Experimental and Theoretical Developments on Accurately Measuring and Modeling Grain Boundary Diffusion in Solids

Zur Erlangung des akademischen Grades eines

Doktors der Ingenieurwissenschaften (Dr.-Ing.)

von der KIT-Fakultät für
Maschinenbau
des Karlsruher Instituts für Technologie (KIT)

genehmigte

DISSERTATION

von

M.Sc. Markus Short
geb. in Gießen

Tag der mündlichen Prüfung:	11 April 2024
Hauptreferent:	Prof. Christoph Kirchlechner
Korreferent:	Prof. Eugen Rabkin

Kurzfassung

Diese Dissertation umfasst drei Hauptstudien und Ergebnisse. In der ersten wird eine neue Technik auf das Design des Heizchips von Zhang et al. (2018) angewendet, die das Pulsen von Dünnschichtproben mit Raten von bis zu 25.000 K/s und die Erkennung von mikrostrukturellen Veränderungen ermöglicht, die mit kalorimetrischen Methoden nicht wahrnehmbar wären. Unter der Annahme, dass die Anwendung einer identischen Heizleistung über einen bestimmten Zeitraum unabhängig vom Dünnschichtmaterial zur gleichen Temperatur führen würde, konnte ein Kalibrierungsmaterial (hier Au) mit einer bekannten Temperatur-Widerstands-Beziehung mit der interessierenden Probe ausgetauscht werden, was die Temperaturmessungen vereinfachte und den Probendurchsatz erhöhte. Durch das Pulsen von Ni/Al-Multilayer-Dünnschichten mit linearen 100 K/s-Pulsen traten zwei deutliche Spitzen im Widerstand mit Aktivierungsenergien von 55 ± 4 bzw. 74 ± 7 kJ/mol auf. Die STEM-Analyse identifizierte den zweiten Peak als Folge einer Umwandlung der mehrschichtigen Dünnschicht in eine homogene NiAl-Legierung, abhängig vom anfänglichen stöchiometrischen Verhältnis, während EDS-Linienscans Spitzen in der Ni-Konzentration entlang der Al-Korngrenzen nach dem ersten Peak zeigten. Dies stellt eine zugängliche Technik zur Untersuchung der Korngrenzendiffusionsdynamik und zur schnellen Abstimmung und Kalibrierung neuartiger heterogener Mikrostrukturen dar.

In der zweiten Studie wurde das Fisher-Modell für die Korngrenzendiffusion unter der Annahme der Konzentrationsabhängigkeit überarbeitet. Dadurch wurde der Fisher'schen Randbedingung ein zusätzlicher Term für die zeitliche Konzentrationsänderung entlang der Korngrenze hinzugefügt, dessen Bedeutung unter realistischen Materialparametern mit Hilfe eines Finite-Differenzen-Modells bewertet wurde, um eine 2D-Diffusionskarte zu simulieren, bei der die Korngrenze senkrecht zur Diffusionsquelle verläuft. Bei Einbeziehung dieses dritten Terms wurde festgestellt, dass die resultierenden Isokonzentrationskurven um einen Betrag abweichen, der mit TEM-Methoden leicht messbar ist (etwa 5-10 nm), wenn der Diffusionskoeffizient an der Korngrenze um etwa 0,5-0,6 Größenordnungen in Bezug auf die Konzentration der diffundierende Spezies variiert. Der ermittelte Wert lag deutlich innerhalb der in der Literatur häufig gefundenen Bereiche, die um 2 oder mehr Größenordnungen variierten. Da die Wärmetransport mathematisch sehr ähnlich zur Diffusion in Festkörpern verhält, da sie linear proportional zu deren Gradienten steht, bietet dies die Möglichkeit, thermodynamische und metallurgische Effekte in heterogenen Mikrostrukturen genauer zu modellieren, indem Wärmepulse angewendet werden.

Die Fähigkeit, kleine Flüssigkeitsmengen von etwa 50 µL schnell zwischen 65 und 95 °C thermisch zu Zyklieren, um eine ultraschnelle PCR durchzuführen, wurde mit einer modifizierten Version der Dünnschicht-Heizspirale aus dem ersten Abschnitt getestet. Durch die Erweiterung der Abmessungen der Spirale, deren Schutz mit einer Schicht aus SiN, SiC oder Teflon und die Anwendung einer 3D-gedruckten hohlen zylindrischen Kunststoffkappe konnte eine sehr dünne Flüssigkeitssäule injiziert und gegen das Dünnschichtelement gedrückt werden. Obwohl beeindruckende thermodynamische Leistungen erzielt wurden, insbesondere eine Abkühlrate von etwa 30 K/s, konnten die Schutzschichten nicht verhindern, dass es zur Delaminierung kam, und eine vollständig erfolgreiche Polymerase Chain Reaction (PCR) wurde nicht erreicht. Daher werden einige Strategien vorgeschlagen, um dieses Problem in der Zukunft anzugehen.

Abstract

Three main studies and findings comprise this dissertation. In the first, a new technique is applied to the heating chip design from Zhang et al. (2018) that allowed the pulsing of thin film samples at rates up to 25,000 K/s and the detection of microstructural changes that would be imperceptible to calorimetric methods. With the assumption that applying an identical heating power over time would result in the same temperature response, regardless of thin film material, a calibration material such as Au with a known temperature vs. resistance relationship could be swapped out with the sample of interest, simplifying temperature measurements and increasing sample throughput. By pulsing Ni/Al multilayer thin films with linear 100 K/s pulses, two distinct spikes in resistivity occurred with activation energies of 55 ± 4 and 74 ± 7 kJ/mol, respectively. STEM analysis easily identified the second peak as resulting from a solid state transformation of the multilayer thin film into a homogeneous NiAl alloy, depending on the initial stoichiometric ratio. Additionally, EDS linescans revealed spikes in Ni concentration along Al grain boundaries after the first peak. This technique offers an accessible approach to studying grain boundary diffusion dynamics and enables rapid tuning and calibration of novel heterogeneous microstructures.

The second study reworked Fisher's model for grain boundary diffusion with the assumption of concentration dependence. This added an extra term to Fisher's boundary condition for the change in concentration along the grain boundary over time which was evaluated for its significance under realistic material parameters using a finite difference model to simulate a 2D diffusion map with the grain boundary perpendicular to the diffusant source. Upon the inclusion of this third term, the resulting isoconcentration curves were found to deviate by an amount easily measurable using TEM methods (about 5-10 nm) when the grain boundary diffusion coefficient varied by about 0.5-0.6 orders of magnitude with respect to diffusant concentration. This was well within ranges often found in the literature that varied by 2 or more orders of magnitude. Since heat diffusion is mathematically very similar to diffusion within solids, being linearly proportional to their gradients, this offers the ability to more precisely model thermodynamic as well as metallurgical effects in heterogeneous microstructures under the application of thermal pulses.

The ability to rapidly thermally cycle small liquid volumes of around 50 µL between 65 and 95 °C for the purpose of ultrafast PCR was tested using a modified version of the thin film heating spiral of the first section. By expanding the spiral's dimensions, protecting it with a layer of SiN, SiC, or Teflon, and applying a 3D printed hollow cylindrical plastic cap, a very thin cylinder of liquid could be injected and pressed up against the thin film element. While impressive thermodynamic performance was achieved, specifically its cooling rate reaching about 30 K/s, the protective layers failed to prevent delamination and a fully successful PCR was not achieved. Some strategies are therefore proposed to address this in the future.

Preface

Before I begin with this dissertation I would like to take a moment to acknowledge those that surrounded me here at KIT, lest the reader infer that the findings contained therein were purely a result of my own efforts.

None of this work would have been possible without my many unique colleagues, although in some cases, possibly a bit more could have been achieved. As of writing this, there remains in my office a closet full of empty bottles from around the world that were shared with my former office mate, Tobias, used to stimulate many evening discussions of various topics such as culture, politics, good books, and our work if we found the time. This of course all supervised by our group leader, Karsten, who was too busy finding sources of funding to partake.

If there was ever a need for our workshop, Herr Ernst wouldn't give up on solving your problem even if you did. He was filled with interesting stories from his childhood in Romania, and was the type of person to stop a meeting in order to rescue a spider. Some may have questioned his priorities but they were fools to do so. His retirement may have come too soon for us, but it was well earned. The institute attempted to replace him with Herr Böck, but instead found someone entirely new. Equally capable and charming in a classically German way, he was never willing to bend the rules for anyone. Unless you asked nicely. Or it was Easter.

When institutes are well run, it's easy to forget the effort it takes to keep it that way. Their names may not appear in any of our papers, but without our secretarial staff, Jana and Gabi, there wouldn't be any work to publish in the first place.

Through simple experience, one learns the value of our senior staff, section, and group leaders. Besides my own group leader, Karsten, the ones who aided my work the most included Subin, Marc, Rainer, Dominik, and Heinz. Besides their own students, their intelligence, curiosity, and drive were freely available to any of us, and I am continually thankful to them.

Halfway through my time here, Christoph, the new head of the institute, joined our collective team. With a wife, three children, and seemingly vastly more time than the rest of us, there is an ongoing debate on whether he sleeps. Quick to the punch, generous with his efforts, and a continual test for my ability to understand spoken German, IAM-MMI was undoubtedly made better by his presence.

In no particular order I wish to thank Oleg, Verena, Friedemann, Chani, Alex, Silva, Jin, Johanna, Felix, Julian, Korbi, Niko, Thimo, Manfred, Juan, Qian, Vishi, Eloho, Valentin, Christina, Diana, Ujjval, Sabrina, Camila, and Angelica for their friendship, and for always patiently waiting for me to finish my lunch.

Finally I want to thank my dear wife, Adri, for supporting me, motivating me, and keeping me well fed throughout my long days and nights researching for and writing this dissertation. Siempre séras mi amor.

Doctoral students, like all people in the scientific profession, are taught to be cynical people. Personally, my preferred description of how the laws of nature are determined is that of Richard Feynman, who described it in three steps: First, you guess. That guess may be grounded in experience and mathematical derivations, but even mathematics is a more refined extrapolation of previously observed patterns. Second, you derive a list of observable consequences should your guess be true. And finally, you observe how nature responds. If it doesn't match your expected consequences, your guess is wrong. An unflinching adherence to evidence is therefore a virtue in this context, even if it often takes a toll on the ego for our guessing abilities.

It naturally follows then, to take an equally cynical approach to the purpose of writing a dissertation. After all, their most interesting contents have been distilled and published, and any extra desired information is accessible with "ctrl-f". The writing style has to be taken from a sterile, third-person perspective, and if there's any plot, the abstract steals the mystery immediately after the title page. The order of my research is presented here as a logical progression of thought, but that was only achieved after much discussion on how to do so. If I have handed you this stack of papers to read, it's likely I humbly and awkwardly expressed my profuse gratitude for doing so! Writing itself is inherently a test of the readers patience, who has to listen to the writer go on and on about himself without the ability to interject. But, it is a pleasure of mine to deprive you of that ability to share my work of the last 4 years with you. In an attempt to reward your time, much thought was put into the conclusions of each chapter on how the information presented could be used, branching into fields such as physics, chemistry, materials science, and biology. If any of these may be put to use, or to stimulate an engaging daydream, I would be content with my efforts.

Contents

Kurzfassung . . . . **i**

Abstract . . . . **iii**

Preface . . . . **v**

1 Introduction and motivation **1**
- 1.1 Introduction 1
- 1.2 Motivation 5

2 Thin Film Heating Coil **9**
- 2.1 Method 16
  - 2.1.1 Measurement Circuit 23
- 2.2 Results 25
  - 2.2.1 EDX Linescans 29
  - 2.2.2 Activation Energy 32
  - 2.2.3 Mechanical Characteristics 33
- 2.3 Discussion 35
- 2.4 Conclusion 39

3 Concentration Dependent Grain Boundary Diffusion **43**
- 3.1 Theory 45
  - 3.1.1 Analytical Solution 49
  - 3.1.2 Layer Averaged Diffusion 51
- 3.2 Finite Difference Simulation 53
- 3.3 Results and Analysis 54
- 3.4 Conclusion 62

4 PCR Cycler **67**
4.1 PCR Background 67
4.1.1 PCR Product Analysis 69
4.2 Current Rapid PCR Strategies 71
4.3 Design 76
4.4 Results 79
4.5 Conclusions 83

5 Summary **85**
5.1 Summary and Outlook 85

A Appendix **89**
A.1 Matlab Finite Difference Simulation 89

List of Figures **99**

List of Tables **107**

List of Publications **109**
Journal articles 109

Bibliography **111**

1 Introduction and motivation

1.1 Introduction

This dissertation aims to present an experimental and a theoretical tool to facilitate better research into interdiffusion effects within solids, specifically in the context of fast diffusion pathways such as grain boundaries which will be divided into two chapters. The experimental work will be focused around thin films, which gave the necessary flexibility in heating and cooling rates, while a numerical simulation was used to evaluate the significance of the theoretical development. In addition, as inspired by the COVID-19 pandemic that affected the globe while this work was underway, a final chapter covers a potential application to human diagnostics that may aid in mitigating the effects of future pandemics and improve patient outcomes in a general care situation by quickly identifying infectious agents from a wide pathogenic library.

While artificially created thin films may stretch back to the ancient Egyptians 5000 years ago (Greene 2014), research into their resistance characteristics began with the work of Stone (1898), notably the second woman awarded a Ph.D. in physics in the United States. Her thesis was primarily concerned with the question of why the resistivity of silver thin films differed from that of the bulk material, and identified its microstructure as the cause due to the change in resistance over time that accelerated with the application of heat described as "a gradual settling down of the silver molecules into a more and more compact mass". In addition, its resistivity suddenly spiked when the film thickness was reduced below about $60\,\mathrm{nm}$, which was noted by other researchers such as Longden (1900). It was only later that Wait (1922) and Steinberg (1923) theorized that the granular structure of metals was the cause of this effect.

Subjecting thin films to rapid thermal pulses was inspired by processing requirements of polysilicon micromechanical structures. Some examples of their applications include accelerometers, pressure sensors, and actuators. Ion-implantation of dopants and micromachining was found to introduce undesirable residual stresses into the polysilicon that could be alleviated by high temperature annealing (Howe 1986), but this was not attractive in every case since this would degrade the electrical characteristics of the microelectronic chip. Putty et al. (1989) found that by applying a rapid thermal pulse in a process dubbed Rapid Thermal Annealing (RTA), residual stresses in polysilicon could be dramatically reduced while preserving its nMOS circuitry. Huber et al. (1989) and Ristic et al. (1992) further substantiated these claims, and inspired Allen et al. (1994) to develop a testing device using an Electrical Thermal Annealing (ETA) technique where high current was passed through a conducting substrate that heated an overlying thin film at rates reaching 10^6 K/s. This was then reworked by Lai et al. (1995) into a device eventually called a nanocalorimeter, where the sample of interest was deposited onto a Ni thin film that served as a heater and thermometer which was suspended on an ultrathin SiN membrane. Any deviations in the expected heating rate were identified as changes in heat capacity of the sample, which indicated irreversible phase changes.

Zhang et al. (2018) proposed a different approach where the sample material itself was used as the heating strip. Their device consisted of a thin film on a solid substrate, structured into a circular coil using photolithography. The key development was the assumption that the heat capacity of the coil was insignificant in relation to the overall heat capacity of the system, allowing for a direct association between input power and temperature once the device reached thermodynamic equilibrium. After calibration with a thin film material such as Au with a known and stable resistance vs. temperature relationship, the calibration material could be swapped out with any conducting sample of interest and the input power would result in the same temperature, alleviating the challenge of precise temperature measurements during thermal pulsing. However, the time needed for the temperature to stabilize was on the order of minutes, preventing its application to tests involving rapid thermal pulses.

A solution for this is presented in chapter 2, where instead of calibrating a set of input powers and temperatures, a power pulse was regulated to achieve a desired temperature pulse, with the assumption that applying the same power pulse to any sample of interest would result in the same temperature pulse. Using a modular PXIe system from NI (Austin, USA), both pulsing and measurement could be integrated into one system reaching a measurement frequency of 10,000 Hz or $100\,\mu\mathrm{s}$ resolution, with a dynamic feedback loop to ensure precise control over input power into the heating coil. After pulsing the samples with the desired power and associated temperature pulse, the resulting resistance data could be processed to reveal any rapid changes likely corresponding to microstructural changes and identify the time and temperature of their onset. Rectangular cross sections about $30\,\mu\mathrm{m}$ x $10\,\mu\mathrm{m}$ x $100\,\mathrm{nm}$ in size could then be lifted out from the thin film coil using a Focused Ion Beam (FIB) and analyzed using Scanning Transmission Electron Microscopy (STEM) and Energy Dispersive X-Ray Spectroscopy (EDX) to map out the resulting microstructure and elemental distribution with up to nm resolution. Applying this technique to Ni/Al multilayer thin films allowed the detection of morphological changes involving phase changes along grain boundaries that would be imperceptible with nanocalorimetry.

Since the kinetics of grain boundary diffusion were so critical to understanding the evolution in microstructure observed via the thin film heater, much thought was given on the mathematics of modeling such a scenario. The model presented by Fisher (1951) still forms the backbone of most attempts to measure grain boundary diffusion coefficients (Mishin et al. 1997). Much researchers have worked on modifying and extending its application such as Whipple (1954) who used a Fourier-Laplace transform to derive a precise analytical solution to Fisher's model and Suzuoka (1961) who generalized the solution to a non-infinite source. However, it was noticed that the original model and all its solutions assumed the grain boundary diffusion coefficient was constant with respect to concentration, which was often not the case (Achter et al. 1959, Austin and Richard 1961, 1962).

Indeed, it was commonly observed to vary by multiple orders of magnitude as the concentration of the diffusant species varied. Rabkin (1996) proposed an analytical solution that was generalized from the case of discontinuous changes in the grain boundary diffusion coefficient along the grain boundary due to phase changes. However, some assumptions were made such as a quasi-stationary solute distribution within the grain boundary and a constant segregation factor.

For this reason, chapter 3 presents a new boundary condition for concentration change over time along the grain boundary, derived using the same method originally used by Fisher, sans the assumption of concentration independence. This introduced a third term into the original boundary condition which was evaluated for significance using a finite difference simulation with material parameters similar to those found in the literature. The resulting data was reprocessed to match the data from radioisotope tracer diffusion methods widely used in the literature to measure grain boundary diffusion (Mishin et al. 1997). However, the most significant effect was found in the shifting of isoconcentration lines in the resulting 2D diffusant concentration field that was found to be well within the resolution of Transmission Electron Microscopy (TEM) techniques.

The moment current was cut off to the thin film heater, its temperature fell by over 1000 K/s which allowed the quenching of the microstructure at various points along its evolution. It was quickly realized that this remarkable cooling rate gave the potential to rapidly cycle materials between temperature points. Beyond applications to stress testing, a particularly motivating application was to speed up Polymerase Chain Reaction (PCR) cycling times. This technique, first developed by Mullis et al. (1986), creates copies of a DNA fragment with each cycle then uses those copies to create more, resulting in an exponential increase in identical DNA fragments with each cycle. This has formed the backbone of genetic research and the biotech industry and unlocked access to the genetic code for study and manipulation. In the context of diagnostics, DNA primers consisting of a sequence of base pairs unique to a certain pathogen can be introduced to a potentially infected sample. If a matching set of base pairs is found in the sample, this is amplified and confirms the presence of the pathogen. 30-40 cycles are often needed for sufficient amplification and detection.

To adapt the thin film heater for this purpose, its geometry was first expanded to maximize the surface area to volume ratio and enhance heat transfer. A protective layer of SiN, SiC, or Teflon was deposited over the top to protect the heating coil from the overlying liquid. A 3D printed, hollow cylindrical cap was attached over the top and the liquid was injected inside through small holes on the top. The high aspect ratio of the liquid cylinder allowed it to maintain a high thermal gradient into the substrate below, giving it impressive cooling performance even without the addition of any active component. Unfortunately, as each protective layer failed to prevent delamination of the heating coil, no successful PCR could be achieved. Some solutions are therefore proposed to address this issue.

1.2 Motivation

Grain boundary diffusion coefficients are inherently difficult to measure. The fact that diffusion through a grain boundary is attenuated through leakage into the surrounding grains was addressed by Fisher (1951), but precise measurements remain elusive due to its complicated nature. Grain boundaries come in many forms, with many different misorientations, resulting interface energies, segregation and precipitation effects, and migration of their own through the polycrystal. An atomistic understanding of diffusion in solids is quite developed in the literature and is well summarized in chapter 6 of *Diffusion in Solids: Fundamentals, Methods, Materials, Diffusion-Controlled Processes* by Mehrer (2007), which explains that atoms jumping into neighboring vacancies within crystal lattices is the primary mechanism. This justifies quite well why diffusion within grains proceeds much more slowly than in grain boundaries, which are naturally defect rich regions. However, since a polycrystalline material is so complex, it is nigh impossible to derive a model such as an ideal gas law accurately encompassing a large amalgamation of these statistical events.

But this complexity is exactly what makes these polycrystalline materials so interesting to materials scientists. When its structure is changed via recovery and recrystallization, plastic deformation, solute migration, segregation, precipitation, and by exposure to magnetic fields, its hardness, shear strength, tensile strength, elasticity, ductility, fracture toughness, ferroelectric, piezoelectric, pyroelectric, ferromagnetic, ferrimagnetic, thermal, and electrical characteristics can be altered. These can either be beneficial such as the classic finding from Hall (1951) that grain boundaries impede dislocation movement and therefore work hardening can strengthen a material, or detrimental. The reason the integrated circuits in your computer have to be kept below a certain operating temperature is because above this point, diffusion effects will permanently alter their precisely designed microstructure. Some specific examples of deterioration due to grain boundary migration effects recently published in the literature include degradation of solar cells (Luka et al. 2016, Sung Yun et al. 2018), fuel cell cathodes (Chen et al. 2019), battery cathodes (S.-A. et al. 2020, Zhang et al. 2022a), superconductors (Qiao et al. 2021), and corrosion induced embrittlement of steels (Yavas et al. 2018, 2020). These are the technologies necessary to drive the electrification of our energy sources to reduce emissions and address the climate crisis.

It is difficult to better motivate using words the need for fast, cheap, sensitive, and accurate tools for the detection of human pathogens than our collective experience over the past few years. Contrary to what many of us may believe, PCR tests for COVID-19 were developed by Jan. 10, 2020 (Zambon et al. 2020), a full four months sooner than antigen tests (Hahn and Shuren 2020). This is because the development of chemical reagents that will result in an easily identifiable change, such as a change in color, upon reaction with a specific antigen (and not any of the other countless chemical species contained in our bodies) is a complicated task, whereas a new PCR test is largely plug-and-play where all that is needed is a unique sequence of base pairs from the pathogen's genome. The reason most of us had access to the antigen test first is because PCR testing is time consuming and expensive, partly because it is so time consuming. While it is impossible with today's technology to eliminate the need for a lab with trained operators, increasing throughput will drive down cost per test. It may take 30 minutes to an hour to complete the necessary cycles, and various methods have been proposed to speed this up including photonics (Son et al. 2015, You et al. 2020) and Peltier elements enhanced by liquid thermal interfaces (Maltezos et al. 2010). The fastest methods proposed so far have used microfluidics (Kim et al. 2019, Kang et al. 2021) where the sample is squeezed through ultra-small channels held at the different temperature set points, achieving results within 4-5 minutes. However, these are expensive devices involving complex fabrication methods that can only be used once due to the impossibility of cleaning out their fine channels. If the sample were instead pressed against a flat surface to recreate such a high surface area to volume ratio and thereby high rate of heat transfer, it may be possible to sterilize this surface and reuse the device.

Such a development, if successful, could radically transform not only population testing but also an everyday visit to a clinic. Infections may be bacterial, viral, or fungal, which require different medicines and courses of treatment. A doctor must rely on an overlapping set of symptoms, and the often unreliable perceptions of the patient, in order to prescribe an appropriate response. Often times, antibiotics are given forthright with the assumption that a bacterial infection is most likely the case, and an alternative is given only in the event that this fails, delaying successful treatment and resulting in an over-prescription of antibiotics. Such guesswork would be eliminated by a cheap and effective PCR device that could test an array of different pathogens with results within the time it takes to discuss your symptoms to your doctor.

2 Thin Film Heating Coil

Chapter 2 is based on:
Short, M., Müller, J., Lee, S., Fornasier, H., Köhler, U., Ott, V., Stüber, M., Gerdes, B., Rupp, T., Kirchlechner, C., & Woll, K. (2023). *Heterogeneous Microstructures Tuned in a High Throughput Architecture*. Materials and Design, 229. 4
https://doi.org/10.1016/J.MATDES.2023.11183
* This work was done under the supervision and direction of K. Woll. The PID regulator was tuned by J. Müller. Photolithography was performed by H. Fornasier with consultation from U. Köhler. The thin films were deposited by V. Ott and T. Rupp with consultation from M. Stüber and B. Gerdes, respectively. S. Lee provided the electron microscopy data. J. Li provided nanoindenation data as well as the respective optical and Scanning Electron Microscopy (SEM) images of indented sites. Additional consultation for the final draft of the cited publication was provided by C. Kirchlechner.

A primary difficulty of investigating diffusion phenomena is achieving a precise control of temperature. Diffusion coefficients (D) can be modeled by the Arrhenius equation as follows,

$$D = D_0 \exp\left(-E/K_B T\right) \tag{2.1}$$

where D_0 is the standard diffusivity, E is the activation energy, K_B is the Boltzmann constant, and T is the temperature. This exponential relationship between

D and T means temperature overswings of even a few degrees can significantly influence results.

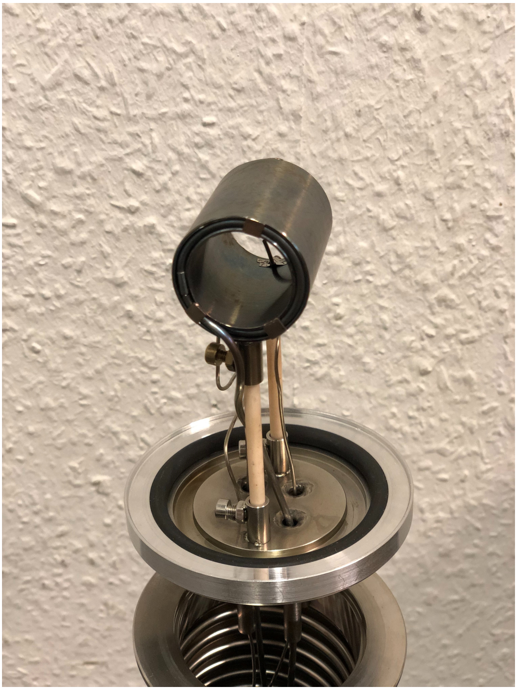

Figure 2.1: An image of the cylindrical oven used to heat bulk samples in a vacuum. The heating element was wrapped between two steel cylinders which were held up with two ceramic rods. Two thermoelectric probes measured the temperature on the inside and outside surface of the cylinder.

Early in our investigations, one strategy to thermally pulse bulk samples used a resistively heated cylindrical coil. An image of the device is shown in figure 2.1. The sample was placed within the cylinder which was then inserted into a high vacuum ($\sim 10^{-6}\,\mathrm{mbar}$) to minimize convective losses and oxidation during heating.

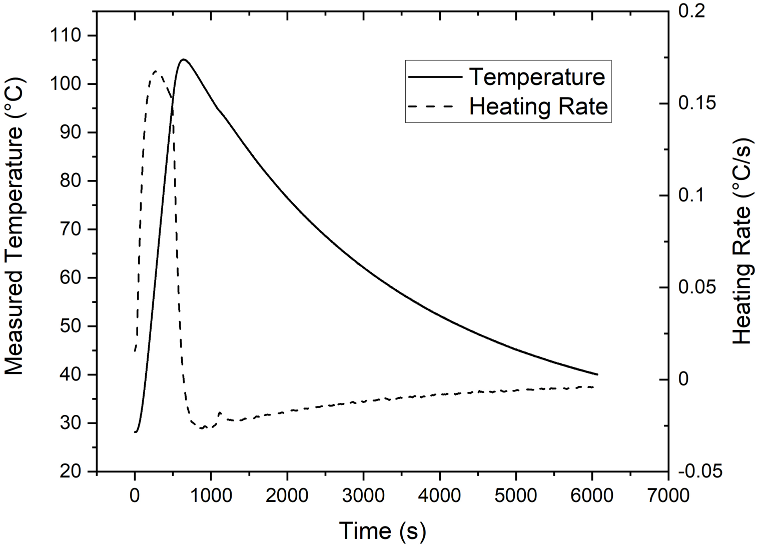

Figure 2.2: Temperature and associated heating rate of a silicon chip pulsed within the cylindrical heater shown in figure 2.1. The temperature was measured with a thermocouple that was bent upwards so as to contact the sample. After 100°C was achieved, the current through the heating element was cut off, and the system was allowed to passively cool.

Figure 2.2 shows the temperature of a small approximately 1 square centimeter silicon chip during a thermal pulse that heated the sample from room temperature then cut off current after 100°C was achieved. The thermocouple on the inside of the cylinder was bent upwards so as to make direct contact with the sample chip. The dashed line shows the heating rate, revealing a maximum and minimum of 0.16 and -0.03 $\mathrm{K\,s^{-1}}$, respectively. This was quite low, and would have severely limited the heating and cooling rates available to us for pulsing a sample. This was of course no surprise, as the thermal contact between the resistively heated coil and the sample was very poor.

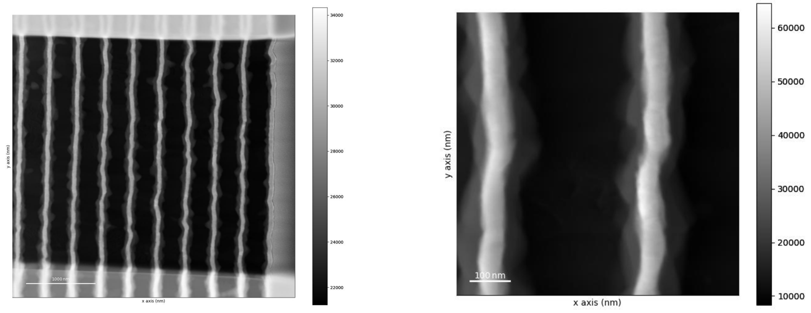
y axis (nm)
1000 nm
x axis (nm)
34000
32000
30000
28000
26000
24000
22000
y axis (nm)
100 nm
x axis (nm)
60000
50000
40000
30000
20000
10000

(a) **(b)**

Figure 2.3: Multilayer Ni/Al sample heated to 250°C for 60 minutes in a TOF.SIMS 5. TEM lamellae were cut using a Zeiss Crossbeam 550 L FIB with the method shown in section 2.2. The STEM images shown here were obtained using a Tecnai F20 from FEI (Hillsboro, USA) with a beam voltage of 200 kV.

Another method that was used was the *in-situ* heating/cooling system in a Time of Flight - Secondary Ion Mass Spectrometer (ToF-SIMS) called a TOF.SIMS 5 from IONTOF (Muenster, Germany). This could achieve a heating rate of around $2\ \mathrm{K\,s^{-1}}$ and a cooling rate of around $1\ \mathrm{K\,s^{-1}}$ using a resistive heating element and a heatsink which was attached to a liquid nitrogen reservoir that could be moved into contact with the sample. STEM images of a multilayer Ni/Al thin film sample heated to 250°C for 60 minutes in such a system are shown in figure 2.3, revealing a significant amount of intermetallic phase formation along the Ni/Al interface.

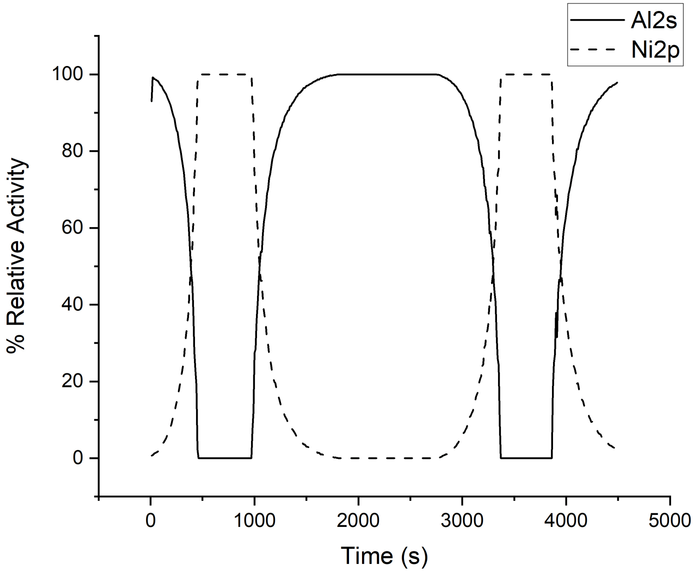

Figure 2.4: X-ray Photoelectron Spectroscopy (XPS) data from sputtering the Ni/Al sample shown in figure 2.3 in a TOF.SIMS 5 using an Ar source with a current of $10\,\mu\text{A}$, accelerated to an energy of $3\,\text{keV}$. The relative concentration of Ni and Al is taken from the relative activity of their 2p and 2s peaks, respectively. Time refers to the sputtering time.

Figure 2.4 shows XPS data from sputtering the sample using an Ar source, showing a periodic change in concentration of Ni and Al as each film is eroded. It is clear from this how Ni is the primary diffuser, as there is a gradual, exponential decrease in Ni concentration moving into the Al layer, but a sharp drop in Al concentration past a certain point in the Ni layer. However, while it is possible to glean some useful information on diffusion coefficients from these data, it is limited in quality by the inability to precisely define sputter depth, the inevitable intermixing due to the sputtering process, and it would be impossible to separate grain from grain boundary diffusion. Finally, if the temperature was increased, the heterogeneous thin film structure would quickly disappear as the Ni and Al completely intermixed into a homogeneous polycrystalline structure, obscuring the intermediate steps to that point. It is difficult to precisely determine quenching points to get an accurate picture of the evolution of the microstructure.

One of the most successful architectures to address this problem (as summarized in the review article by Yi and Lavan (2019)) has been nanocalorimetry consisting of a thin platinum strip on a SiN membrane that the sample is deposited onto. While resistively heating the platinum, temperature can be measured by analyzing its change in resistance. Deviations from the expected temperature response can be interpreted as changes in heat capacity of the sample, indicating phase changes. Due to the small thermal masses involved, very high heating rates of up to 10^6 K/s can be achieved (Yi et al. 2015). This can further be combined with *in situ* electron microscopy (Grapes et al. 2014), time resolved X-ray Diffraction (XRD) (Neuhauser et al. 2020), and mass spectrometry (Yi et al. 2015) to better characterize phase transitions.

One disadvantage of this method is that its indirect heating of the sample necessitates a significant volume of phase change to induce a measurable deviation in heating rate. An even simpler design where the platinum strip is eliminated and a current is passed through the sample itself to heat it would allow a direct measurement of its resistance which would be far more sensitive to any microstructural changes due to phase transformations. However, its resistance versus temperature relationship would inherently be unknown making a temperature measurement difficult. The work of Zhang et al. (2018) presented a solution to this problem in the form of a thin film coil deposited onto a solid substrate such as silicon or glass. A diagram of this is shown in figure 2.5.

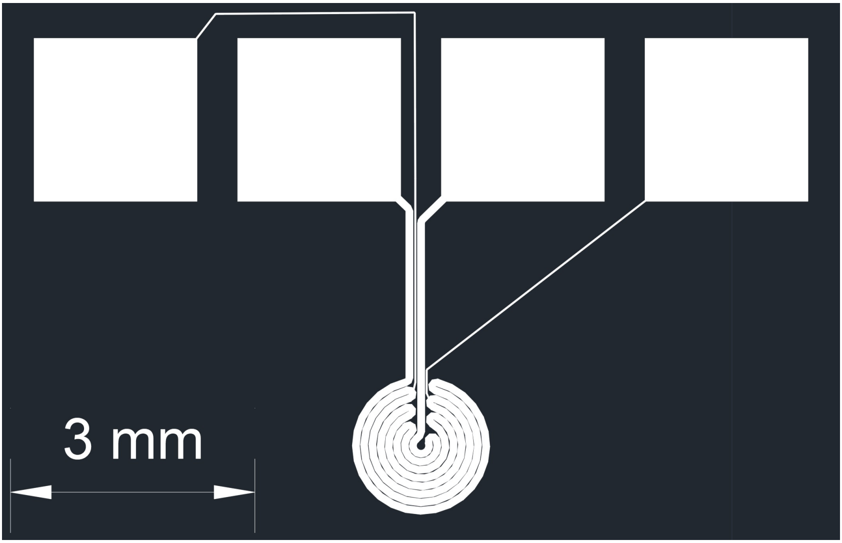

Figure 2.5: Outline of the thin film heater coil used to create a photomask. A current is passed through the two innermost square contact pads which then concentrates through the heating coil below. The two outermost contact pads then allow a measurement of the voltage drop across the third outermost ring in the coil giving its resistance.

The most important assumption underlying the technique of this design is that, as long as the geometry and substrate are held constant, the temperature response of the coil is solely dependent on the input power. This means that if the temperature response for a given power is first measured using a material with a known temperature versus resistance relationship such as gold (where no phase change will occur over the desired temperature range), an identical power will reproduce this temperature result if the gold is replaced with the sample of interest. An array of samples can then be produced and heated with pre-calibrated powers eliminating the need for complex calibration procedures necessitated by nanocalorimetry and allowing a high throughput architecture.

However, the technique presented by Zhang et al. required waiting up to a few minutes until the temperature stabilized, making measurements of fast phase transformations under high heating rates impossible. To address this, a new technique is proposed here involving a Proportional Integral Derivative (PID) regulated power pulse. With the slight modification to the original assumption that an identical power input over time will result in the same temperature response over time, we unlock similar timescales and heating rates as nanocalorimetry.

PID regulation is a widely used feedback loop algorithm that attempts to minimize the difference between a desired set point and process variable (in our case temperature) by applying an appropriate and responsive level to a driving variable (current). In our case, the proportional term modulates current applied (with a minimum of 0 A) by a multiple of the difference between the measured temperature and the desired temperature. This will eventually come to an equilibrium temperature just below the set point due to a constant heat loss. To address this, an integral term increases current by a multiple of the integral difference between the constant set point and temperature over time. A derivative term then decreases current by a multiple of the rate of temperature increase, in order to minimize overswing. These three coefficients must be tuned to provide the most stable response that minimizes overswing but maximizes the speed at which the desired temperature is achieved.

To demonstrate this technique, a linear 100 K/s temperature ramp was PID regulated on a gold calibration chip. The power pulse necessary to achieve this was then applied to multilayer Ni/Al thin films which resulted in noticeable spikes in resistance changes indicating likely morphological and phase changes. The samples were then quenched at various points of interest along this resistance curve and analyzed using electron microscopy.

2.1 Method

A photolithographic process was used to achieve the desired patterning of the thin films on borosilicate glass wafers. The general process is graphically depicted in figure 2.7. To promote wetting and photoresist adhesion by creating a hydrophobic surface, the wafers were first immersed in a hexamethyldisilizane

(HMDS) atmosphere for 30 minutes. The photoresist Ma-N 1440 (Micro Resist Technology GmbH, Germany) was spin coated onto the wafer at 3000 rpm for 30 seconds then baked at 100°C for 180 seconds. The wafers were then irradiated with 365 nm light with a total illumination of 550 $\mathrm{mJ/cm^2}$ through a photomask containing 61 of the patterns shown in figure 2.5 arranged so as to fit on a 4 inch wafer as shown in figure 2.6. Since a negative photoresist was used, a 120 second wash in the developer MaD 533/s (Micro Resist Technology GmbH, Germany) removed any photoresist that was not illuminated.

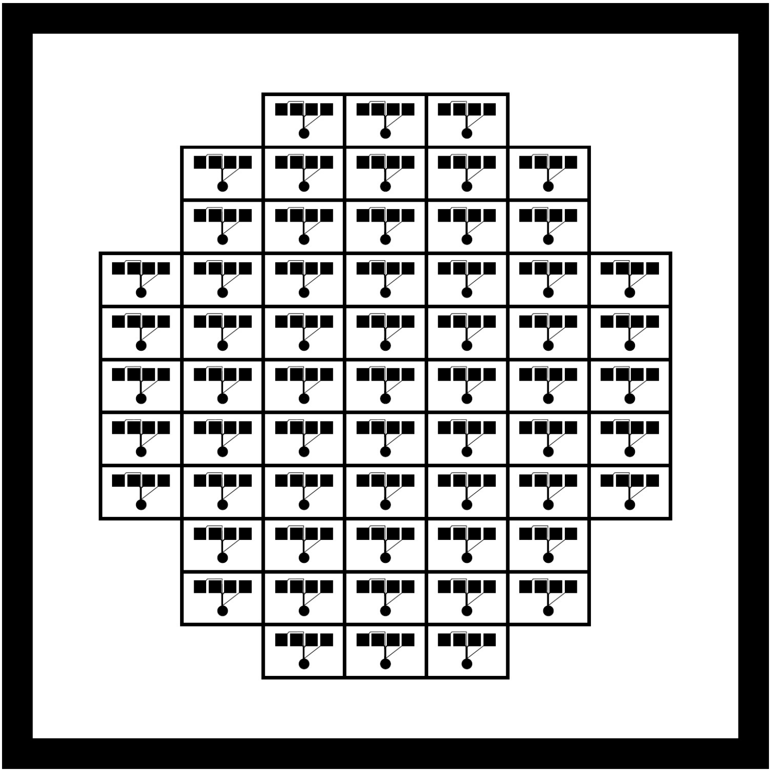

Figure 2.6: An array of the heater coil design shown in figure 2.5 arranged so as to fit on a 4 inch wafer. This was the pattern used for the photomask for the photolithographic process described in figure 2.7.

Sample	Adhesion Layer	Al Thickness	Ni Thickness	# Bilayers
1	15 nm Ti	100 nm	133 nm	3
2	15 nm Ti	200 nm	133 nm	3
3	15 nm Ti	300 nm	133 nm	3

Table 2.1: List of Ni/Al thin film samples indicating their varying Al film thicknesses.

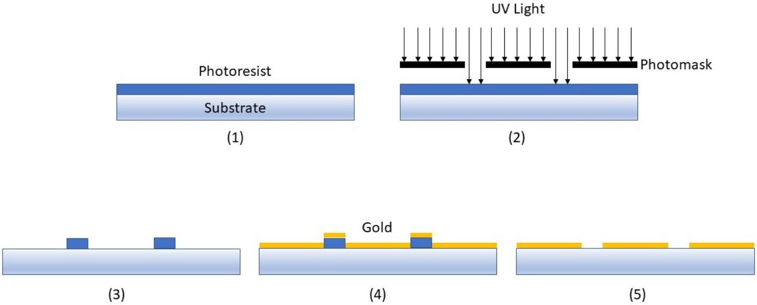

Figure 2.7: Graphical representation of a negative photolithographic process. The steps are as follows: (1) A photoresist is spin coated onto the substrate. (2) The photoresist is illuminated with UV light through a photomask with the desired design. (3) A developer washes away any photoresist not illuminated with UV light. (4) A thin film is deposited (in this case gold). (5) An acetone wash removes the remaining photoresist along with any thin film deposited on top of it, leaving the final patterned thin film.

One wafer was deposited with gold to be used for calibration, while 3 wafers were sputtered with 3 bilayers of Ni and Al with varying Al thicknesses as listed in table 2.1. For the gold calibration samples, electron beam physical vapor deposition with a Univex 450 (Leybold GmbH, Germany) was used to deposit a 10 nm Cr adhesion layer followed by 200 nm of Au. Gold purity was rated at 99.99% and was deposited at a rate of 7-9 Å at a pressure of 1×10^{-4} Pa.

Samples 1 and 3 were magnetron sputtered using a Star 100 Pentaco chamber (FHR Anlagenbau GmbH, Germany). 35 sccm of Ar was released into the chamber giving a pressure of 0.5 Pa. A Ti adhesion layer was sputtered at 200 W giving a deposition rate of 3.5 nm/min that was applied for 4 minutes 17 seconds targeting a thickness of 15 nm. 3 bilayers of Al and Ni were then deposited at a power of 300 and 500 W giving a deposition rate of 6.2 and 11.4 nm/min, respectively. Each Al layer was sputtered for 8 minutes 46 seconds for sample 1 and 26 minutes 19 seconds for sample 3 targeting total layer thicknesses of 100 and 300 nm, respectively. For both samples, Ni was sputtered for 6.2 nm/min for 21 minutes 27 seconds for a targeted layer thickness of 133 nm.

The thin films for sample 2 were magnetron sputtered using a Leybold Z 550 coater (Leybold GmbH, Germany). As before, argon was released into the chamber until a chamber pressure of 0.4 Pa was achieved. Ti was deposited at 18.6 nm/min for 48.4 seconds targeting a thickness of 15 nm. 3 bilayers of Al and Ni were then sputtered at 24 nm/min and 41.4 nm/min for 8 minutes 20 seconds and 3 minutes 13 seconds for targeted thicknesses of 200 and 133 nm, respectively. A TEM image of the result of this process for samples of type 2 is shown in figure 2.8.

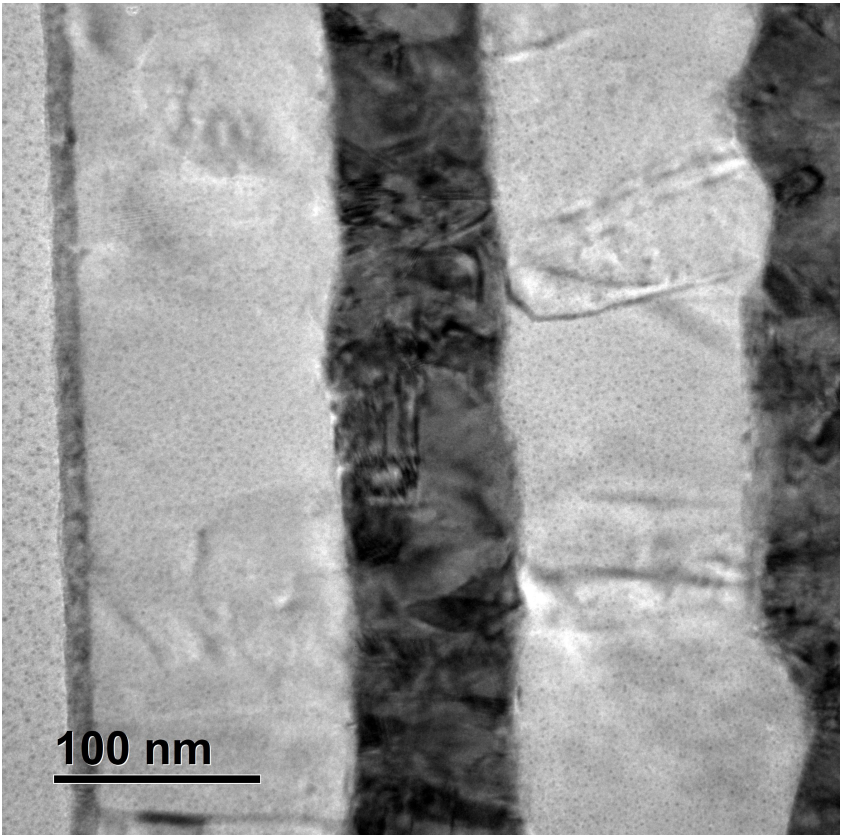

Figure 2.8: A TEM image of an as deposited sample showing the results of the sputtering process for a sample of type 2. On the left is the glass substrate which is separated from the first Al layer by a thin layer of Ti, used to promote adhesion. The Ni layers are the darkest layers. This cross section was extracted using the method described in section 2.2 and imaged using a Tecnai F20.

The wafers were then at step 4 of the lithographic process shown in figure 2.7. In order to remove the unwanted thin film, the remaining photoresist beneath it was dissolved and washed away in an acetone bath stirring overnight at 1 Hz. The wafers were then diced into their 61 constituent chips looking much like figure

2.5. An optical microscope was used to check for any defects such as short circuit bridges.

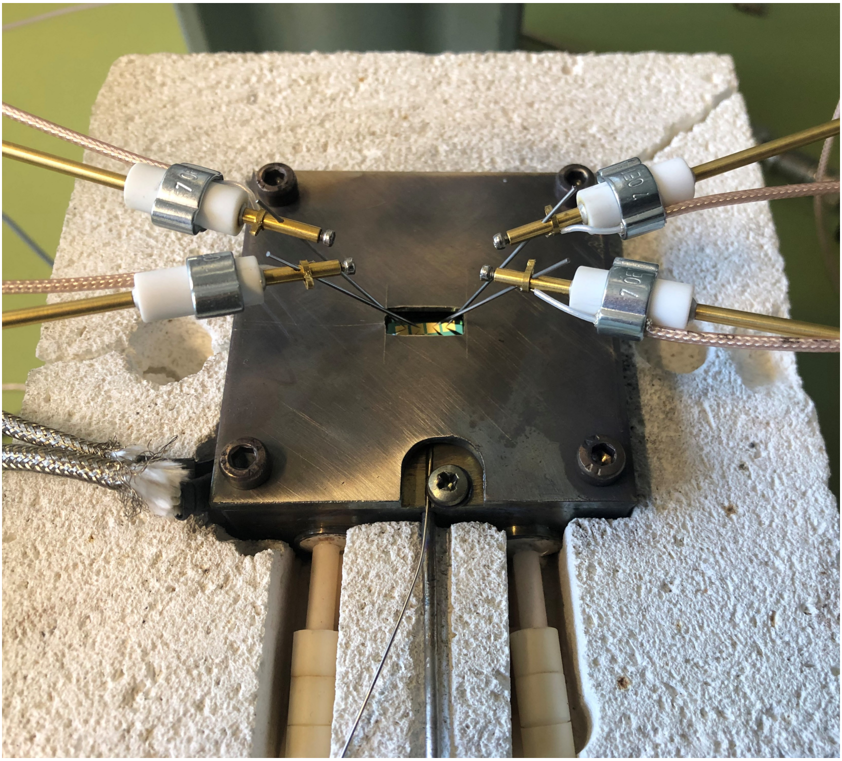

Figure 2.9: An image of the setup used to characterize the temperature versus resistance relationship of the gold calibration chips. The copper heating block was incrementally stepped up in temperature, measured with a thermocouple underneath the chip. A 4 contact point measurement with tungsten needles using a 20 mA current was used to measure the resistance across the third outermost ring in the heating coil shown in figure 2.5.

Before a thermal pulse could be tuned and calibrated on the gold chips, their temperature versus resistance relationship had to be determined. To do this, the setup shown in figure 2.9 was used. The chips were placed on a copper heating block with a thermocouple built into to the block directly underneath the chips. A copper lid was placed over the top to minimize temperature gradients and ensure the thermocouple reading was as close to the temperature of the heating spiral as possible. A rectangular hole was cut into this lid to give 4 tungsten needles access to the electrical contact pads on the chips.

While current was passed through the coil via the two innermost contact pads, the two outermost pads allowed a measurement of the voltage drop across the third outermost ring of the heating coil. This gave an accurate 4 contact point measurement of the resistance of this ring, which will be the resistance analyzed and discussed in the remainder of this chapter. To ensure the current used during calibration was low enough to avoid extraneous heating but high enough to ensure an accurate measurement, it was incrementally increased until a change in resistance was measured at around 30 mA. 20 mA was then chosen as a safe measurement current.

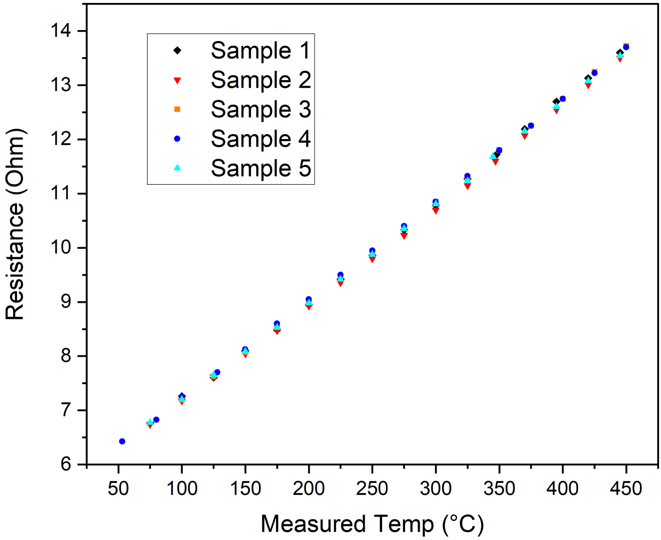

Figure 2.10: Resistance versus temperature relationship for 5 different gold calibration samples using a 4 contact measurement at 20 mA with the setup shown in figure 2.9.

The resistance versus temperature data of 5 different gold calibration samples is shown in figure 2.10. While the relationship is mostly linear, a second order polynomial was used to fit the data to ensure the best fit.

2.1.1 Measurement Circuit

To pulse the chips and readout the resulting voltage data an integrated system from NI was used. A PXIe-1071 chassis contained the PXIe-4139 Source Measure Unit (Source Measure Unit (SMU)) and PXIe-4464 Sound and Vibration Module. Figure 2.11 shows how these were attached to the contact pads on the chip shown in figure 2.5. The SMU provided the current source that was fed through a 1 Ω shunt resistor then the current contact pads. The analog input A_3 of the PXIe-4464 measured the voltage across the shunt resistor, giving an accurate current measurement. A_1 and A_2 were both attached to the voltage contact pads. A_1 was set to a dynamic readout mode, allowing the PID algorithm to be regularly updated with temperature data while A_2 was set to burst measurement mode at 10,000 Hz, giving a greater temporal resolution.

[!ht]

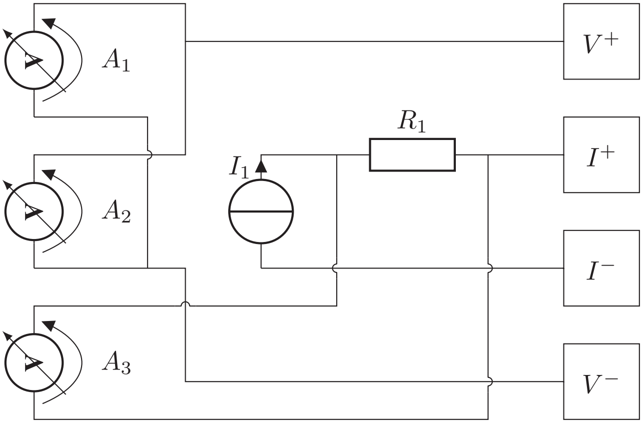

Figure 2.11: A circuit diagram describing the measurement setup. A_1 through A_3 refer to the analog voltmeters on the PXIe-4464 while current, I_1, was sourced from the SMU. On the right in the diagram are the four contact pads of the chip shown in figure 2.5 with the labels V^+, V^-, I^+, and I^- indicating the voltage and current pads, respectively. Current from the source I_1 flowed through the 1 Ω shunt resistor R_1 followed by the current pads leading to the heating coil. The voltage across R_1 was measured by A_3 for an accurate current measurement. A_1 and A_2 both measured the voltage across the voltage contact pads.

A power pulse PID tuned to match a desired temperature pulse of 100 K/s is shown in figure 2.12. To verify a sufficient degree of similarity between the chips, another gold calibration chip was pulsed using the same power over time that was PID tuned to achieve the desired temperature pulse. The resulting temperature data is plotted over the previous in figure 2.12, showing very good agreement.

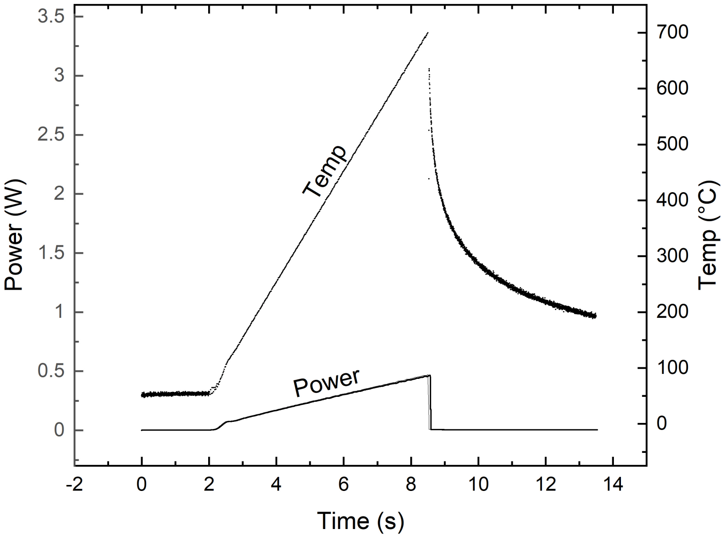

Figure 2.12: Data showing two power pulses. The first was applied to a gold calibration sample that was PID regulated to match a 100 K/s linear ramp to 700°C. The same power pulse was then applied to another calibration sample and the resulting temperature data were plotted over the former, showing very good agreement. Reprinted from Short et al. (2023).

2.2 Results

The same power over time shown in figure 2.12 was then applied to two different Ni/Al samples of type two. The resulting resistance data, plotted over temperature, is shown in the top image of figure 2.13. The data was smoothed using a Savitsky-Golay algorithm, the first derivative of which is shown in the image below. 2 distinct, reproducible peaks in resistance change are clearly visible, with the smaller first peak appearing at around 285°C followed by a significantly larger one at around 360°C.

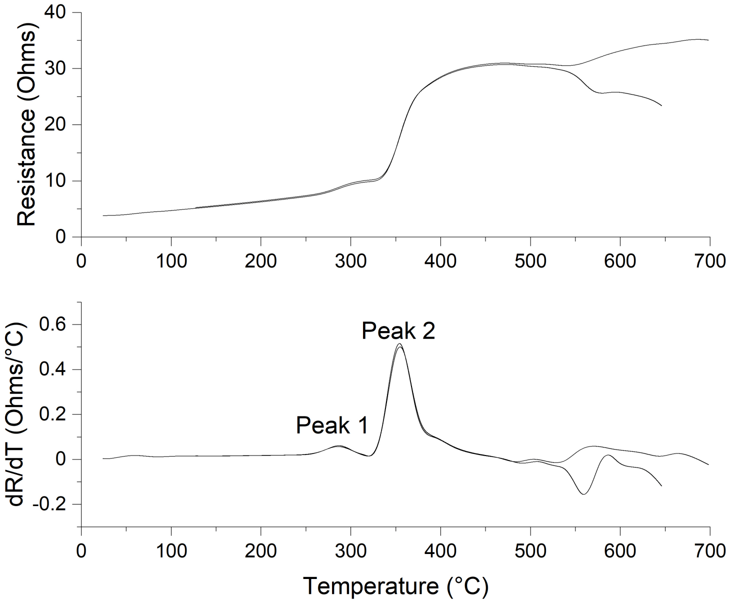

Figure 2.13: Data resulting from the 100 K/s power pulse shown in figure 2.12 applied two Ni/Al samples of type 2 in table 2.1 (200 nm Al). The top image shows the resistance over temperature, and below it is the plot of its derivative with respect to temperature. Two distinct peaks are indicated. Reprinted from Short et al. (2023)

To investigate the cause of peaks 1 and 2, different Ni/Al samples of type 2 were pulsed and quenched at various points of interest around these peaks, namely immediately before peak 1, between peak 1 and 2, and after peak 2. The derivatives of the resistance data from these pulses are shown in figure 2.14.

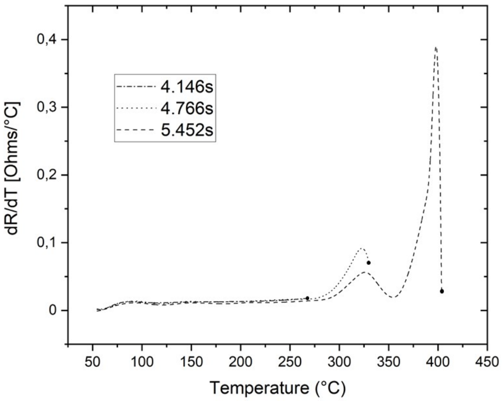

Figure 2.14: Data showing resistance over temperature of three different samples of type 2 in table 2.1 that were pulsed using the power pulse shown in figure 2.12 and quenched at points of interest around the two peaks shown in figure 2.13.

Using a Zeiss Crossbeam 550 L FIB from Carl Zeiss AG (Oberkochen, Germany), cross-sectional TEM lamellae were taken from each of the quenched samples, along with an untreated sample. STEM images of each of these samples, taken using the same FIB, are shown in figure 2.15. The as deposited sample (a) shows excellent separation of the Ni and Al layers, which, even before the first peak (b), are already seen to migrate into each other around the interface region with some peaks into presumed grain boundaries between Al grains. Based on these images, this morphology seems to be maintained after peak 1 (c). However, the heterogeneous layered structure is largely consumed during the second peak (d), and recrystallization and grain growth of new intermetallic crystals can be observed. While the cause of peak 2 is relatively clear from these images, the changes that led to the spike in resistance at peak 1 are not.

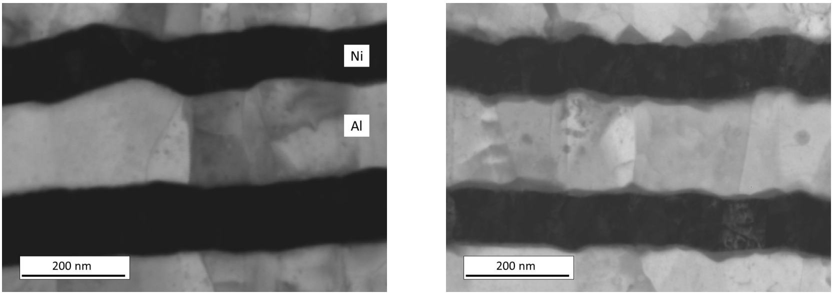

(a) Untreated

(b) Before peak 1

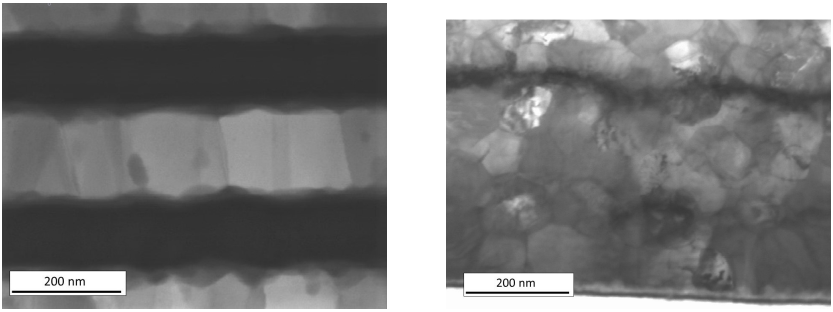

(c) After peak 1

(d) After peak 2

Figure 2.15: STEM-in-SEM images of cross sectional TEM lamella taken from Ni/Al samples of type 2 that were untreated (a) and pulsed using the power pulse shown in figure 2.12 to before the first peak (b), after the first peak (c), and after the second peak (d) as shown in figure 2.14. Ni is darker while the lighter areas show Al, as shown in subfigure (a). Reprinted from Short et al. (2023)

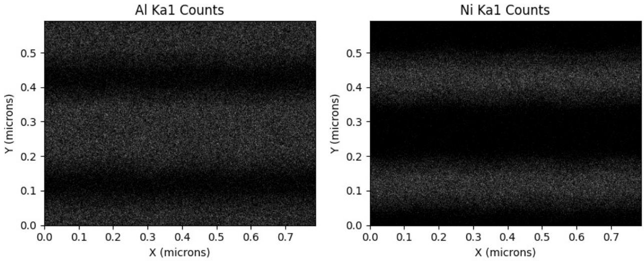

(a) Before peak 1

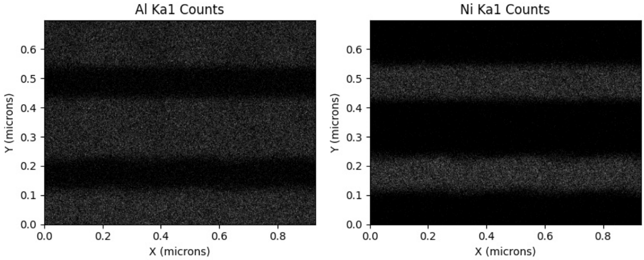

(b) After peak 1

Figure 2.16: EDX scans of the STEM images shown in figure 2.15 before and after peak 1 showing counts of photons from the Ka1 edge for Al and Ni.

2.2.1 EDX Linescans

Two dimensional EDX scans shown in figure 2.16 of the samples before and after peak 1 gave inconclusive results, and it was surmised that the spatial resolution was lacking. Since diffusion along heterogeneous interfaces tends to proceed at a rate similar to that of diffusion along grain boundaries (Kumar et al. 2018), it was predicted that the relatively faster diffusing Ni may have diffused through the Al grain boundaries after the visible intermetallic layer was built up along the interface. To test this, EDX linescans were taken along the Al layer, the results of which before and after peak 1 are shown in figure 2.17 and 2.18, respectively.

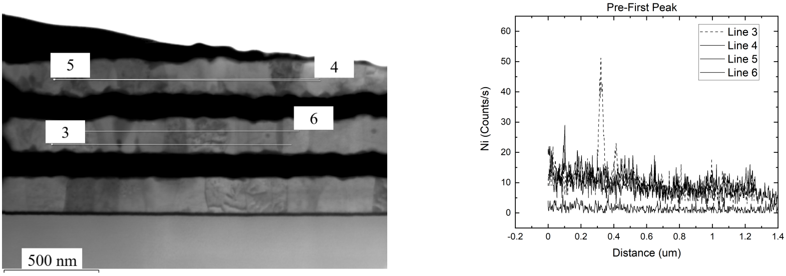

(a) STEM Image

(b) EDX Linescan

Figure 2.17: On the left is a STEM image of a Ni/Al sample of type 2 that was quenched before the first peak. EDX linescans were taken along the lines indicated in the image. The measured Ni distribution is plotted on the right. Reprinted from Short et al. (2023)

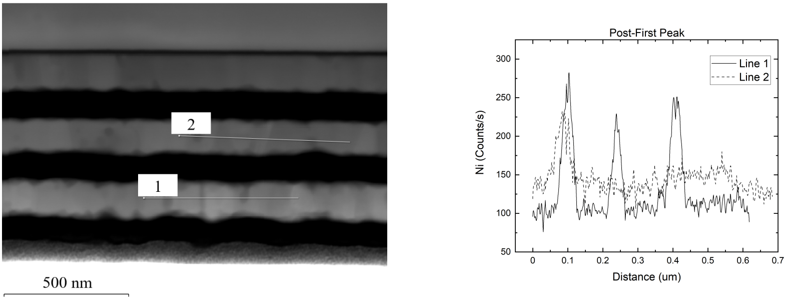

(a) STEM Image

(b) EDX Linescan

Figure 2.18: On the left is a STEM image of a Ni/Al sample of type 2 that was quenched after the first peak. EDX linescans were taken along the lines indicated in the image. The measured Ni distribution is plotted on the right. Reprinted from Short et al. (2023)

Linescan 2 from the post-peak sample demonstrates well the periodic peaks in Ni activity as expected from our prediction. It shows an average Al grain width of about $0.15\,\mu\mathrm{m}$. Linescan 1 also shows a peak, although some may be missing because, as we see from figure 2.14, the sample was quenched before the first peak completely subsided. In the pre-peak data we see only one such peak among much more data. Note that each scan in the pre-peak data was over twice as long as the scans in the post-peak data. In addition, scans 3 and 6 were taken much closer to the Ni/Al interface layer to catch any potential peaks that hadn't reached the center of the Al layer yet. This shows a substantial increase in Ni concentration within the Al grain boundaries occurring over peak 1, giving solid evidence to our theory.

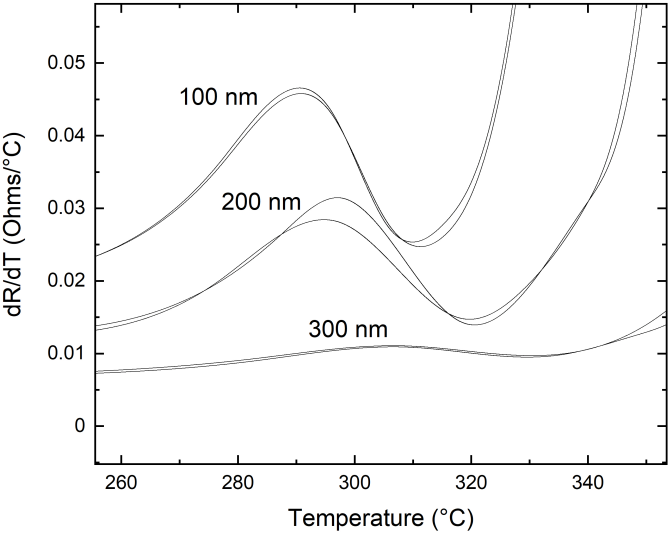

Figure 2.19: Data showing how peak 1 is modified by differing Al layer thicknesses, given the same linear 100 K/s pulse. Reprinted from Short et al. (2023)

When the same 100 K/s pulse is applied to samples 1 and 3 as well, we see not only a peak shift but a modification of the shape of peak 1 as well, as seen in figure 2.19. As the Al layer thickness increases, peak 1 shifts to higher temperatures and flattens out, becoming hardly noticeable at 300 nm. That the peak shifts to higher temperatures is logical, given the extra time and energy needed to allow the Ni to diffuse through the thicker Al region and contribute significantly to the coil's overall resistance. The disappearance of the peak at higher Al thicknesses is likely due to increasingly complex fast diffusion pathways through the Al layer. From the data presented in figure 2.18, we know that the Al grains are in the region of 150 nm, so at 300 nm thick, the Al layers in sample 3 already had a more complex network of grain boundaries instead of the straight pathways from Ni to Ni layers in samples 1 and 2.

2.2.2 Activation Energy

In order to measure the activation energy of the two peaks, a Kissinger analysis, first proposed by Kissinger (1956), was utilized in which the kinetics of the reaction can be related to the peak positions as follows,

$$\frac{d\left(\ln \frac{\beta}{\mathrm{T_{peak}}^2}\right)}{d\left(1/\mathrm{T_{peak}}\right)} = -\frac{E}{R} \tag{2.2}$$

where β is the heating rate, $\mathrm{T_{peak}}$ is the peak temperature, E is the activation energy, and R is the ideal gas constant. Heating rates of 25, 50, 100, and 200 K/s were applied to samples 1, 2, and 3 and the resulting peak shifts were analyzed. Plots of these data are shown in figure 2.20.

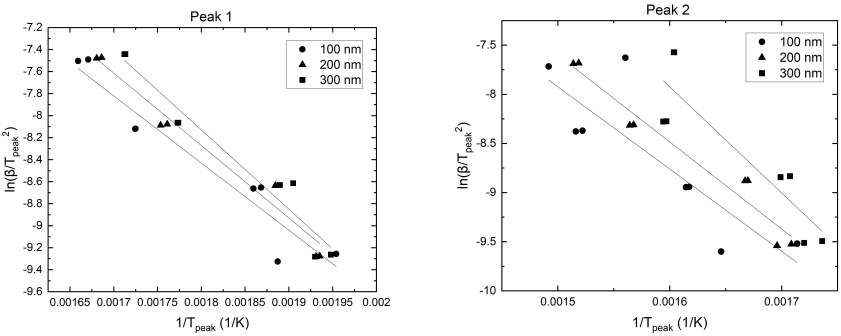

(a) Peak 1 **(b)** Peak 2

Figure 2.20: Kissinger plots showing the shift in peak 1 (a) and 2 (b) resulting from different linear heating ramps varying from 25 to 200 K/s applied to the Ni/Al samples. The different Al thicknesses for samples 1, 2, and 3 are indicated. Reprinted from Short et al. (2023)

The data shows some shift to the right as the Al layer thickness is increased, but the slope of the linear fits remained consistent as expected. The activation energies for peak 1 were 51±6, 55±4, and 60±6 kJ/mol, while for peak 2 they were 70±18, 74±7, and 90±18 kJ/mol for samples 1, 2, and 3, respectively.

2.2.3 Mechanical Characteristics

To measure the evolution of the elasticity and hardness of the Ni/Al film, specifically samples of type 2, an Agilent G200 Nanoindenter (Agilent Technologies) using a Berkovich tip was used on samples quenched at the temperature points indicated in figure 2.14, along with two extra temperature points immediately before and after the sample broke and became an open circuit. Between 16 and 25 measurements were taken along the third outermost ring of the heating spiral so as to match the data as closely as possible with its indicated temperature. These data are summarized in figure 2.21.

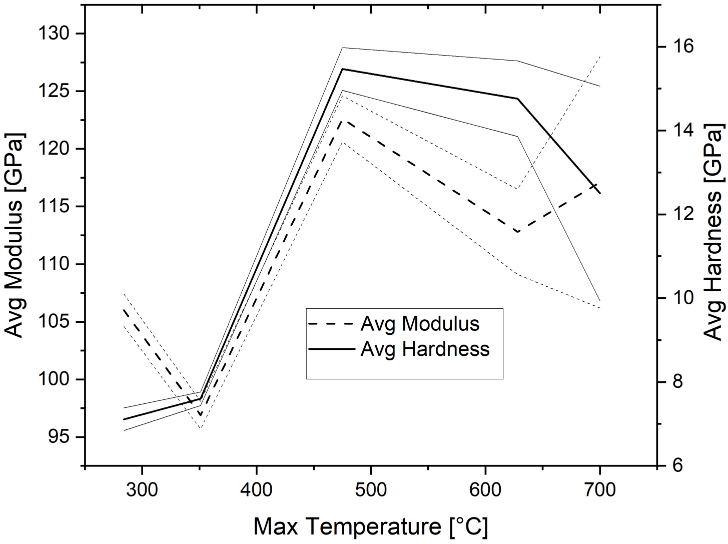

Figure 2.21: Elastic moduli and hardness data from nanoindentations taken with an Agilent G200 Nanoindenter (Agilent Technologies) on the third outermost ring of sample 2 (where temperature was measured) pulsed to various maximum temperatures shown along the x-axis. The upper and lower bound for ± 1 standard deviation are shown as accompanying thinner solid or dashed lines for the hardness and elasticity moduli data, respectively.

We see that, as the system passes through the first resistance peak, the indentation modulus drops somewhat while hardness remains unchanged. Both hardness and the indentation modulus increased dramatically after the second peak, after which the precision of the data dropped as shown by the widening of the $\pm 1\sigma$ bounds. This was likely due to the large buildup in residual stresses at this point which induced crack formation upon indentation, as noticed in the optical image shown in figure 2.22a. In the middle of the coil, where even higher temperatures were reached and where the open circuit likely occurred that led to failure of the device, SEM images shown in figure 2.22b reveal mud cracks on the surface of the film.

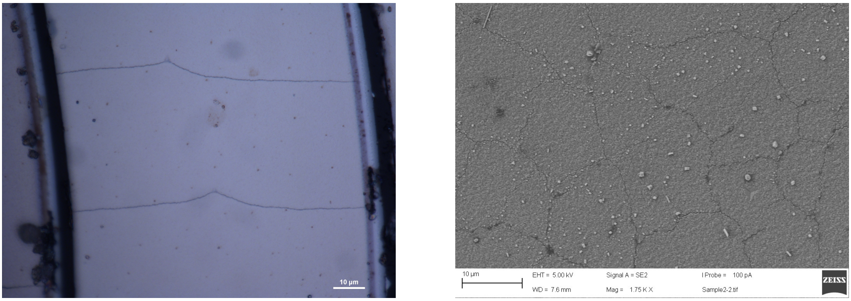

(a) Induced Cracks

(b) Mud Cracks

Figure 2.22: Images displaying different stress states of the Ni surface from a sample of type 2 pulsed at 100 K/s to failure (circuit break) occurring at around 700°C. Image (a) is from an optical microscope showing cracks in the third outermost ring induced by nanoindentation while image (b) shows an SEM image of one of the inner rings showing mudcracks.

2.3 Discussion

This section will aim to more precisely define the proposed mechanism of morphological transformation of the Ni/Al thin film bilayers under the applied temperature treatment and analyze whether this is physically realistic based on known parameters for the resistivity of Ni, Al, and their intermetallic compounds. Note that in this discussion, in the interests of brevity in text and equations, NiAl refers to any intermetallic alloy of Ni and Al unless otherwise stated.

Figure 2.25 displays again the resistance data of a 100 K/s pulse applied to sample 2 as initially shown in figure 2.13. In addition, The dotted line represents the calculated resistance of the third coil with respect to temperature given its geometry and assuming Al has a resistivity coefficient of $2.65 \times 10^{-8}\,\Omega\,\mathrm{m}$ with a temperature coefficient of $3.9 \times 10^{-3}\,\mathrm{K}^{-1}$ while Ni has a resistivity coefficient of $6.99 \times 10^{-8}\,\Omega\,\mathrm{m}$ with a temperature coefficient of $6 \times 10^{-3}\,\mathrm{K}^{-1}$. This underestimated the actual resistance measured at room temperature which was expected due to unaccounted effects such as grain size and interface roughness. To account for this, the line was shifted to match the data at room temperature as shown by the dashed line.

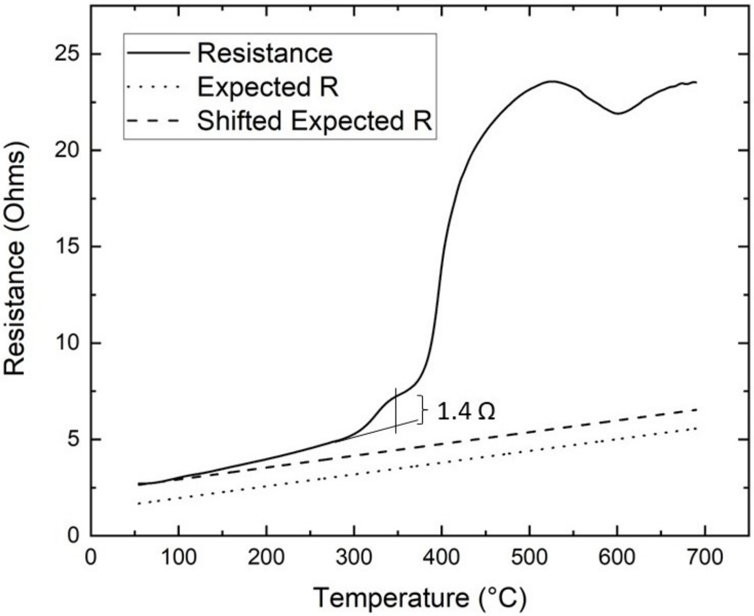

Figure 2.23: Resistance data from sample 2 pulsed at 100 K/s compared with expected resistance of the coil assuming no diffusion effects or structural or morphological transformations based on the resistivity of Ni and Al with respect to temperature. To match the initial measured resistance of the coil, this line was shifted up to better compare with the data. The difference in resistance between the actual sample and this line is shown as $1.4\,\Omega$. (Short et al. 2023)

We see that the shifted expected resistance follows the data almost identically until about 60-70°C, at which point it begins to deviate upwards. This is about the temperature that the thin films were deposited at, meaning it has already experienced this temperature range and any morphological changes that would have occurred are already present. After this point, the measured data deviate upwards, which is likely due to the formation of a layer of NiAl at the interface between the Ni and Al films, as can be seen in the STEM image of the sample before the first peak in figure 2.15b. This essentially "throttles" the more highly conductive Al layer gradually increasing the overall resistance.

The second major change that follows is the formation of intermetallics along the Al grain boundaries that further attenuates this conducting pathway. This scenario is depicted in figure 2.24 along with the dimensions for the average width of the Al grains, λ_{Al}, the average width of the NiAl region, λ_{NiAl}, and the thickness of the Al and Ni films, D_{Al} and D_{Ni}, respectively. These values were derived from the previously presented STEM and EDX data.

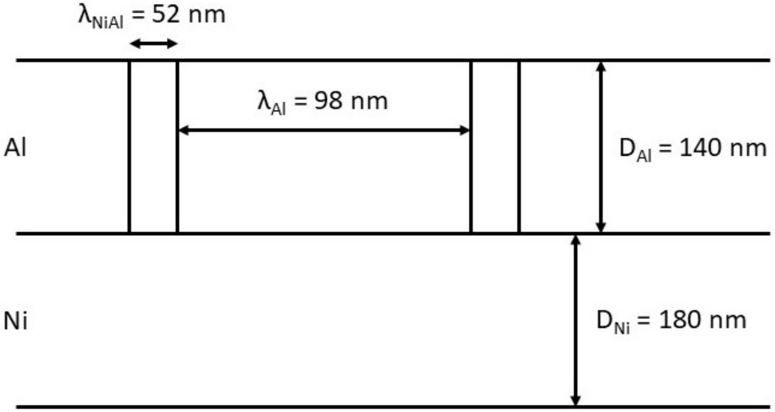

Figure 2.24: Diagram of the morphological situation of a single bilayer of sample 2 proposed to be present after peak 1, with NiAl regions formed within the grain boundaries of the Al layer. Reprinted from Short et al. (2023)

This situation was then reinterpreted as a circuit which is depicted in figure 2.25. Note the Ni and Al layers are in parallel, with the Al layer consisting of a repeating sequence of Al and NiAl grains.

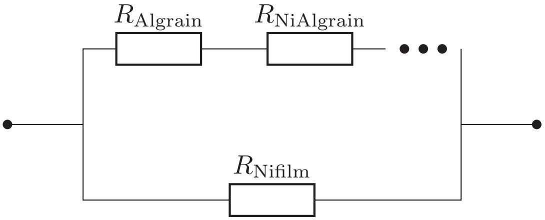

Figure 2.25: A reinterpretation of the situation depicted in figure 2.24 as a circuit with the Ni and Al films in parallel. The Al, NiAl grain sequence along the top layer is repeated along the length of the coil. Reprinted from Short et al. (2023)

The total resistance of the coil measured, R_T, can then be calculated as follows,

$$R_T = \frac{1}{n/R_{\text{Alfilm}} + n/R_{\text{Nifilm}}} \tag{2.3}$$

where n is the total number of bilayers (in our case 3), and R_{Alfilm} and R_{Nifilm} are the total resistances of the Al and Ni films, respectively. R_{Nifilm} can be calculated from its resistivity, ρ_{Ni}, as follows,

$$R_{\text{Nifilm}} = \frac{\rho_{\text{Ni}}\lambda_T}{wD_{\text{Ni}}} \tag{2.4}$$

where λ_T is the total coil length and w is the coil width. Calculating R_{Alfilm} requires the summation of the constituent Al and NiAl grains in series as follows,

$$R_{\text{Alfilm}} = \left(\frac{\rho_{\text{Al}}\lambda_{\text{Al}} + \rho_{\text{NiAl}}\lambda_{\text{NiAl}}}{wD_{\text{Al}}}\right)\frac{\lambda_T}{\lambda_{\text{Al}} + \lambda_{\text{NiAl}}} \tag{2.5}$$

where ρ_{Al} and ρ_{NiAl} are the resistivity of Al and NiAl and λ_{Al} and λ_{NiAl} are the average width of the Al and NiAl grains. The last term multiplies the resistance of two grains by the amount of Ni and NiAl grains in the coil length. A critique that may be raised here is against the assumption that the grains extend along the width of the coil, which is indeed not the physical case. However, when considering the total resistance, a staggered arrangement would just as effectively block off current flow. While we may underestimate the amount of NiAl present, thereby underestimating the total resistance, it nevertheless makes up a small proportion of the total structure and it is the morphological arrangement of the NiAl that is proposed to be most responsible for peak 1.

While the resistivity of Ni and Al are relatively easy to find on public databases, the resistivity of NiAl and vary considerably based on its distribution. According to Yamaguchi et al. (1968), at a 50-50 stoichiometric ratio it displays a low point of $1 \times 10^{-7}\,\Omega\,\mathrm{m}$ which quickly doubles to $2 \times 10^{-7}\,\Omega\,\mathrm{m}$ when the Ni ratio is increased to 52% or decreased to 49%. A compromise value of $1.5 \times 10^{-7}\,\Omega\,\mathrm{m}$ was taken due to this sensitivity. Using the equations given with the parameters claimed, if we increase λ_{NiAl} from 0 to 52 nm as measured after the first peak, the total resistance increases by $1.27\,\Omega$. This matches up very well to the $1.4\,\Omega$ difference in resistance between the measured sample and the resistance expected at that temperature if no morphological changes took place as shown in figure 2.23, even underestimating it by a slight amount as predicted earlier, although this could be due to differences from the actual value of the resistivity of NiAl.

2.4 Conclusion

The study explained in this chapter for the use of the thin film heating coil proposed focused on the control and manipulation of nano to microcrystalline structures. There are, however, many other potential usage scenarios for this device. One example that was investigated is surface modification of the thin film. It was noticed that, when measuring hardness and elasticity using a nanoindenter, different surface areas of the thin film were under different stress states after thermal pulsing to failure, meaning the circuit broke. Figure 2.22 shows two examples of this. In figure 2.22a we see an optical microscope image of the third outermost ring where temperature measurements were taken. After nanoindentation, cracks were induced that consistently spread out towards the sides of the ring, possibly indicating residual tensile stress that dominated in the direction along the coil. Subfigure b shows an SEM image of an area from the inner part of the coil that reached higher temperatures. Here the stresses built up more isometrically over the thin film surface resulting in a mud crack pattern.

Precise control of the surface stress state of the thin films via pinpoint temperature selection also allows the potential for advanced epitaxial grown regimes during thin film deposition (Headrick 2016). One potential usage of this is to create ultrasmooth coatings that have not only optical applications but also medical such as ultra-sterile surfaces whose low protein adsorption properties would hinder pathogen adhesion (Wang and He 2021).

Other surface modifications that are possible include inducing heat specific chemical reactions at the surface, allowing the selection of different functional groups to be attached at the surface. For example, in the presence of different atmospheres and temperature regimes, hydroxyl, carboxyl, or amino groups can be synthesized at the surface allowing for selective protein surface adsorption (Abdal-hay et al. 2022). Besides bioengineering artificial tissues and organelles as mentioned by Abdal-hay et al. (2022), different biosensors can be created allowing the detection of enzymes, antibodies, or nucleic acids through changes in pH, mass, surface potential, optical properties, or the production of a byproduct (Bhakta et al. 2015, Mehrotra 2016). This can be used for diagnostics, environmental monitoring, food safety, real time monitoring of biological processes, and quantification of relevant chemicals in biological samples. A biosensor with a precisely temperature controlled base offers the opportunity to more effectively utilize temperature dependent recognition elements, such as liposomes (Jose et al. 2019) and aptamers which have been used for the detection of specific cancer cells (Tang et al. 2017).

Solid state batteries, having a solid electrolyte, have been presented as an alternative to the liquid electrolytes in for example Li-ion batteries that have long been problematic due to their many different side reactions including the promotion of dendritic growth leading to system failure (Li et al. 2021). However, as we have seen, solids are not immune to similar effects. An example from Alexander et al. (2021) is shown in figure 2.26, where different models for dendritic growth of Li is shown through a solid electrolyte. The thin film heater presented in this chapter provides an excellent technique to detect this growth, and investigate strategies to mitigate it.

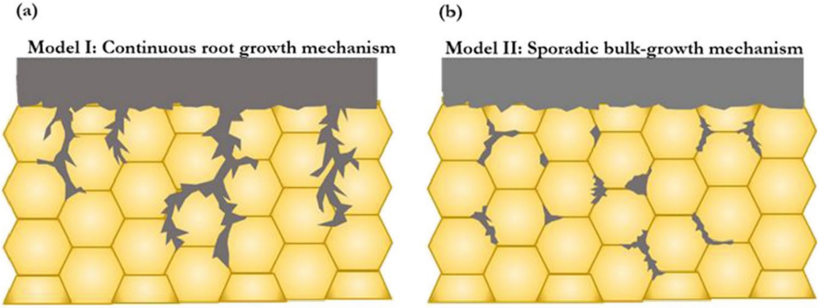
(a)
Model I: Continuous root growth mechanism
(b)
Model II: Sporadic bulk-growth mechanism

Figure 2.26: Diagram showing Li dendritic growth through a solid electrolyte. Reprinted with permission from G. V. Alexander, M. S. Indu, and R. Murugan, Review on the critical issues for the realization of all-solid-state lithium metal batteries with garnet electrolyte: interfacial chemistry, dendrite growth, and critical current densities, Ionics, 27, 4105-4126, 2021, Springer Nature.

3 Concentration Dependent Grain Boundary Diffusion

Chapter 3 is based on:
Short, M., & Woll, K. (2021). *An expansion of the Fisher Model for concentration dependent grain boundary diffusion.* Acta Materialia, 217, 117056.
10.1016/J.ACTAMAT.2021.11705
* This work was done under the supervision and direction of K. Woll.

As we have seen in chapter 2, fast diffusion pathways such as grain boundaries are an important phenomenon in the evolution of microstructures. One of the difficulties in properly measuring the diffusion coefficient for a material through a grain boundary, D_{gb}, is because of leakage of the diffusant material into the adjacent grains, effectively attenuating diffusion through the grain boundary. While numerous extraneous effects, such as grain boundary migration, Kirkendall effect, differing grain misorientations, precipitation, and phase change within the grain boundary, will alter the final concentration distribution measured after a thermal pulse excites a significant migration of diffusant through a grain boundary, an interest in solving the mathematical problem of measuring D_{gb} while taking leakage into account goes back to the 1950's with Fisher's model first proposed in his work Fisher (1951).

In this model, Fisher takes a situation such as that presented in figure 3.1 and derives a boundary condition for the change in concentration of the grain, c_g, at its interface with the grain boundary over time, t, as follows,

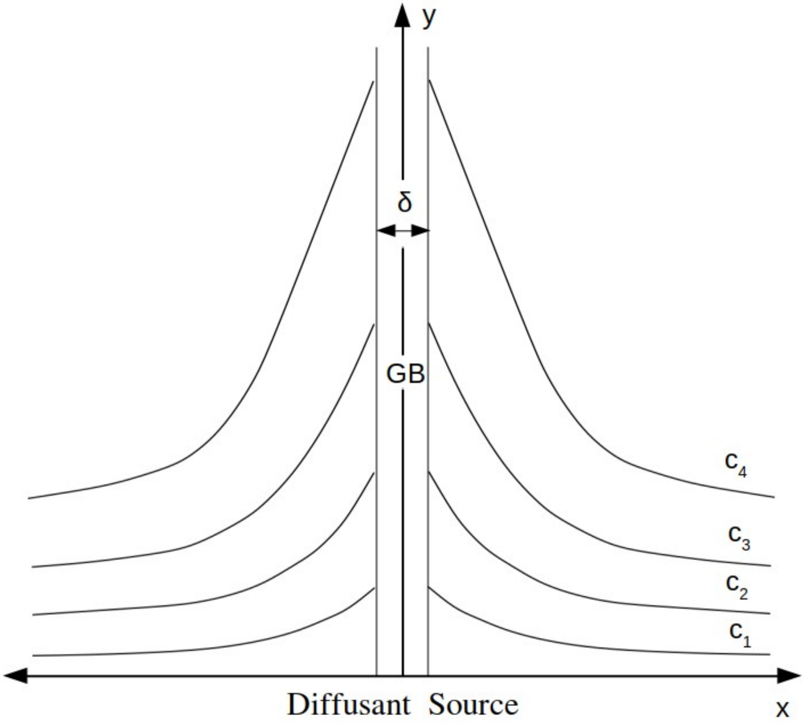

Figure 3.1: Graphical representation of the diffusion situation this chapter seeks to analyze. At the bottom is a diffusant source that diffuses upwards through the fast diffusion grain boundary (GB), with width δ, and outwards into the grains to the left and right. This forms diffusant "peaks" indicated by isoconcentration lines with concentrations $c_1 > c_2 > c_3 > c_4$. Reprinted from Short and Woll (2021)

$$\left.\frac{\partial c_g}{\partial t}\right|_{x=\pm\frac{\delta}{2}} = D_{gb}\frac{\partial^2 c_g}{\partial y^2} + \frac{2D_g}{\delta}\frac{\partial c_g}{\partial x} \tag{3.1}$$

where D_g is the diffusion coefficient within the grain, x and y refer to the axes shown in figure 3.1, and δ refers to the width of the grain boundary. The first term on the right is directly from Fick's second law of diffusion while the second term describes leakage ($\frac{\partial c_g}{\partial x}$ will be negative) directed orthogonally to the grain boundary. Note how if the grain diffusion coefficient is higher, leakage will increase.

Although this model has been used and modified extensively in the literature, one of its major assumptions is that D_{gb} is concentration independent, and therefore $\frac{\partial c_{gb}}{\partial t} = D_{gb}\Delta c_{gb}$ where c_{gb} is concentration in the grain boundary. Reports from about a decade later from Achter et al. (1959), Austin and Richard (1961, 1962) demonstrate this not to be a good assumption in every case, and so a modification of equation 3.1 is made here taking this into account.

3.1 Theory

We begin by clearly stating the primary assumptions we will make below.

1. Fick's laws governing diffusant flux, $\vec{J}$, are obeyed in the grain boundary and the grain.

   $\vec{J} = -D_g \nabla c_g$

2. D_{gb} is concentration dependent.

   $\frac{\partial c_{gb}}{\partial t} = \nabla \cdot (D_{gb}\nabla c_{gb}) \neq D_{gb}\Delta c_{gb}$

3. Diffusant concentration at the grain boundary/grain interface is related by a segregation factor, s, while the flux across this interface is continuous.

   a) $c_{gb}(\pm\frac{\delta}{2}, y, t) = s c_g(\pm\frac{\delta}{2}, y, t)$

b) $D_{gb} \left. \frac{\partial c_{gb}(x,y,t)}{\partial x} \right|_{x=\pm\frac{\delta}{2}} = D_g \left. \frac{\partial c_g(x,y,t)}{\partial x} \right|_{x=\pm\frac{\delta}{2}}$

4. Grain boundary width, δ, is very small so the variance of c_{gb} across x is negligible.

   $\frac{\partial c_{gb}}{\partial x} = 0$

All of these are largely the same as the assumptions Fisher used in his original paper, except for assumption 2. Since D_{gb} is not constant, we cannot ignore the gradient operator. Assumption 3a only adds in a segregation factor to the relation of concentration across the grain boundary/grain interface which is nonvariant with respect to concentration in the dilute limit case (Herzig and Divinski 2003) while the flux is kept continuous in the x-direction as before. Assumption 4 is a simplifying assumption as the grain boundary is often so small (∼5nm) that any concentration gradient across it in the x-direction is negligible when considering the overall diffusion kinetics. Since we are considering a 2-dimensional case, ∇ can be defined as $(\frac{\partial}{\partial x}, \frac{\partial}{\partial y})$. We can first expand assumption 2 for within and outside the grain boundary as follows,

$$\begin{aligned}\frac{\partial c_{gb}}{\partial t} &= \nabla \cdot (D_{gb} \nabla c_{gb}(x,y,t)) \\ &= \frac{\partial}{\partial x} D_{gb} \frac{\partial}{\partial x} c_{gb} + D_{gb} \frac{\partial^2}{\partial x^2} c_{gb} + \frac{\partial}{\partial y} D_{gb} \frac{\partial}{\partial y} c_{gb} + D_{gb} \frac{\partial^2}{\partial y^2} c_{gb} \text{ for } |x| \leq \frac{\delta}{2}\end{aligned} \tag{3.2}$$

$$\begin{aligned}\frac{\partial c_g}{\partial t} &= \nabla \cdot (D_g \nabla c_g(x,y,t)) \\ &= \frac{\partial}{\partial x} D_g \frac{\partial}{\partial x} c_g + D_g \frac{\partial^2}{\partial x^2} c_g + \frac{\partial}{\partial y} D_g \frac{\partial}{\partial y} c_g + D_g \frac{\partial^2}{\partial y^2} c_g \text{ for } |x| \geq \frac{\delta}{2}\end{aligned} \tag{3.3}$$

Now, a formula is needed to relate these two equations at the interface at $x = \frac{\delta}{2}$. We can begin by Taylor expanding c_{gb} around $x = 0$,

$$c_{gb}(x, y, t) \approx c_{b0} + \frac{x^2}{2} c_{b2} \tag{3.4}$$

where $c_{b0} = c_{gb}(0, y, t)$ and $c_{b2} = \left.\frac{\partial^2 c_{gb}}{\partial x^2}\right|_{x=0}$. Assumption 4 allows us to exclude higher order terms. For simplicity, before we substitute equation 3.4 into equation 3.2, some derivative terms can be analyzed first:

$$\frac{\partial^2}{\partial x^2} c_{b0} = 0 \tag{3.5}$$

$$\frac{\partial}{\partial x} c_{b0} = 0 \tag{3.6}$$

$$\frac{\partial^2}{\partial y^2} \left(\frac{x^2}{2} c_{b2} \right) = 0 \tag{3.7}$$

$$\frac{\partial}{\partial y} \left(\frac{x^2}{2} c_{b2} \right) = 0 \tag{3.8}$$

$$\frac{\partial}{\partial t} \left(\frac{x^2}{2} c_{b2} \right) = 0 \tag{3.9}$$

$$\frac{\partial^2}{\partial x^2} \left(\frac{x^2}{2} c_{b2} \right) = c_{b2} \tag{3.10}$$

$$\frac{\partial}{\partial x} \left(\frac{x^2}{2} c_{b2} \right) = \pm \frac{1}{2} \delta c_{b2} \tag{3.11}$$

Equations 3.5 and 3.6 are due to assumption 4, as the concentration is invariant in the x-direction. Equations 3.7 through 3.9 can be approximated as 0 since we will apply this boundary condition at $x = \frac{\delta}{2}$ and δ is very small. Substituting equation 3.4 into 3.2 then gives us,

$$\begin{aligned}\frac{\partial c_{gb}}{\partial t} = \frac{\partial}{\partial t}\left(c_{b0} + \frac{x^2}{2}c_{b2}\right) &= \frac{\partial}{\partial x}D_{gb}\frac{\partial}{\partial x}\left(c_{b0} + \frac{x^2}{2}c_{b2}\right) + D_{gb}\frac{\partial^2}{\partial x^2}\left(c_{b0} + \frac{x^2}{2}c_{b2}\right) \\ &+ \frac{\partial}{\partial y}D_{gb}\frac{\partial}{\partial y}\left(c_{b0} + \frac{x^2}{2}c_{b2}\right) + D_{gb}\frac{\partial^2}{\partial x^2}\left(c_{b0} + \frac{x^2}{2}c_{b2}\right) \\ &= \frac{\partial}{\partial x}D_{gb}\left(\pm\frac{1}{2}\delta c_{b2}\right) + D_{gb}c_{b2} + \frac{\partial}{\partial y}D_{gb}\frac{\partial}{\partial y}c_{b0} + D_{gb}\frac{\partial^2}{\partial y^2}c_{b0}\end{aligned} \tag{3.12}$$

Now we must relate the substitution terms c_{b0} and c_{b2} with c_g. c_{b0} can be related to c_g at the interface via assumption 3a as follows,

$$c_{b0} = sc_g(\pm\frac{\delta}{2}, y, t) \tag{3.13}$$

which can also be substituted into equation 3.12. If we substitute equation 3.4 into the flux continuity equation shown in assumption 3b we get,

$$\begin{aligned}D_{gb}\left.\frac{\partial c_{gb}}{\partial x}\right|_{x=\pm\frac{\delta}{2}} = D_{gb}\left.\frac{\partial}{\partial x}\left(c_{b0} + \frac{x^2}{2}c_{b2}\right)\right|_{x=\pm\frac{\delta}{2}} &= D_g\left.\frac{\partial c_g}{\partial x}\right|_{x=\pm\frac{\delta}{2}} \\ \pm\frac{1}{2}D_{gb}\delta c_{b2} &= D_g\left.\frac{\partial c_g}{\partial x}\right|_{x=\pm\frac{\delta}{2}}\end{aligned} \tag{3.14}$$

which shows us that $\pm\frac{1}{2}\delta c_{b2} = \frac{D_g}{D_{gb}}\left.\frac{\partial c_g}{\partial x}\right|_{x=\pm\frac{\delta}{2}}$ and $D_{gb}c_{b2} = \frac{2D_g}{\delta}\left.\frac{\partial c_g}{\partial x}\right|_{x=\pm\frac{\delta}{2}}$. If we apply these relations to equation 3.12 we get,

$$\begin{aligned}\left.\frac{\partial c_{gb}}{\partial t}\right|_{x=\pm\frac{\delta}{2}} = \left.\frac{s\partial c_g}{\partial t}\right|_{x=\pm\frac{\delta}{2}} &= \frac{D_g}{D_{gb}}\frac{\partial c_g}{\partial x}\frac{\partial D_{gb}}{\partial x} + \frac{2D_g}{\delta}\frac{\partial c_g}{\partial x} + s\frac{\partial c_g}{\partial y}\frac{\partial D_{gb}}{\partial y} + sD_{gb}\frac{\partial^2 c_g}{\partial y^2} \\ &= \frac{D_g}{D_{gb}}\frac{\partial c_g}{\partial x}\frac{\partial D_{gb}}{\partial x} + sD_{gb}\frac{\partial^2 c_g}{\partial y^2} + \frac{2D_g}{\delta}\frac{\partial c_g}{\partial x} + s\frac{\partial c_g}{\partial y}\frac{\partial D_{gb}}{\partial y}\end{aligned} \tag{3.15}$$

Since $\frac{\partial c_g}{\partial x}$ is zero due to assumption 4, we can eliminate the first term. Dividing by s and rearranging the terms to match Fisher's boundary condition gives us,

$$\left.\frac{\partial c_g}{\partial t}\right|_{x=\pm\frac{\delta}{2}} = D_{gb}\frac{\partial^2 c_g}{\partial y^2} + \frac{2D_g}{s\delta}\frac{\partial c_g}{\partial x} + \frac{\partial c_g}{\partial y}\frac{\partial D_{gb}}{\partial y} \tag{3.16}$$

This is the main result of this study and will often be referred to as equation 3.16 in the following text. Note that the first two terms are the same as Fisher's, although the leakage component is now attenuated by the segregation factor. Note that these are the same as those derived by Gibbs by including segregation effects (Gibbs 1966). The third term, sometimes called a reaction term in this context, takes into account the change in D_{gb} along the y-direction. The significance of this term will be evaluated in the following sections using finite difference modeling.

3.1.1 Analytical Solution

It would of course be much easier (and computationally less intensive) to calculate the concentration with respect to x and y after time t if we had an analytical solution for $c(x, y, t)$. As mentioned in the introduction, Whipple (1954) and Suzuoka (1961) came up with analytical solutions to Fisher's original model assuming an infinite and non-infinite source, respectively. To show why this is likely impossible with the modification to Fisher's boundary condition presented here, we can begin with a separation of variables approach. First, assume $c(x, y, t)$ can be written as a product of three functions each dependent on a single variable as follows,

$$c(x, y, t) = X(x) * Y(y) * T(t) \tag{3.17}$$

Substituting this equation into equation 3.16 and dividing both sides by $c(x, y, t)$, we get,

$$\frac{1}{T}\frac{\partial T}{\partial t} = \frac{D_{gb}(y)}{Y}\frac{\partial^2 Y}{\partial y^2} + \frac{2D_g}{s\delta X}\frac{\partial X}{\partial x} + \frac{1}{Y}\frac{\partial Y}{\partial y}\frac{\partial D_{gb}}{\partial y} \tag{3.18}$$

We already have T isolated to the left side of the equation, and X and Y isolated to the right side. For the equation to hold, both sides must be equal to some separation constant, let's say λ.

$$\frac{1}{T}\frac{\partial T}{\partial t} = \lambda \tag{3.19}$$

$$\frac{D_{gb}(y)}{Y}\frac{\partial^2 Y}{\partial y^2} + \frac{2D_g}{s\delta X}\frac{\partial X}{\partial x} + \frac{1}{Y}\frac{\partial Y}{\partial y}\frac{\partial D_{gb}}{\partial y} = \lambda \tag{3.20}$$

The equation for T is relatively easy to solve, and is given by $T(t) = A\exp(\lambda t)$ where A is some constant. Separating equation 3.20 gives us,

$$\frac{1}{X}\frac{\partial X}{\partial x} = \frac{s\delta}{2D_g}\lambda_x \tag{3.21}$$

$$\frac{D_{gb}(y)}{Y}\frac{\partial^2 Y}{\partial y^2} + \frac{1}{Y}\frac{\partial Y}{\partial y}\frac{\partial D_{gb}}{\partial y} = \lambda_y \tag{3.22}$$

Note that since the grain boundary diffusion coefficient is only valid along the y direction along the grain boundary, it could be separated from x. Equation 3.21 is solvable by integration in the same manner as T, but solving for $Y(y)$ is not possible due to the presence of $\frac{\partial D_{gb}}{\partial y}$. Even if we substitute a simple case such as the equation for a positive exponential dependence on concentration given in equation 3.27, the problem remains nontrivial due to the complex evolving nature of the gradient of D_{gb} along the grain boundary. Using another approach such as mapping onto another dimensional space using, for instance, a Fourier or Laplace transform would inevitably run into the same problem, and so needs no further discussion here.

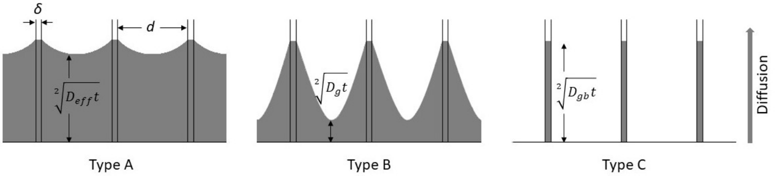

Figure 3.2: A graphic showing the three main Harrison Regimes described by Harrison (1961), consisting of parallel grain boundaries extending vertically from a diffusant source below with a horizontal spacing of d. The diffusant is shown here in gray.

3.1.2 Layer Averaged Diffusion

Measuring the concentration of radioactive tracer elements in a layer by layer fashion along the grain boundary axis has been a widely used technique for investigating grain boundary diffusion in the literature (Surholt et al. 1994, Divinski et al. 2007). While normally being the sum of radioactive activity over a 2-dimensional surface, for our simulation the layer averaged diffusant concentration, $\overline{c}$, will be the sum of the diffusant concentration within the grain boundary and the integral of diffusant over the x-axis as follows,

$$\overline{c}(y,t) = c_{gb}(y,t)\delta + \int_{\delta/2}^{x_{max}} c_g dx \tag{3.23}$$

As discussed in the introduction, diffusion within a polycrystalline material is a complex process, with many contributing factors influencing the diffusion kinetics. The primary factors considered here include the rate of diffusion within the grain, the grain boundary, the leakage from the grain boundaries into their surrounding grains, and the resulting volume diffusion around the grain boundaries. Most often, some of these factors dominate over the others, allowing the classification of "regimes". The oldest and most popular classification system is that of Harrison (1961), shown graphically in figure 3.2.

In a type A regime, volume diffusion dominates, and the diffusion field of each grain extends beyond their boundaries into the neighboring grains. Thus, the condition for this regime is that $\sqrt{D_g t}$ is much greater than d. This results in an approximately planar diffusion front with an effective diffusion coefficient of D_{eff}. According to Hart (1957), this can be expressed by the equation,

$$D_{eff} = fD_{gb} + (1 - f)D_g \tag{3.24}$$

where f is the volume fraction of grain boundary in the polycrystalline material.

For kinetics of type C, grain boundary diffusion completely dominates and any diffusion activity within the grain is minimal. This occurs when $\sqrt{D_g t} << s\delta$.

The most commonly occurring and studied regime within Harrison's classification is the type B regime. Here, grain boundary diffusion takes on a larger role, and the diffusion field of the grains no longer overlap as in the A regime. This effectively isolates each grain boundary, and allows the mathematical modelling and extraction of different parameters based on the shape of the surrounding diffusion front. A condition for this regime is that $s\delta << \sqrt{D_g t} << d$. Le Claire (1963) formulated an additional dimensionless parameter, β, given by,

$$\beta = \frac{s\delta D_{gb}}{2D_g (D_g t)^{1/2}} \tag{3.25}$$

which describes the "sharpness" of the peaks shown in the middle image of figure 3.2. This was derived from Fisher's original solution for the contact angle, ϕ, of the diffusion peak with the grain boundary. As the diffusion behavior tended from type A to type B, β increased, and a value of 10 is often given as a cutoff point between the two regimes. If the ratio D_{gb}/D_g is divided out, we get a parameter given as α in the literature (Mishin et al. 1997) which describes the the size of the diffusion field of the grain. A value less than 0.1 is often given as a cutoff point.

It was determined experimentally by Levine and MacCallum (1960) that, within the B regime, $\ln \bar{c}$ was linear when plotted with respect to $y^{6/5}$. Mishin et al. (1997) lists the various empirically formulated models for different values of β to extract the triple product, $sD_{gb}\delta$, from the slope of this line. However, in the interest of brevity, only the formula relevant to the conditions of the finite difference simulation described in section 3.2 will be given,

$$sD_{gb}\delta = 1.206 \left(\frac{D_g^{0.585}}{t^{0.605}} \right)^{1/1.19} \left(-\frac{\partial \ln \bar{c}}{\partial y^{6/5}} \right)^{-5/2.975} \tag{3.26}$$

which is valid when $10^2 < \beta < 10^4$. It should be noted that the conditions and models given above were not theoretically derived from any first principles, and so caution should always be taken to their application.

3.2 Finite Difference Simulation

A finite difference simulation was written in Matlab as the boundary condition derived was not included in any off the shelf simulation software. The code for this is given in the appendix. The implicit formulation was chosen as the explicit formula resulted in wild instabilities and vastly different results for slight changes in cell sizes and time steps. The simulation field consisted of a 50 x 50 cell grid with a height and width of $5\,\mathrm{\mu m}$ x $2\,\mathrm{nm}$. The entire field represented a single grain, where the left hand boundary was the grain boundary and the bottom was the diffusant source. This narrow field was chosen to highlight changes in concentration distribution that would occur around the grain boundary.

As there are many sources in the literature reporting that D_{gb} varies by a few orders of magnitude with respect to c_{gb} (Kube et al. 2010, Erdelyi et al. 1999, Erdélyi and Beke 2011, Holzapfel et al. 2003), simple exponential dependencies were chosen. These were formulated to have a value of $1 \times 10^{-15}\,\mathrm{m^2\,s^{-1}}$ at $c_{gb} = 0.5$ and vary by n orders of magnitude from $c_{gb} = 0$ to $c_{gb} = 1$. The case of a positive dependency is given below,

$$D_{gb} = 10^{-15+n(c_{gb}-0.5)} m^2/s \tag{3.27}$$

While a negative dependency was not found in the literature, to the best of the author's knowledge there is no obvious physical argument as to why this could not be the case. For this reason, it was considered as well.

$$D_{gb} = 10^{-15-n(c_{gb}-0.5)} m^2/s \tag{3.28}$$

Note that, although the concentration ranges given here vary from 0 to 100%, this can be scaled so as to stay within the dilute limit range.

Grain boundaries are considered fast diffusion pathways because they often exhibit diffusion coefficients multiple orders of magnitude higher than that of their neighboring grains (Mehrer 2007). For this reason, D_g was set to $10^{-20.5}\mathrm{m}^2\,\mathrm{s}^{-1}$ which was 4 to 5 orders of magnitude lower than D_{gb}, depending on c_{gb} and n. The lower boundary represents an interface that is also a high stress region and is therefore also a fast diffusion pathway (Mishin and Razumovskii 1992). For this reason, a diffusion coefficient along this interface was set to $1 \times 10^{-17}\,\mathrm{m}^2\,\mathrm{s}^{-1}$.

Finally, δ width was set to $0.5\,\mathrm{nm}$ which is a reasonable value for FCC metals (Gas et al. 1992, Sommer and Herzig 1992). A diffusing solute was then introduced evenly into the lower boundary at a rate of $0.01\,\mathrm{nm}^{-1}\,\mathrm{s}^{-1}$. The simulation was allowed to run with a time step of 0.2 seconds for a total of 4000 seconds.

3.3 Results and Analysis

Examples of the raw data resulting from this simulation are shown in figure 3.3. The x and y-axes were normalized to the standard diffusion length within the grain as follows,

$$\xi = \frac{x}{\sqrt{D_g t}}, \quad \eta = \frac{y}{\sqrt{D_g t}} \tag{3.29}$$

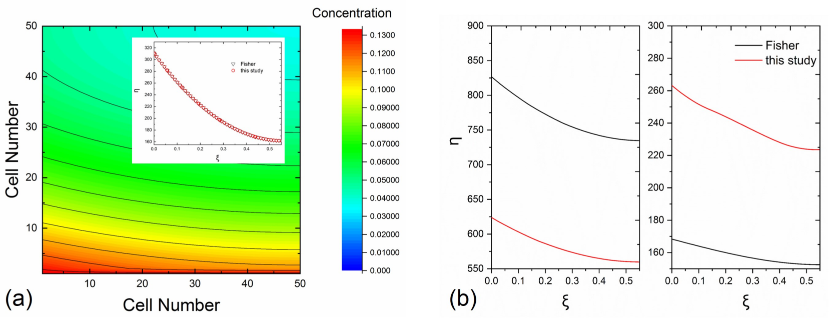

Figure 3.3: Raw data resulting from the finite difference simulation described in section 3.2. On the left is a map showing the final solute concentrations across the cells assuming D_{gb} was held constant at $10^{-15}\mathrm{m}^2\,\mathrm{s}^{-1}$. The black lines show isoconcentration curves while the insert shows the 10% isoconcentration curve using the Fisher model and the one derived in this study. On the right are the 10% isoconcentration curves for a negative (left graph) and positive (right graph) dependence of D_{gb} on c_{gb} where $n = 2$, with the axes normalized to standard diffusion lengths. Reprinted from Short and Woll (2021)

As a check to ensure the simulation was working correctly, D_{gb} was first held constant to $10^{-15}\mathrm{m}^2\,\mathrm{s}^{-1}$. This should cause the third term in equation 3.16 to collapse to zero, creating an identical result as Fisher's model. Figure 3.3a shows the result of this, with the insert revealing overlapping data for the two models along the 10% isoconcentration curve.

In figure 3.3b, equations 3.27 and 3.28 were substituted in for D_{gb} with $n = 2$. Here we already see a significant difference due to the third term in equation 3.16. For a positive dependency, the 10% isoconcentration point penetrated 56.3% further along the grain boundary, while for a negative dependency this depth was reduced by 24.5%. This general behavior makes sense given that, assuming $\frac{\partial c_g}{\partial y}$ is always negative, a positive dependency will cause the third term of the boundary condition to be positive, promoting diffusion, and vice-versa for a negative dependency. Figure 3.4a shows how this penetration depth changes when considering different diffusant concentration points. It seems that for for higher concentration points, this effect is exacerbated, indicating that $\frac{\partial c_g}{\partial y}\frac{\partial D_{gb}}{\partial y}$ has a far greater impact closer to the diffusant source where concentration is higher than farther away.

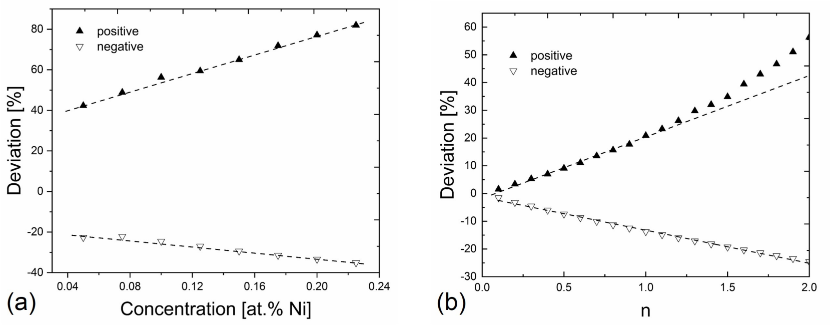

Figure 3.4: Data showing the percent change in penetration depth along the grain boundary given a negative and positive concentration dependency. Subfigure a shows this deviation with respect to the diffusant concentration point where $n = 2$. Subfigure b shows the penetration depth's dependency on n where the diffusant concentration considered was 10%. Reprinted from Short and Woll (2021)

A 2 order of magnitude difference between the grain boundary diffusion coefficient at 100% and 0% diffusant concentration has been noted to be reasonable based on values in the literature previously cited. However, even at this value for n we see quite a stark effect on the penetration depth. Since we know this change in penetration depth should tend to zero as n goes to zero, multiple simulations were run for values of n between 0 and 2 in order to evaluate at what point a significant deviation occurs. These results were plotted in figure 3.4b. We see a mostly linear relationship for both the negative and positive dependencies spreading away from a 0% deviation as n increases from zero, although the positive dependency inexplicably curves upwards after $n = 1.5$. For our simulation field, a 10% deviation in penetration depth translates to about 10 nm along the y-direction, which is measurable using modern TEM techniques. This would mean that, given our diffusion coefficients and flow rate, a measurable difference between the two models occurs when $n > 0.5$.

To compare the data from the simulation to radiotracer techniques commonly found in the literature, the layer averaged diffusant concentration was calculated using equation 3.23, the results of which are plotted in figure 3.5. To capture as much data on volume diffusion into the grain as possible, the simulation field

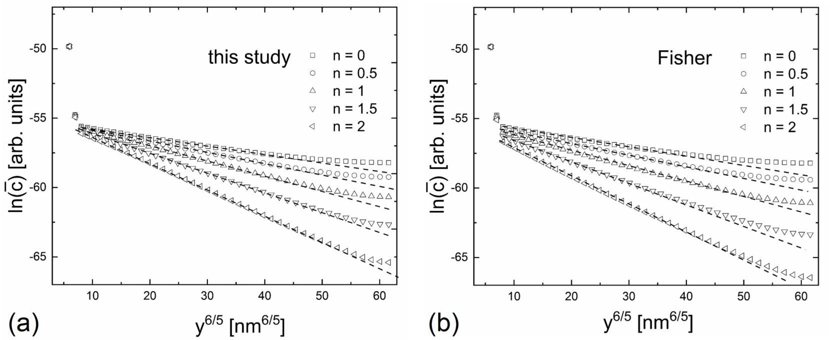

Figure 3.5: Data showing the result of applying equation 3.23 to our simulation results for a positive dependency using equation 3.16 as a boundary condition for the left side (a), and Fisher's model (b) with n ranging from 0 to 2. The simulation field was widened along the x-direction from 2 nm to 50 nm and shortened along the y-direction from 5 $\mathrm{\mu m}$ to 1 $\mathrm{\mu m}$. Linear trendlines were fitted to the data in the dilute region. Reprinted from Short and Woll (2021)

was widened along the x-axis to $50\,\mathrm{nm}$. At $5\,\mathrm{\mu m}$ from the diffusant source, the diffusant concentration became extremely diffuse, so the field was shortened along the y-axis to $1\,\mathrm{\mu m}$ to exclude any uninteresting data.

The general character of these data agree quite well with those in the literature (Divinski et al. 2010, Herzig et al. 2003, Kondavalasa et al. 2020, Glienke et al. 2020, Vaidya et al. 2016, 2018) in that they all show a sharp increase in $\ln \bar{c}$ as $y^{6/5}$ gets close to 0 and linearity of $\ln \bar{c}$ with respect to $y^{6/5}$ as the distance from the diffusant source is increased. The sharp increase near the interface can be explained by direct volume diffusion into the grain, which takes place along a larger x-range but is limited along the y-direction. Here, $\beta \approx 700$ and $\alpha \approx 0.07$ allowing us to apply equation 3.26 to recalculate D_{gb} from the data to see how accurately such a procedure on experimental data would predict this value. The results of this assuming a segregation of 1 are summarized in table 3.1.

These values show an underestimation of D_{gb} by a factor of between 2.69 and 4.46, with increasing accuracy as n increases. According to Szabó et al. (1990), when α is between 0.01 and 10, the system is in a transitional regime between B and C, and so a correcting factor can be calculated based on Suzuoka's solution

	n	Calculated D_{gb}	Expected D_{gb}
Modified	0	2.24×10^{-16}	1×10^{-15}
	0.5	1.49×10^{-16}	5.62×10^{-16}
	1.0	9.71×10^{-17}	3.16×10^{-16}
	1.5	6.12×10^{-17}	1.78×10^{-16}
	2.0	3.72×10^{-17}	1×10^{-16}
Fisher	0	2.24×10^{-16}	1×10^{-15}
	0.5	1.41×10^{-16}	5.62×10^{-16}
	1.0	8.76×10^{-17}	3.16×10^{-16}
	1.5	5.35×10^{-17}	1.78×10^{-16}
	2.0	3.22×10^{-17}	1×10^{-16}

Table 3.1: Calculated and expected values of D_{gb} from applying equation 3.26 to the data shown in Figure 3.5. Expected D_{gb} is derived from Equation 3.27 at the dilute limit ($c_{gb} = 0$) with the given value of n.

(Suzuoka 1961) to Fisher's model that relates the apparent and true value of D_{gb}. This is dependent on $\alpha w^{4/5}$ where w is the reduced penetration depth given by $w = \frac{y}{\sqrt{s\delta D_{gb}}}\left(\frac{4D_g}{t}\right)^{1/4}$. Assuming y is the height of the simulation, $\alpha w^{4/5} = 0.46$, which gives a ratio of 4-5 between the apparent and true value of D_{gb}.

While it may be tempting to compare the relative accuracy of the modified and Fisher models based on these values, they were the result of different simulations with a different boundary condition. How well equation 3.26 predicts D_{gb} is a reflection of its applicability (and the applicability of the modeling and theory built around radio-tracer diffusion methods over the years as summarized by Mishin et al. (1997)) to the data, and not the veracity of the two models considered. However, what these results do tell us is that using radio-tracer techniques to verify the modified model would be difficult, as the result of a numerical simulation using a modified model may be challenging to distinguish from one using Fisher's boundary condition.

Arguably the most noteworthy contribution in recent decades to finding a solution to Fisher's model for the case of concentration dependent grain boundary diffusion was by Rabkin (1996). While originally modeling a step wise concentration dependence of D_{gb} due to different phases present in the grain boundary, this was generalized to a continuous case by the following equation,

$$(D_{gb}\delta s)_{y_o} = \frac{2\sqrt{\frac{D_g}{\pi t}} \displaystyle\int_{y_o}^{y^*} c(y)dy + \left|\frac{\partial c}{\partial y}\right|_{y^*} (D_{gb}\delta s)_0}{\left|\frac{\partial c}{\partial y}\right|_{y_o}} \tag{3.30}$$

where D_{gb} is effectively calculated for the concentration at some point y_0, given a constant and known segregation factor. One way of interpreting the integral term is as a corrective factor between the diffusant flux (multiplied by δs) at y_0 and y^*, where y^* is a point far enough above y_0 to be close to the dilute limit. The results of applying this equation to the data from the simulation are shown in figure 3.6 where the lines represent the calculated D_{gb} from Rabkin's equation and the points are values originally input into the simulation for that respective concentration.

Note that D_{gb} was only calculated using equation 3.30 at concentration values actually measured at the discretized points along the grain boundary in the y-direction. We see very good agreement in the case of a positive dependency, and little if any in the case of a negative dependency. This may speak to either how realistic such a negative dependency is, or the applicability of Rabkin's equation, although, in the opinion of the author, it is more likely the former as Rabkin's equation is not empirically derived and doesn't make assumptions with respect to either dependency.

The work of Bernardini et al. (2003) showed that curvature in diffusion profiles commonly seen in polycrystals within the B regime are the result of non-linear segregation of diffusants. This segregation can be defined as $s = \left.\frac{c_{gb}}{c_g}\right|_{x=\pm\delta/2}$. We can see from equation 3.16 that for $s > 1$, leakage will be attenuated and

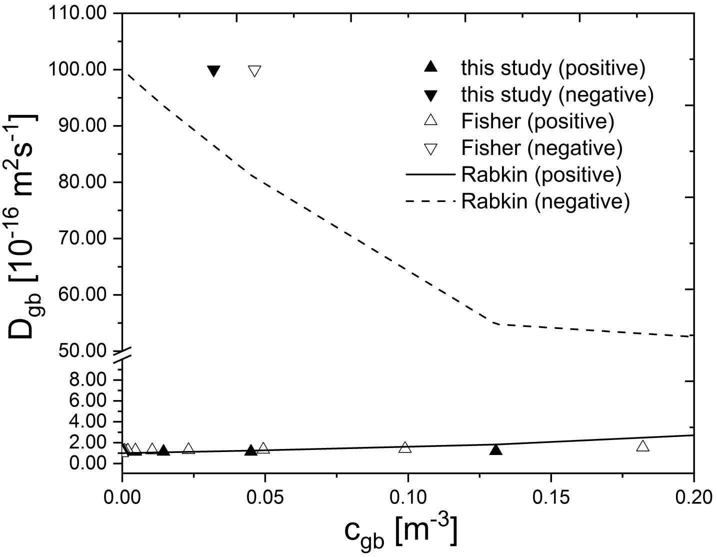

Figure 3.6: Results of applying Rabkin's solution shown in equation 3.30. Reprinted from Short and Woll (2021)

diffusion promoted along the grain boundary. This means that the regime will be shifted towards the C regime as s increases.

In a similar graphic as figure 3.4, figure 3.7 shows the deviation of the modified model from the Fisher model for increasing values of s given a positive and negative dependency. This deviation is significantly stronger for a positive dependency, and they both seem to saturate asymptotically. This is logical given that the dependency on s has the form of $1/s$, which naturally has an asymptotic curve.

The layer averaged concentration is again plotted for different segregation values in figure 3.8. While the simulations where $s = 5, 10$ were arguably within B-type kinetics, they were close enough to being within a C regime that the data was

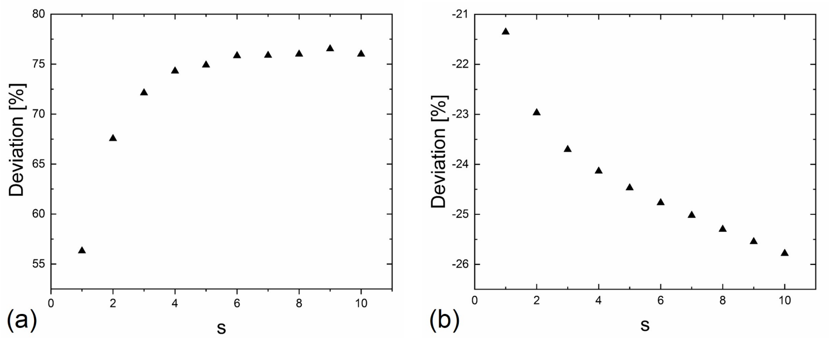

Figure 3.7: Data showing the % deviation from the Fisher model given various values of s for a positive (a) and negative (b) concentration dependency. Reprinted from Short and Woll (2021)

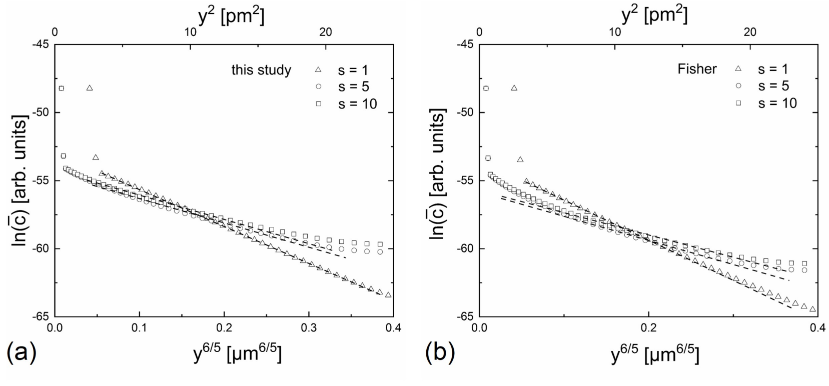

Figure 3.8: Figure showing the data from simulations using different values for s, layer averaged using equation 3.23. To account for the resulting different Harrison regimes, $s = 1$ is plotted over $y^{6/5}$ while $s = 5, 10$ are plotted over y^2. Reprinted from Short and Woll (2021)

plotted against y^2 instead of $y^{6/5}$. This allowed the application of the following formula

$$D_{gb} = \frac{1}{4t}\left(-\frac{\partial \ln \overline{c}}{\partial y^2}\right)^{-1} \tag{3.31}$$

taken from Divinski et al. (2007) which allowed a far simpler back calculation of D_{gb} as leakage effects were nearly negligible. The resulting D_{gb} was 2.3-2.8 times higher than the expected value, with an insignificant difference between the modified and Fisher models.

3.4 Conclusion

Via finite difference element simulation, this chapter has shown that by adding the term $\frac{\partial c_g}{\partial y}\frac{\partial D_{gb}}{\partial y}$ to Fisher's boundary condition to account for concentration dependence of D_{gb} within a range smaller than values commonly reported in the literature, a significant spatial deviation in isoconcentration curves is seen that would be measurable using modern TEM techniques such as EDX or Electron Energy Loss Spectroscopy (EELS) mapping. This extra term was derived from the well established Fick's laws of diffusion, along with some reasonable assumptions listed in the beginning of section 3.1. Therefore, mathematically the new boundary condition presented is sound, but whether it is useful in an experimental setting has yet to be determined.

A very similar approach that may be of interest to the reader is that of Benoist and Martin (1975), who applied a finite difference simulation to determine the leakage rate from the grain boundary to the surrounding grain. They did not derive their work directly from Fisher, but instead assumed the grain boundary to be a series of parallel "lanes" of fast diffusion, and each node was assigned a certain jump frequency to its neighboring node, with jumps along the fast diffusion lanes being promoted. While not directly addressing concentration dependent grain boundary diffusion, it would be possible to extend their approach to take this into account.

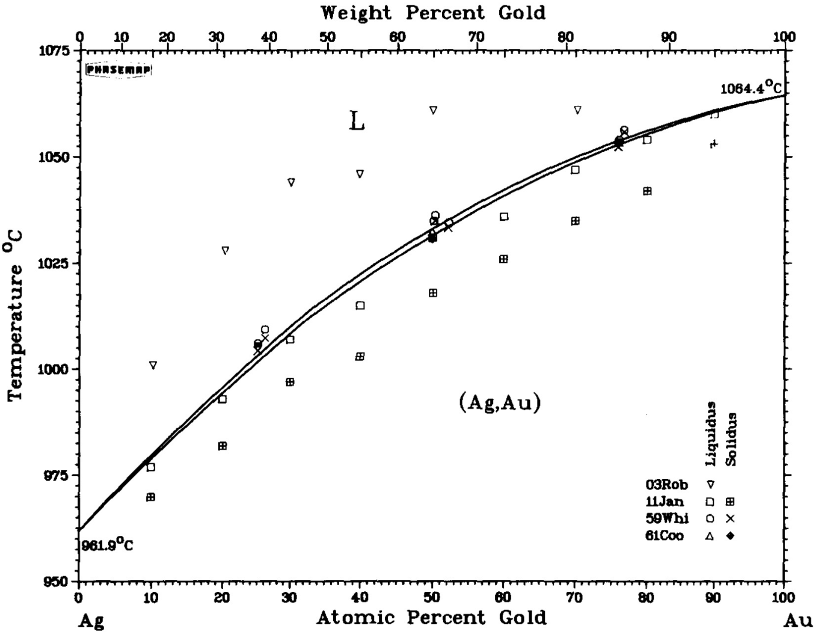

Figure 3.9: Gold-Silver phase diagram showing a single phase at any mixing ratio. Reprinted with permission from H. Okamoto and T.B. Massalski, The Ag-Au (Silver-Gold) system, Bulletin of Alloy Phase Diagrams, 4, 30-38, 1983, Springer Nature.

A primary difficulty of experimentally confirming the theoretical model presented here is not only the many different physical effects that inevitably take place when a polycrystalline sample is heated such as grain boundary migration, but also phase changes within the grain boundaries. This will result in discontinuous changes in D_{gb} with respect to c_g. One way to overcome this is to use a binary alloy where both elements create an identical elementary unit structure, resulting in a unitary phase at any mixing ratio. A gold-silver alloy is an excellent example of this, as shown in figure 3.9.

A very high resolution (<1 nm) TEM technique such as High Resolution Transmission Electron Microscopy (HRTEM) could then be used to search for and map out the resulting peaks. An example of this applied to the Ni/Al multilayers is

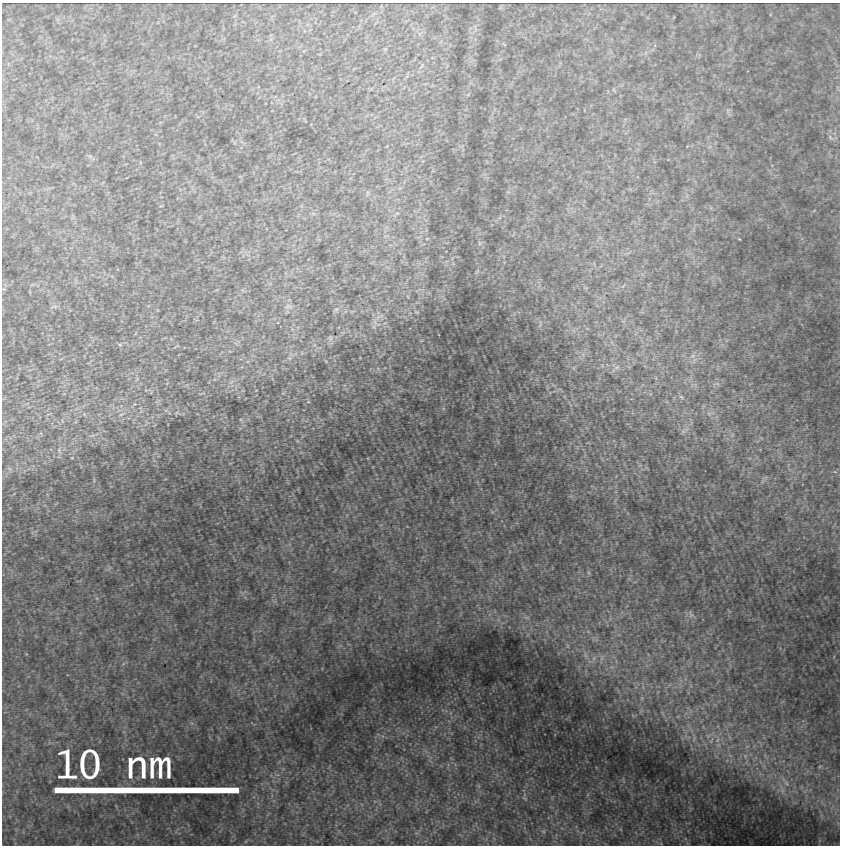

Figure 3.10: HRTEM image of a site within the Ni/Al multilayer where Ni has diffused from the bottom of the image into the Al layer above, separated into two grains by the approximately vertical grain boundary just right of center. Diffusion was clearly promoted through the Al grain boundary forming a characteristic peak in the surrounding intermetallic phases.

shown in figure 3.10, where Ni has diffused from the below into the Al layer above, with diffusion promoted by the approximately vertical grain boundary resulting in peaks as predicted earlier in this chapter. Attempts to quantify a diffusion coefficient for this boundary layer were hampered by the fact that the different intermetallic phases formed will have discontinuous diffusion coefficients.

As explained by Wu et al. (2014) and mathematically modeled by Vignes and Birchenall (1968), the varying melting point of the Ag-Au mixture implies concentration dependence of their diffusion coefficients. This presents an excellent case material to experimentally verify equation 3.16. The data that was layer averaged to reflect the results of radio-tracer diffusion measurements showed that such a method is not ideal to differentiate between the Fisher and modified boundary condition presented here. It is therefore the author's recommendation to use TEM methods instead, as they would likely be best able to distinguish the small deviations in isoconcentration lines. Numerical simulations would be useful here to select experimental parameters that would best facilitate measurements within the spatial sensitivity of the TEM system utilized.

Section 2.4 gives a list of interesting research domains and engineering applications that would be aided by better understanding grain boundary diffusion. The theoretical development in this chapter may help facilitate these pursuits and provide deeper insights into the underlying mechanisms at play. However, it should be noted that, mathematically, diffusion in solids behaves almost identically to that of heat diffusion, and so the boundary condition derived here can also be applied to fast heat conductive pathways with a temperature dependent thermal conductivity. The boundary condition could then be rewritten as,

$$\left.\frac{\partial T}{\partial t}\right|_{x=\pm\frac{\delta}{2}} = \alpha_{gb}\frac{\partial^2 T}{\partial y^2} + \frac{2\alpha_g}{\delta}\frac{\partial T}{\partial x} + \frac{\partial T}{\partial y}\frac{\partial \alpha_{gb}}{\partial y} \tag{3.32}$$

where T is temperature and α_{gb} and α_g are the thermal diffusivity of the grain boundary and grain, respectively, given by their thermal conductivity divided by their specific heat capacity and density. Segregation is excluded as it is not relevant here.

Such a development may prove useful in the field of thermoelectrics, where minimizing thermal conductivity enhances the Seebeck Coefficient and thereby the thermoelectric quality of a material. Snyder and Toberer (2008) gave a review explaining this and potential developments in this field, which has attempted to make greater use of nanostructured materials as further detailed by Dresselhaus et al. (2007) and Chen et al. (2003). Such heterogeneous materials would inevitably present a complex network of different thermal conductivities, and a precise modeling of their thermodynamic properties would prove useful to optimizing their design. Most of the work on reducing thermal conductivity in thermoelectrics has taken the physical approach of increasing phonon scattering and reducing its mean free path through, for example, the introduction of point defects (Pei et al. 2016) or creating a finely grained structure through ball milling and the use of a loose, "rattler" ion (Short et al. 2015). Combining this work with a heat diffusion model may contribute to a better understanding of thermal transport physics.

4 PCR Cycler

* This chapter contains proprietary work detailing ideas and designs conceived by the author, M. Short, while funded by the German Research Foundation (DFG) within the Emmy-Noether-Program (funding number: WO 2198/1-1) under the supervision of K. Woll. Photolithography was performed by H. Fornasier, while the gold films were deposited by T. Rupp. The SiN, SiC, and Teflon films were deposited by C. Savio. PCR solutions were provided by J. Müller who also gave much needed consultation with regards to this technology, while preparation of the assays and their analysis were done by D. Hellmann.

4.1 PCR Background

The aim of PCR is in essence to emulate the way cells duplicate DNA during replication processes such as mitosis. While cells use different enzymes for the various steps of the process, this can mostly be replaced with thermal cycling in the lab to better control the process. Figure 4.1 shows the structure of DNA, showing the sugar-phosphate backbone with the 3’ and 5’ (pronounced 3 prime and 5 prime, respectively) ends indicated. These are derived from the fact that the functional group at each respective end, phosphate for the 5’ and hydroxyl for the 3’ direction, are attached to the 5th and 3rd carbon atom on the nucleotide pentose-sugar-ring. This determines directionality, which will be useful later. The nucleobases (adenine, guanine, thymine, and cytosine) are covalently bonded to the 1st carbon atom on this ring. These are then hydrogen bonded, shown by the dotted lines, to their complementary nucleobase. As shown by the structure of these bonds, guanine only bonds with cytosine and vice versa, and thymine only bonds with adenine and vice versa.

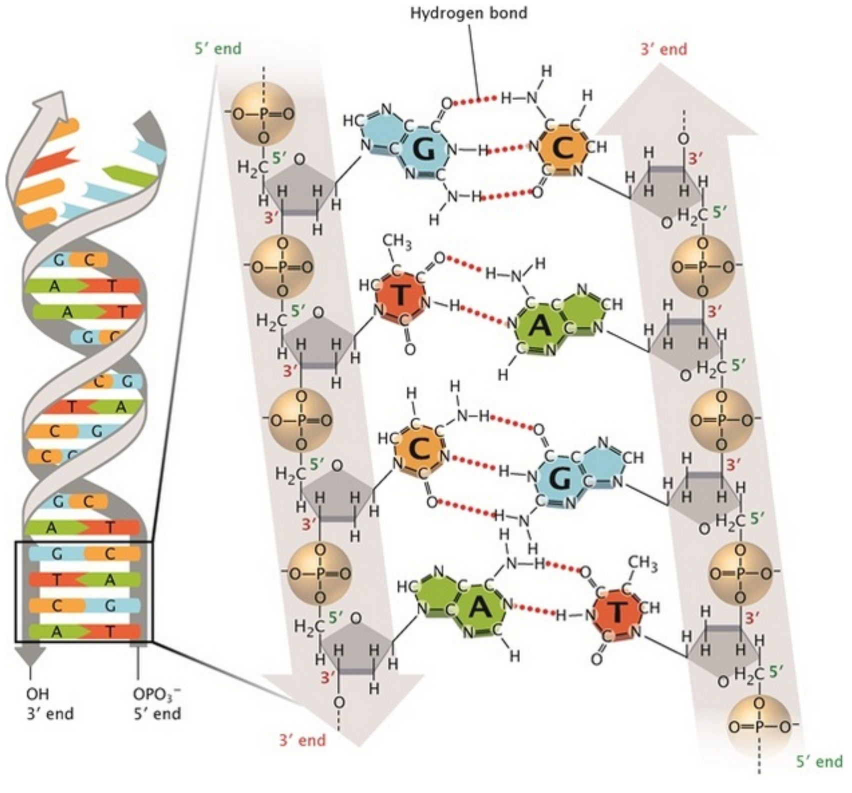

Figure 4.1: An image showing the molecular makeup of DNA. Covalent bonds are indicated by solid lines while dotted lines indicate hydrogen bonds. Reprinted under fair use from Pray (2008).

To begin the duplication process, the relatively weak hydrogen bonds can be broken by increasing the temperature to 92-98°C, effectively "unzipping" the DNA, otherwise referred to as denaturing. The two halves are contained in a solution full of nucleobases in the form of Dideoxynucleotide Triphosphates (dNTPs), but they will not individually attach yet to recreate the original DNA strand. To start this process, a "primer", consisting of a short single stranded DNA sequence (oligonucleotide), must first attach to one of the DNA halves where their sequences match in what is called annealing. To do this, the solution is cooled to a temperature where the hydrogen bonds can form (around 45-65°C depending on the primer’s sequence and length). It is then heated up again to around 72°C at which point an enzyme called DNA polymerase attaches to the 3’ end and travels in the 5’ to 3’ direction attaching complementary nucleobases in what is called the extension step. The denaturing, annealing, and extension steps constitute one cycle, which effectively doubles the amount of the original DNA sequences between the forward and backward primers in the solution. If repeated, this results in an exponential increase, which would result in over 1 trillion copies after 40 cycles assuming perfect replication. Note that replication can only occur if there exsists a sequence of nucleobases in the original DNA sample that matches the sequence contained in the primers. This is what makes this method useful for diagnostics, as the primer can be synthetically created to match a sequence of nucleotides only found in the DNA of a specific pathogen.

4.1.1 PCR Product Analysis

Various methods can be used to analyze the product of PCR and determine whether a successful reaction took place. The most common and straightforward method is Agarose Gel Electrophoresis, an example of which is shown in figure 4.2. This takes advantage of the fact that DNA and RNA molecules are large and negatively charged. After PCR has been completed, the resulting sample mixed with a fluorescent tag such as ethidium bromide is placed in an agarose gel. An electrical potential is then applied across the tray containing the gel. The DNA will migrate towards the positively charged side, the speed of which is inversely proportional to the logarithm of the amount of base pairs. Applying UV light will then cause the fluorescent tag to fluoresce, revealing the location of any DNA within the gel. In the figure one can see how the DNA fragments with fewer base pairs migrate faster, allowing the identification of the DNA sequence targeted with the primer. In this case a sequence of 800 base pairs was used to identify a virus infecting onions, with a positive result in 3 of the 4 samples.

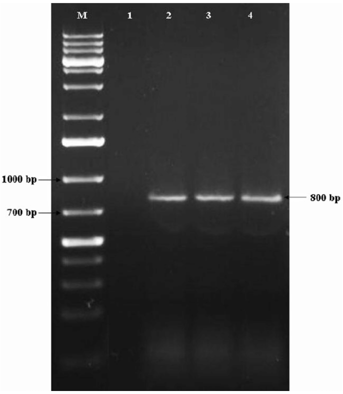

Figure 4.2: An example of agarose gel electrophoresis showing the result of a PCR test for Groundnut bud necrosis virus in onions (*Allium Cepa*). Well 1 shows a negative result, while 2-4 are positive. Reprinted with permission from A. Sujitha et al, First report of Groundnut bud necrosis virus infecting onion (Allium cepa), Australasian Plant Disease Notes, 7, 183-187, 2012, Springer Nature

Another strategy is real-time PCR or quantitative PCR also known as Quantitative Polymerase Chain Reaction (qPCR) (note that RT-PCR stands for Reverse Transcription PCR). Here, the degree of fluorescence of the PCR product is measured after each cycle, allowing both a timely result and a quantification of the amount of targeted DNA in the original sample. There are two main methods of fluorescent detection: DNA binding dyes and fluorescently labeled probes.

With DNA binding dyes, a fluorescent dye such as SYBR Green fluoresces as it binds to double stranded DNA (although some signal is seen with single stranded DNA and RNA). Here, the fluorescent intensity is directly proportional to the amount of replicated target DNA, which exponentially increases as the solution is thermally cycled. Fluorescently labeled probes involves using reporter probes containing the target DNA sequence. Each probe has a fluorophore at one end and a quencher at the other, which prevents fluorescence due to Förster resonance energy transfer. When the probe binds to its target sequence and extension begins, the polymerase degrades the probe, separating the fluorophore from the quencher, resulting in fluorescence. This has the noted advantage of offering the ability to simultaneously detect multiple different target sequences using various probes with differently colored markers. Figure 4.3 from the work of Nolan et al. (2006) shows an example of this using DNA binding dyes with primer concentrations ranging from 50-600 nM.

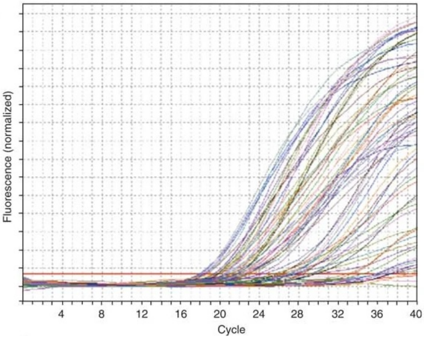

Figure 4.3: qPCR results on mouse DNA using primers targeting the hepcidin 1 gene with concentrations varying from 50-600 nM. Reprinted with permission from T. Nolan, R. E. Hands, and S. A. Bustin, Quantification of mRNA using real-time RT-PCR, Nature Protocols, 1, 1559-1582, 2006, Springer Nature.

4.2 Current Rapid PCR Strategies

Increasing and decreasing the temperature of the assay can be very time consuming, and a standard amount of cycles (∼35-40) normally takes about an hour using off the shelf thermal cyclers. Various strategies have been proposed and tested to address this, some of which will be presented here. One of the most notable earlier attempts from the late 90's at extremely rapid PCR was the work of Kopp et al. (1998) which used serpentine microfluidic channels which passed through regions held at the respective temperatures for denaturing, annealing, and extension. The device setup is shown in figure 4.4, which achieved a successful 20 cycle amplification of a 187 base pair fragment in a staggering 90 seconds.

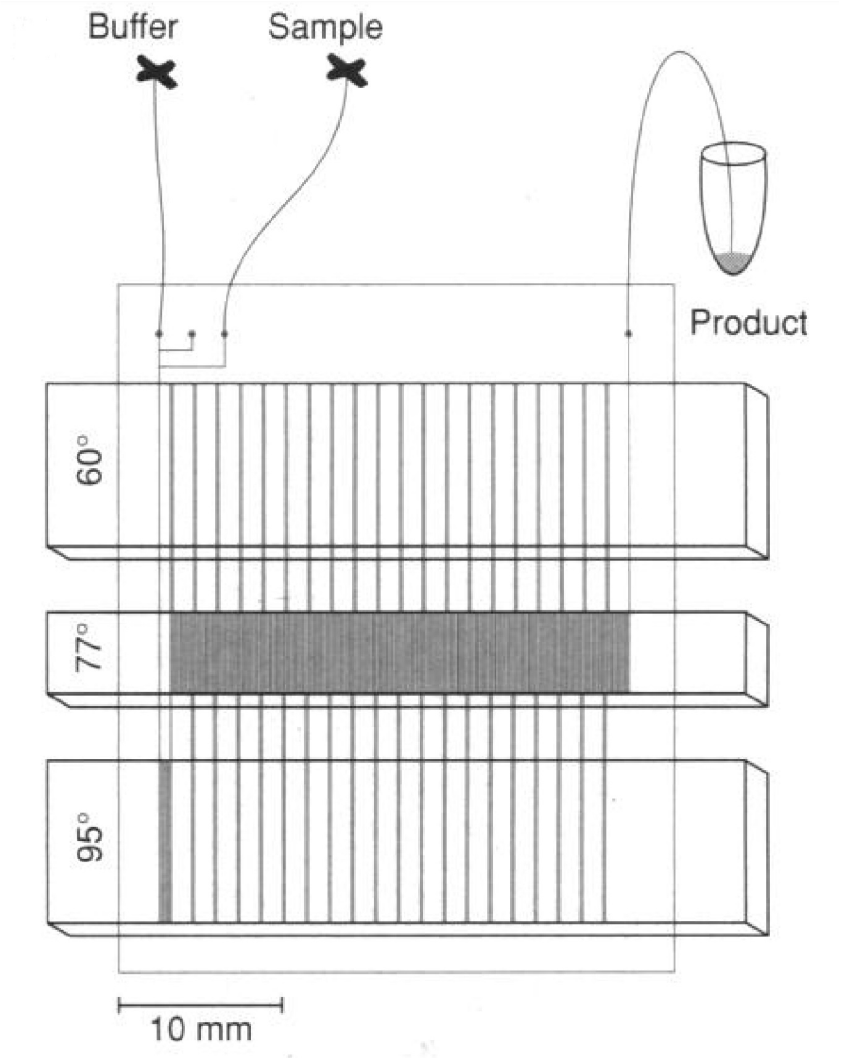

Figure 4.4: A graphic depiction of the serpentine microfluidic device used by Kopp et al. (1998) to achieve a successful PCR amplification in 20 cycles within a minimum of 90 seconds. From Kopp, M. U., De Mello, A. J., & Manz, A. (1998). Chemical Amplification: Continuous-Flow PCR on a Chip. Science, 280(5366), 1046–1048. Reprinted with permission from AAAS.

There are, however, some issues with this design, the main one being its complexity and difficulty of production. This is exacerbated by the fact that such devices are single use, as it would be impossible to clean out such small channels that are microns in scale well enough to guarantee no cross contamination. Another strategy undertaken in recent years is using photonics. The setup tested by Son et al. (2015) and shown in figure 4.5 achieved 30 cycles within 5 minutes, with a maximum heating rate of about 13 K/s and maximum cooling rate of about 6.6 K/s.

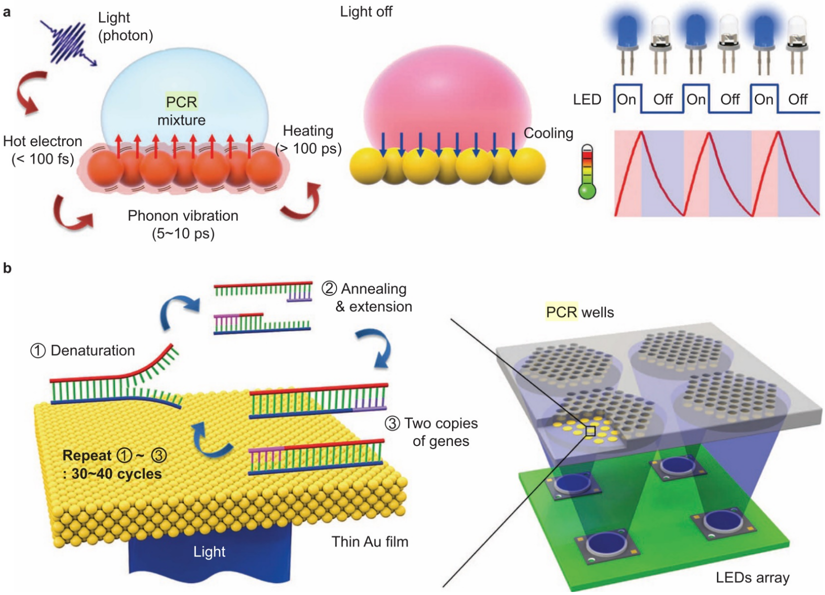
a
Light
(photon)
PCR
mixture
Hot electron
(< 100 fs)
Heating
(> 100 ps)
Phonon vibration
(5~10 ps)
Light off
Cooling
LED
On
Off
On
Off
On
Off
b
① Denaturation
② Annealing
& extension
③ Two copies
of genes
Repeat ① ~ ③
: 30~40 cycles
Light
Thin Au film
PCR wells
LEDs array

Figure 4.5: A diagram showing a photonic PCR setup from the work of Son et al. (2015). Light, emitted by LEDs, thermally excited a gold layer in contact with the PCR mixture. This is then allowed to passively cool to cycle between denaturation, annealing and extension temperatures. Reprinted under the terms of the Creative Commons CC BY license.

The device presented in the literature most similar to the device proposed and tested in this chapter is from the work of Zhang et al. (2022b). The design is shown in figure 4.6 which achieved successful amplification of a 978 bp amplicon within 45 minutes.

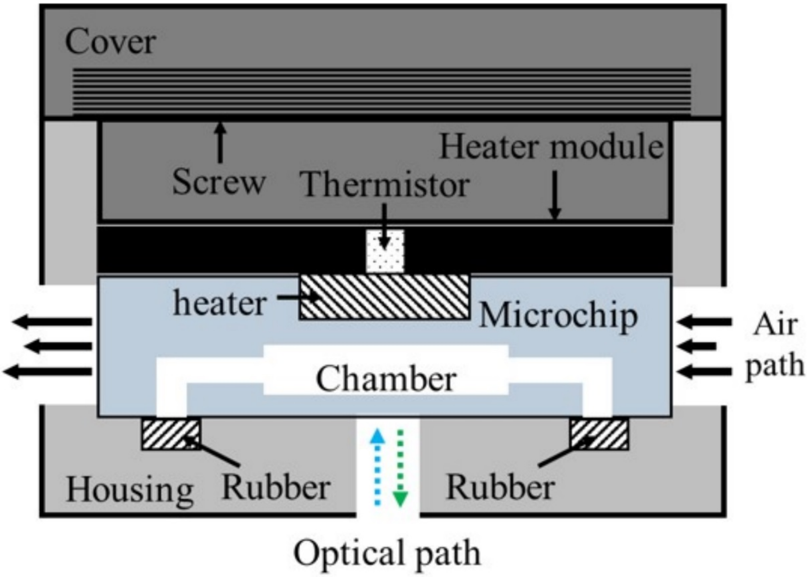

Figure 4.6: An ultrafast PCR device proposed and tested by Zhang et al. (2022b) utilizing a glass chip micromachined using Selective Laster-induced Etching (SLE) using a femtosecond laser to create a chamber that was heated using a chip resistor. A blower fan provided an active cooling source and a thermistor was used to regulate monitor and regulate the temperature. Reprinted under the terms of the Creative Commons CC BY license.

Although Peltier elements are often used to actively cool PCR solutions, there are thermodynamic advantages of maximizing surface area that their designs don't realize. The potential of passive cooling under such conditions was demonstrated quite well with the photonic device of Son et al. (2015). In the following section, a redesign of the heating coil of chapter 2 that attempts to combine the active cooling performance of Son et al's device with a more simplified version of the resistive heating strategy undertaken by Zhang et al. (2022b). While the performance of microfluidics will not likely be exceeded by such a strategy, its simplicity and potential reusability (as explained later) may make it superior in most applications.

4.3 Design

The heating coil design of chapter 2 was expanded in order to maximize the surface area to volume ratio of the overlying liquid assay. A CAD drawing of this is shown in figure 4.7. To hold the liquid in place and spread it out evenly over the heating spiral, a thermoplastic cap was stereolithographically 3D printed using a Photon printer from Anycubic (Shenzhen, China). Figure 4.8 shows the 3D model used for this. This cap was adhered to the glass substrate using an epoxy resin after the thin film coil and protective layers were deposited.

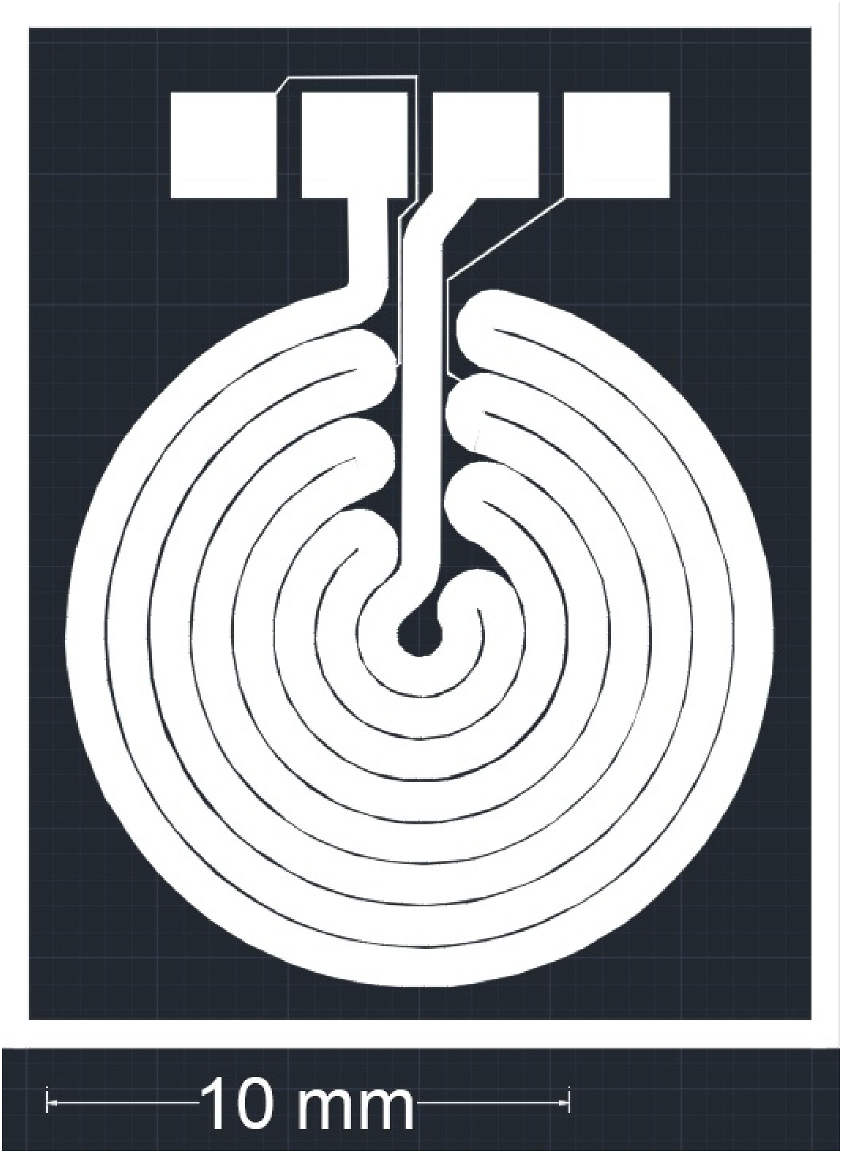

Figure 4.7: A CAD drawing of the PCR chip that was redesigned from the heating spiral discussed in chapter 2.

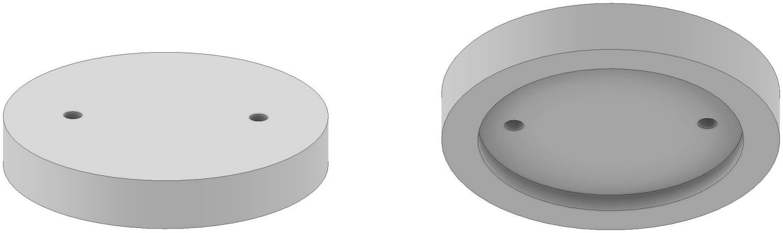

(a) Above **(b)** Below

Figure 4.8: CAD model of the thermoplastic caps applied to the heating coil shown in figure 4.7

The heating coils were structured and deposited in the same manner as the gold calibration chips in chapter 2, only now using a photomask with the structure shown in figure 4.7. To protect the thin film from the solutions it was to come in contact with, a SiN film was initially used, inspired by the initial work of Zhang et al. (2018). This was deposited via a Chemical Vapor Deposition (CVD) method using a PECVD 310 from Surface Technology Systems (Newport, UK). The precursor gases used in this process were nitrogen (N_2) at a flow rate of 1960 standard cubic centimeters per minute (sccm), silane (SiH_4) at 40 sccm, and ammonia (NH_3) at 55 sccm. The chamber pressure was maintained at 900 mTorr throughout the deposition process. The substrate plate was heated to a temperature of 110°C. An RF power of 30 Watts, at a frequency of 13.56 MHz, was supplied as forward power to sustain the plasma. The total process time was 21 minutes, for a targeted thickness of 300 nm.

Initial cycling tests using deionized water showed delamination of the thin film, so 3 different additional films were tested to attempt to alleviate this. These were deposited on top of the initial SiN layer, as this was deposited on all samples, and included Teflon, SiC, and another layer of SiN but deposited at low frequency to balance out the residual tensile stress of the initial layer.

The deposition of Teflon (polytetrafluoroethylene, PTFE) was conducted using an Inductively Coupled Plasma (ICP) reactor. The ICP coil received an RF power input of 800 W, while a lower RF power of 5 W was applied to the substrate plate.

The precursor gas, octafluorocyclobutane (C_4F_8), was utilized at a flow rate of 85 sccm. The process pressure was set at 17 mTorr, and the deposition rate was set to 100 nm/min. With a target film thickness of 100 nm, the deposition time was 1 minute.

Silicon carbide (SiC) was deposited using a CVD process. The substrate plate was set at a temperature of 100°C, and the chamber pressure was maintained at 650 mTorr. The precursor gases were argon (Ar) at a flow rate of 426 sccm with a tolerance of ±5%, silane (SiH_4) at 15 sccm with a variation of ±20%, and methane (CH_4) at 200 sccm with an allowed fluctuation of ±5%. The RF power applied was 60 W at a frequency of 187 kHz to sustain the plasma. The entire deposition process was carried out over a duration of 10 minutes which achieved a final film thickness of about 100 nm, as measured by a reflectometer.

For the final set of chips, another layer of SiN was deposited using the same parameters as before, except with a plate temperature of 110°C, a lower chamber pressure of 550 mTorr, and a lower frequency of 187 kHz. This was carried out over a duration of 17 minutes 30 seconds, giving a final thickness of 350-400 nm as measured with a reflectometer.

All chips continued to show delamination after cycling tests using deionized water, but since the samples with an additional layer of Teflon showed the best results, these were used for the PCR tests in the following section.

4.4 Results

For the following tests the "Mango Mix" assay from Bio Cat (Heidelberg, Germany) was used, consisting of MangoTaq^{TM} DNA Polymerase, $MgCl_2$ to act as a buffer, and ultra-pure dNTPs manufactured by Bioline (now Meridian Bioscience (Cincinnati, USA)). $50\,\mu L$ of this was mixed with $5\,\mu L$ each of the forward and backward primer with concentrations of $10\,\mu mol$, $10\,\mu L$ of the template DNA with a concentration of $1\,ng\,\mu L^{-1}$, and $30\,\mu L$ of deionized water. Template RNA came from *Escherichia coli* with primers for the 16S gene with 27 bp (base pairs) in the forward direction and 1492 in the reverse direction, giving a targeted fragment length of 1465 bp.

Identical solutions were prepared for the PCR chip and a C1000 Touch thermal cycler from Bio-Rad Laboratories, Inc. (Hercules, USA) to act as a control. Cycling parameters for the control included a denaturing step at 95°C for 90 seconds, an annealing step at 55°C for 30 seconds, and an extension step at 72°C for 45 seconds, with a total of 25 cycles. An initial hold time of 3 minutes at 95°C was included to start the reaction, and a finishing hold time of 5 minutes at 72°C to finish it.

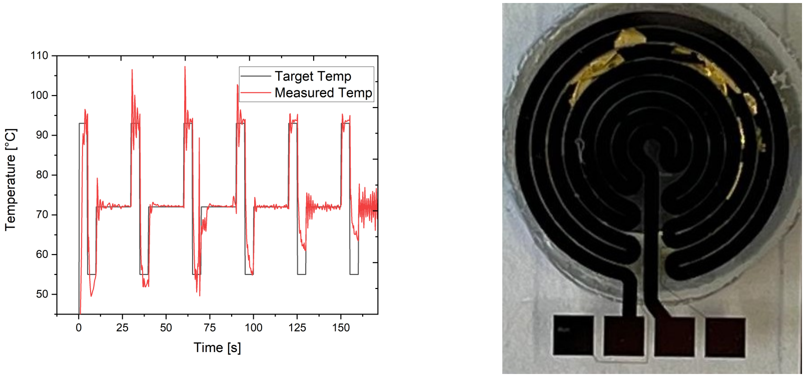

(a)

(b)

Figure 4.9: On the left are data showing the desired temperature pulse and measured pulse over 6 cycles. To the right is an image of the underside of the heating coil with a teflon protective film after this cyclic pulsing was applied.

Shorter cycling times were used for the PCR chip to test its speed and avoid delamination of the thin film which was a known issue. Here, a 5 second denaturing step at 93°C was used, followed by a 5 second annealing step at 55°C, and a 20 second extension step at 72°C. The desired and measured temperature for the first 6 cycles are shown in figure 4.9a, showing a gradual deterioration in control. As shown in the final state of the heating coil in subfigure b, this was the result of the gold thin film delaminating from the glass substrate, which increased the resistance resulting in a measured temperature higher than the actual value. However, the first cycle still showed a good degree of performance and control, achieving a cooling rate of 30 K/s between the denaturing and annealing step.

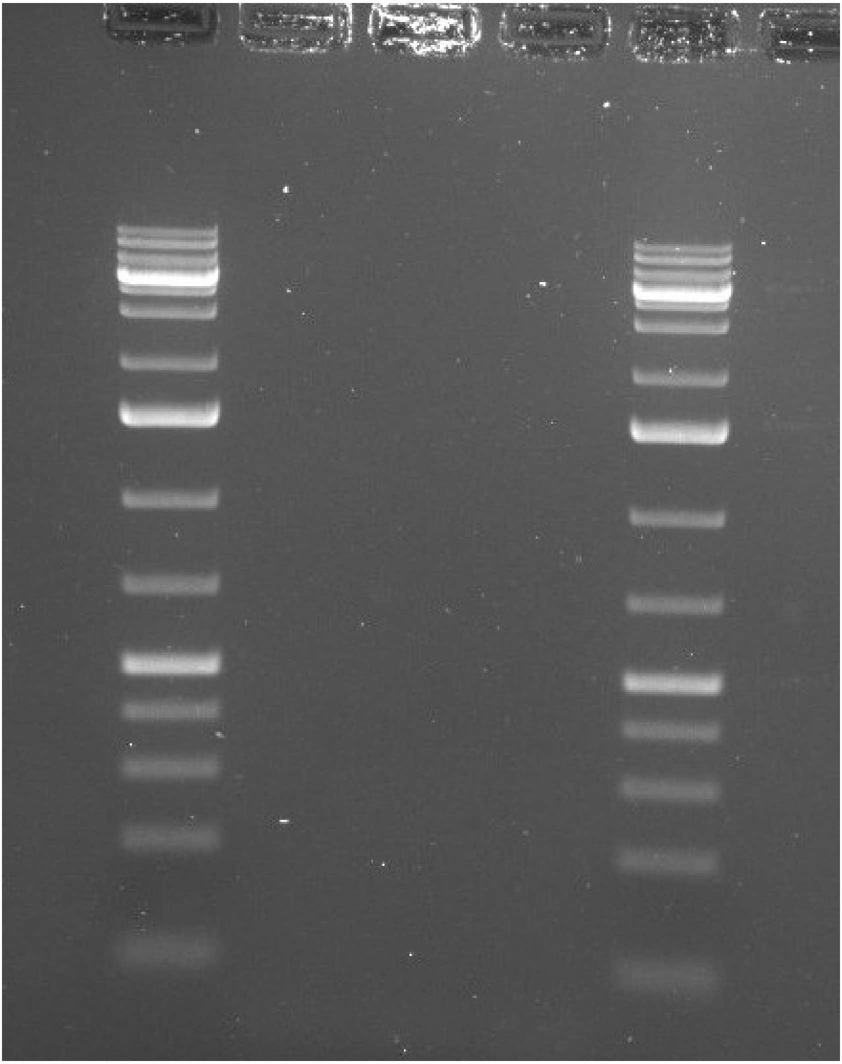

Figure 4.10: Agarose gel electrophoresis results of the solution thermocycled using the cycling pulse shown in figure 4.9 showing no PCR amplification. The wells on the left and right contained control solutions cycled using a C1000 Touch thermal cycler.

Each solution was tested using agarose gel electrophoresis, the results of which are shown in figure 4.10. The first and fifth wells are the control, while the second through fourth contained the solutions amplified by the PCR chip, each showing a negative result.

4.5 Conclusions

While this initial test was unsuccessful, the first cycle shown in figure 4.9a shows its thermodynamic capability. If the thermodynamically active volume is kept as thin as possible, its thermal gradients should be maintained to such a degree that its passive cooling would surpass the performance of any actively cooled device. This is very similar to the strategy of using microfluidics, only in an architecture that is quicker and cheaper to manufacture, and potentially reusable if a sufficient cleaning step is undertaken. To facilitate this cleaning, the thermoplastic cap could be eliminated entirely and replaced with a droplet of mineral oil that would cover the PCR solution to prevent evaporation. This would also require the patterning of hydrophilic surfaces over the heating coil, surrounded by hydrophobic areas, in order to position the solutions more easily and ensure a good thermal contact. Removing the thermoplastic cap also makes it possible to use qPCR since the solution is directly visible, which would significantly shorten diagnostic time as agarose gel electrophoresis can take from 30 minutes to an hour to complete.

The main challenge remaining then is the durability of the protective layer to prevent the diffusion of the overlying solution into the high stress interface between the gold thin film and the glass substrate, which is theorized to cause its delamination. A significant drop in film adhesion in the presence of moisture has also been noticed by other researchers such as Waters and Volinsky (2007). Some useful knowledge could be gleaned from the solar cell industry, where sensitive electronics must be protected from continuous cycling between hot and cold conditions in sometimes wet environments within temperature regimes somewhat similar to those demanded in this application. A recent paper by Kirmani et al. (2023) investigating protective layers for solar cells in space found that a $1\,\mu m$ thick layer of SiO_2 helped "$Cs_{0.05}(MA_{0.17}FA_{0.83})_{0.95}Pb(I_{0.83}Br_{0.17})_3$ (MA, methylammonium; FA, formamidinium cation) and $CsPbI_2Br$ cells survive submergence in water and N,N-dimethylformamide. Furthermore, moisture tolerance of Sn$-$Pb and $CsPbI_2Br$ devices is boosted". This is a good candidate material and thickness, but it may be also useful to investigate more closely where and how failure of the protective layer took place via for instance SEM.

5 Summary

5.1 Summary and Outlook

A relatively short summary and outlook of this dissertation is presented here, as the work contained in chapters 2 through 4 slightly vary in context and so have much more extensive writings in their respective conclusions and outlooks on their potential future developments and applications. These three chapters focused around initial experiments attempting to controllably induce and precisely quantify morphological changes due to interdiffusion effects in heterogeneous materials via temperature control. Chapter 2 presents the lead up to developing the final experimental setup used, showing the difficulty of using indirect heating of the substrate to achieve the heating and cooling rates necessary to controllably induce and halt diffusion processes. Passing a current through a thin film to thermally pulse samples deposited on them has been commonly used and reported on in the literature. The difficulty in determining the temperature of a conductive sample that is itself used as the heating element was partially solved by the work of Zhang et al. (2018). A novel modification of the pulsing method first published by Short et al. (2023) and written about more extensively in chapter 2 allowed this relatively simple device to use rapid thermal pulses. The rates presented here reached up to 200 K/s, but maxing out the current with the PXIe-4139 source reached a maximum of around 25,000 K/s, albeit non-linear.

An unexpected benefit of this technique that was noticed was increased sensitivity to subtle morphological changes that were not noticed with nanocalorimetry. Thermally pulsing Ni/Al thin film multilayers has been extensively reported on in the literature with regards to the intermetallic phases formed, but no mention has been made of the initial diffusing of Ni through Al grain boundaries that was measured here by a small spike in resistance before a major spike indicating complete mixing of the distinct layers. This presents an accessible method to study grain boundary diffusion and aid attempts to better quantify it, promote it to generate novel structures such as brick and mortar architectures, or hinder it to prevent unwanted effects such as corrosion or a breakdown of microelectronic devices. A more precise case study was also proposed on solid state batteries, where grain boundary diffusion is an important phenomenon. Since the scale of these phenomena is so small, cumbersome techniques such as TEM are usually necessary to prove their effects. The experimental setup presented here would allow a much higher throughput to investigate more materials under a more diverse set of circumstances, reducing budgetary and time constraints.

Since grain boundary diffusion played such an important role in the investigations of chapter 2, the next chapter further developed the theoretical understanding of this field. Fast diffusing pathways such as grain boundaries experience leakage to the surrounding grain so it is not straightforward to calculate the diffusion coefficients of diffusants passing through them. Fisher (1951) presented the first mathematical model to account for this, and the work first published by Short and Woll (2021) and written about more extensively in chapter 3 extended this model to include concentration dependent grain boundary diffusion coefficients. A thorough mathematical derivation was first presented to demonstrate its validity, followed by a series of finite difference simulations that demonstrated its significance given degrees of concentration dependence reported on in the literature. While it would be difficult to apply this theoretical framework to precisely determine the concentration dependence of Ni diffusion into Al grains due to inevitable phase changes leading to discontinuous concentration dependence, another binary alloy such as Ag/Au could be used instead as a test case due to its constant elementary unit structure at any stoichiometric ratio. While still not straightforward due to the mathematical difficulties of determining a best fit of diffusion coefficients with respect to temperature, there are some theoretical tools such as those of Vignes and Birchenall (1968) that would mitigate this problem.

Due to the far reaching effects of the global COVID-19 pandemic into our personal and professional lives, much thought was put into potential applications of this work over the course of this doctoral project to better address the inevitable recurrence of such an event. Rapidly heating and quenching samples was integral to this work, but it is also a primary challenge of PCR applied to human diagnostics since it inherently involves numerous thermal cycles. Improving cycling time would significantly reduce its cost and open up new usage scenarios to improve not only population testing but also individual patient care. A thermodynamic strategy similar to that of microfluidic PCR devices was devised by maximizing the surface area to volume ratio of the PCR assay and taking advantage of passive cooling which was demonstrated in previous experiments to reach remarkable cooling rates if the thermodynamically active region is very thin. This was done by expanding the heating coil presented in chapter 2, and covering it with a 3D printed thermoplastic cap into which the PCR solution was injected. While the device proved unstable due to the failure of a protective layer of SiN, SiC, or Teflon over the top of the thin film coil to prevent its delamination, impressive thermodynamic performance while in thermal contact with the liquid solution was briefly achieved. This would shift the limiting factor on speed to the length of the DNA fragment selected by the primers and the speed of the polymerase enzyme. It would be worthwile then, to investigate better strategies to prevent delamination of the thin film in contact with liquids which is a known problem in the literature (Waters and Volinsky 2007) with some potential solutions already reported (Kirmani et al. 2023).

A Appendix

A.1 Matlab Finite Difference Simulation

The finite difference simulation programmed in Matlab used in chapter 3 is displayed below. It runs as follows:

1. Constants and parameters are defined, such as the simulation dimensions, temperature, material properties, and diffusion coefficients.
2. The domain is divided into a grid, and initial concentrations B and diffusion coefficients D are set.
3. For each time step, the program calculates the diffusion coefficients for each grid point, sets up a tridiagonal matrix A (with extra diagonal components representing concentration dependence) to represent the diffusion equation, solves the linear system, and updates the concentrations.
4. The program repeats the process for a specified number of frames.
5. The resulting concentration data is written to a text file, and a surface plot of the final concentration distribution is generated.
6. The program calculates the isoconcentration lines for 10% and 50% of the maximum concentration.
7. A function, CalculateDiffusionCoefficients, is defined to calculate the diffusion coefficients based on the specified model (positive or negative slope).

```
clear
```

```
SimWidth = 2*10^(-9);  % m
SimHeight = 1000*10^(-9);
NiHeight = SimHeight*0.15;
GBWidth = 5*10^(-10);
MeshNumberX = 50;
MeshNumberY = 50;
UnitCellX = SimWidth/MeshNumberX;
UnitCellY = SimHeight/MeshNumberY;

Temp = 250 + 273.15;  % K

AlDNaught = 0.0000037;  % cm^2/s
AlQ = 15700;  % J/mol
NiDNaught = 0.000019;
NiQ = 2.77;

GrainBoundaryOrderMagnitude = 5;
InitialAlDiffusion = 10^(-21);
SurfaceDiffusion = 10^(-15);
ConstantSource = true;
Flow = 2*10^(10);  % 1/(m*s)

AlDensity = 8.9*10^6;  % g/m^3
AlGramsPerMol = 26.981538;
AlNumberDensity = 0;  % mol/cm^2
NiDensity = 2.7 * 10^6;  % g/m^3
NiGramsPerMol = 58.6934;
NiNumberDensity = 1;  % mol/cm^2

Concentrations = zeros(MeshNumberY, MeshNumberX);
Diffusions = zeros(MeshNumberY, MeshNumberX);
```

```
Species = zeros(MeshNumberY, MeshNumberX);  %1 for
    Al, 2 for Ni, 3 for GB

TIME_STEP = 0.01;
FRAMES = 3000;

InputMatrix = {TIME_STEP,FRAMES,"Modified",'P',
    10};
Diffusions(:,:) = InitialAlDiffusion;

#initialize tridiagonal matrix
A = zeros(MeshNumberX*MeshNumberY,MeshNumberX*
    MeshNumberY);
#initialize concentrations in a 1 dimensional list
    to facilitate linear multiplication
B = zeros(MeshNumberX*MeshNumberY,1);

h = waitbar(0,'Please wait...');

#Start simulation for each set of input parameters
    in the input matrix
for i = 1:length(InputMatrix(:,1))
    tstep = InputMatrix{i,1};
    tmax = InputMatrix{i,2}*tstep;
    Model = InputMatrix{i,3};
    Slope = InputMatrix{i,4};
    MaxDiffusion = 10^(-16.5 + InputMatrix{i,5} /
        20);
    MinDiffusion = 10^(-16.5 - InputMatrix{i,5} /
        20);

    % initialize concentrations, species, indices
    Concentrations(:,:) = 0;
```

```
for y = 1:MeshNumberY
    Concentrations(y,:) = (NiNumberDensity)*(1+
       erf((-y)/(1*sqrt(2))));
end

#begin simulation
for t = 0:tstep:tmax
    Diffusions(:,MeshNumberX) =
       CalculateDiffusionCoefficients(
       Concentrations(:,MeshNumberX)./
       NiNumberDensity, MinDiffusion,
       MaxDiffusion, Slope);
    Diffusions(1,:) = SurfaceDiffusion;
    D = reshape(Diffusions,MeshNumberX*
       MeshNumberY,1);

    index = 0;
    for y = 1:MeshNumberX*MeshNumberY
        yback = y-1;
        yfor = y+1;
        if y == index*MeshNumberY+1
            yback = index*MeshNumberY+
               MeshNumberY;
        elseif y == index*MeshNumberY+
           MeshNumberY
            yfor = index*MeshNumberY+1;
            index = index + 1;
        end
        if y-MeshNumberY <= 0
            xback = MeshNumberX*MeshNumberY + y
               -MeshNumberY;
        else
            xback = y-MeshNumberY;
```

```
end
if y+MeshNumberY > MeshNumberX*
   MeshNumberY
    xfor = y+MeshNumberY - MeshNumberX*
       MeshNumberY;
else
    xfor = y+MeshNumberY;
end
if y <= MeshNumberX*MeshNumberY -
   MeshNumberY       #within Grain
    A(y,y) = 1 + (2*tstep*D(y,1))/(
       UnitCellX^2) + (2*tstep*D(y,1))
       /(UnitCellY^2);
    A(y,xback) = -(tstep*D(y,1))/(
       UnitCellX^2);
    A(y,xfor) = -(tstep*D(y,1))/(
       UnitCellX^2);
    A(y,yback) = -(tstep*D(y,1))/(
       UnitCellY^2);
    A(y,yfor) = -(tstep*D(y,1))/(
       UnitCellY^2);
elseif Model == 'Fisher'    #for Fisher
    model
    A(y,y) = 1 + (2*tstep*
       InitialAlDiffusion)/(GBWidth*
       UnitCellX) + (2*tstep*D(y,1))/(
       UnitCellY^2);
    A(y,xfor) = -(2*tstep*
       InitialAlDiffusion)/(GBWidth*
       UnitCellX);
    A(y,yback) = -(tstep*D(y,1))/(
       UnitCellY^2);
```

```
        A(y,yfor) = -(tstep*D(y,1))/(
           UnitCellY^2);
    elseif Model == 'Modified'  #for
       modified model
        if y == MeshNumberX*MeshNumberY -
           MeshNumberY + 1
            DeltaDiffusion = 0;
        elseif y == MeshNumberX*MeshNumberY
            DeltaDiffusion = 0;
        else
            DeltaDiffusion = (D(y+1,1) - D(
               y,1)) / UnitCellY;
        end
        A(y,y) = 1 + (DeltaDiffusion*tstep)
           /(UnitCellY) + (2*tstep*D(y,1))
           /(UnitCellY^2) + (2*tstep*
           InitialAlDiffusion)/(GBWidth*
           UnitCellX);
        A(y,xfor) = -(2*tstep*
           InitialAlDiffusion)/(GBWidth*
           UnitCellX);
        A(y,yback) = -(tstep*D(y,1))/(
           UnitCellY^2);
        A(y,yfor) = -(DeltaDiffusion*tstep)
           /(UnitCellY) - (tstep*D(y,1))/(
           UnitCellY^2);
    end
end

B = reshape(Concentrations, MeshNumberX*
   MeshNumberY,1);
X = double(mldivide(A,B));
```

```
        Concentrations = reshape(X,MeshNumberY,
           MeshNumberX);
        if ConstantSource
            Concentrations(1,:) = Concentrations
               (1,:) + Flow*(UnitCellX*tstep);
        end
        waitbar(((i-1)*FRAMES + t/tstep)/(length(
           InputMatrix(:,1))*FRAMES),h)
    end

    writematrix(Concentrations, 'concentrations_' +
        string(tstep) + '_' + string(tmax) + '_' +
        Model + '_' + Slope + '_' + string(
       MeshNumberX) + '_' + string(MeshNumberY) +
       '_' + string(GrainBoundaryOrderMagnitude) +
        '_0p' + string(InputMatrix{i,5}) + '.txt',
        'Delimiter', ';');

end

#plot concentration surface plot
surf(Concentrations);

TenpIsoconcentration = zeros(MeshNumberX,2);
TenpIsoconcentration(:,1) = 1:MeshNumberX;
FiftypIsoconcentration = zeros(MeshNumberX,2);
FiftypIsoconcentration(:,1) = 1:MeshNumberX;

#Calculate isoconcentration lines for 10% Ni
for x = 1:MeshNumberX
    for y = int16(MeshNumberY/2):MeshNumberY
        if Concentrations(y,x) > 0.1
```

```
            TenpIsoconcentration(x,2) = MeshNumberY
               -y;
            break
        end
    end
end

#Calculate isoconcentration lines for 50% Ni
for x = 1:MeshNumberX
    for y = int16(MeshNumberY/2):MeshNumberY
        if Concentrations(y,x) > 0.5
            FiftypIsoconcentration(x,2) =
               MeshNumberY-y;
            break
        end
    end
end

function DiffusionCoefficients =
   CalculateDiffusionCoefficients(Concentrations,
   MinDiffusion, MaxDiffusion, Slope)
n = length(Concentrations);
DiffusionCoefficients = zeros(n,1);
if Slope == 'P'
    DiffusionCoefficients(1:n) = 10.^(
       Concentrations.*log10(MaxDiffusion/
       MinDiffusion) + log10(MinDiffusion));
elseif Slope == 'N'
    DiffusionCoefficients(1:n) = 10.^(
       Concentrations.*log10(MinDiffusion/
       MaxDiffusion) + log10(MaxDiffusion));
else
```

```
      DiffusionCoefficients(:) = 10^((log10(
           MinDiffusion) + log10(MaxDiffusion)) / 2);
end
end
```

List of Figures

2.1 An image of the cylindrical oven used to heat bulk samples in a vacuum. The heating element was wrapped between two steel cylinders which were held up with two ceramic rods. Two thermoelectric probes measured the temperature on the inside and outside surface of the cylinder. 10
2.2 Temperature and associated heating rate of a silicon chip pulsed within the cylindrical heater shown in figure 2.1. The temperature was measured with a thermocouple that was bent upwards so as to contact the sample. After 100°C was achieved, the current through the heating element was cut off, and the system was allowed to passively cool. 11
2.3 Multilayer Ni/Al sample heated to 250°C for 60 minutes in a TOF.SIMS 5. TEM lamellae were cut using a Zeiss Crossbeam 550 L FIB with the method shown in section 2.2. The STEM images shown here were obtained using a Tecnai F20 from FEI (Hillsboro, USA) with a beam voltage of 200 kV. 12
2.4 XPS data from sputtering the Ni/Al sample shown in figure 2.3 in a TOF.SIMS 5 using an Ar source with a current of $10\,\mu\mathrm{A}$, accelerated to an energy of $3\,\mathrm{keV}$. The relative concentration of Ni and Al is taken from the relative activity of their 2p and 2s peaks, respectively. Time refers to the sputtering time. 13
2.5 Outline of the thin film heater coil used to create a photomask. A current is passed through the two innermost square contact pads which then concentrates through the heating coil below. The two outermost contact pads then allow a measurement of the voltage drop across the third outermost ring in the coil giving its resistance. . 15

2.6 An array of the heater coil design shown in figure 2.5 arranged so as to fit on a 4 inch wafer. This was the pattern used for the photomask for the photolithographic process described in figure 2.7. . 17
2.7 Graphical representation of a negative photolithographic process. The steps are as follows: (1) A photoresist is spin coated onto the substrate. (2) The photoresist is illuminated with UV light through a photomask with the desired design. (3) A developer washes away any photoresist not illuminated with UV light. (4) A thin film is deposited (in this case gold). (5) An acetone wash removes the remaining photoresist along with any thin film deposited on top of it, leaving the final patterned thin film. 18
2.8 A TEM image of an as deposited sample showing the results of the sputtering process for a sample of type 2. On the left is the glass substrate which is separated from the first Al layer by a thin layer of Ti, used to promote adhesion. The Ni layers are the darkest layers. This cross section was extracted using the method described in section 2.2 and imaged using a Tecnai F20. . . . 20
2.9 An image of the setup used to characterize the temperature versus resistance relationship of the gold calibration chips. The copper heating block was incrementally stepped up in temperature, measured with a thermocouple underneath the chip. A 4 contact point measurement with tungsten needles using a 20 mA current was used to measure the resistance across the third outermost ring in the heating coil shown in figure 2.5. 21
2.10 Resistance versus temperature relationship for 5 different gold calibration samples using a 4 contact measurement at 20 mA with the setup shown in figure 2.9. 23

2.11 A circuit diagram describing the measurement setup. A_1 through A_3 refer to the analog voltmeters on the PXIe-4464 while current, I_1, was sourced from the SMU. On the right in the diagram are the four contact pads of the chip shown in figure 2.5 with the labels V^+, V^-, I^+, and I^- indicating the voltage and current pads, respectively. Current from the source I_1 flowed through the 1 Ω shunt resistor R_1 followed by the current pads leading to the heating coil. The voltage across R_1 was measured by A_3 for an accurate current measurement. A_1 and A_2 both measured the voltage across the voltage contact pads. 24
2.12 Data showing two power pulses. The first was applied to a gold calibration sample that was PID regulated to match a 100 K/s linear ramp to 700°C. The same power pulse was then applied to another calibration sample and the resulting temperature data were plotted over the former, showing very good agreement. Reprinted from Short et al. (2023). 25
2.13 Data resulting from the 100 K/s power pulse shown in figure 2.12 applied two Ni/Al samples of type 2 in table 2.1 (200 nm Al). The top image shows the resistance over temperature, and below it is the plot of its derivative with respect to temperature. Two distinct peaks are indicated. Reprinted from Short et al. (2023) . 26
2.14 Data showing resistance over temperature of three different samples of type 2 in table 2.1 that were pulsed using the power pulse shown in figure 2.12 and quenched at points of interest around the two peaks shown in figure 2.13. 27
2.15 STEM-in-SEM images of cross sectional TEM lamella taken from Ni/Al samples of type 2 that were untreated (a) and pulsed using the power pulse shown in figure 2.12 to before the first peak (b), after the first peak (c), and after the second peak (d) as shown in figure 2.14. Ni is darker while the lighter areas show Al, as shown in subfigure (a). Reprinted from Short et al. (2023) . . . 28
2.16 EDX scans of the STEM images shown in figure 2.15 before and after peak 1 showing counts of photons from the Ka1 edge for Al and Ni. 29

2.17 On the left is a STEM image of a Ni/Al sample of type 2 that was quenched before the first peak. EDX linescans were taken along the lines indicated in the image. The measured Ni distribution is plotted on the right. Reprinted from Short et al. (2023) 30
2.18 On the left is a STEM image of a Ni/Al sample of type 2 that was quenched after the first peak. EDX linescans were taken along the lines indicated in the image. The measured Ni distribution is plotted on the right. Reprinted from Short et al. (2023) 30
2.19 Data showing how peak 1 is modified by differing Al layer thicknesses, given the same linear 100 K/s pulse. Reprinted from Short et al. (2023) 31
2.20 Kissinger plots showing the shift in peak 1 (a) and 2 (b) resulting from different linear heating ramps varying from 25 to 200 K/s applied to the Ni/Al samples. The different Al thicknesses for samples 1, 2, and 3 are indicated. Reprinted from Short et al. (2023) . 33
2.21 Elastic moduli and hardness data from nanoindentations taken with an Agilent G200 Nanoindenter (Agilent Technologies) on the third outermost ring of sample 2 (where temperature was measured) pulsed to various maximum temperatures shown along the x-axis. The upper and lower bound for ± 1 standard deviation are shown as accompanying thinner solid or dashed lines for the hardness and elasticity moduli data, respectively. 34
2.22 Images displaying different stress states of the Ni surface from a sample of type 2 pulsed at 100 K/s to failure (circuit break) occurring at around 700°C. Image (a) is from an optical microscope showing cracks in the third outermost ring induced by nanoindentation while image (b) shows an SEM image of one of the inner rings showing mudcracks. 35

2.23 Resistance data from sample 2 pulsed at 100 K/s compared with expected resistance of the coil assuming no diffusion effects or structural or morphological transformations based on the resistivity of Ni and Al with respect to temperature. To match the initial measured resistance of the coil, this line was shifted up to better compare with the data. The difference in resistance between the actual sample and this line is shown as $1.4\,\Omega$. (Short et al. 2023) 36
2.24 Diagram of the morphological situation of a single bilayer of sample 2 proposed to be present after peak 1, with NiAl regions formed within the grain boundaries of the Al layer. Reprinted from Short et al. (2023) 37
2.25 A reinterpretation of the situation depicted in figure 2.24 as a circuit with the Ni and Al films in parallel. The Al, NiAl grain sequence along the top layer is repeated along the length of the coil. Reprinted from Short et al. (2023) 38
2.26 Diagram showing Li dendritic growth through a solid electrolyte. Reprinted with permission from G. V. Alexander, M. S. Indu, and R. Murugan, Review on the critical issues for the realization of all-solid-state lithium metal batteries with garnet electrolyte: interfacial chemistry, dendrite growth, and critical current densities, Ionics, 27, 4105-4126, 2021, Springer Nature. 41
3.1 Graphical representation of the diffusion situation this chapter seeks to analyze. At the bottom is a diffusant source that diffuses upwards through the fast diffusion grain boundary (GB), with width δ, and outwards into the grains to the left and right. This forms diffusant "peaks" indicated by isoconcentration lines with concentrations $c_1 > c_2 > c_3 > c_4$. Reprinted from Short and Woll (2021) 44
3.2 A graphic showing the three main Harrison Regimes described by Harrison (1961), consisting of parallel grain boundaries extending vertically from a diffusant source below with a horizontal spacing of d. The diffusant is shown here in gray. 51

3.3 Raw data resulting from the finite difference simulation described in section 3.2. On the left is a map showing the final solute concentrations across the cells assuming D_{gb} was held constant at $10^{-15}\mathrm{m}^2\,\mathrm{s}^{-1}$. The black lines show isoconcentration curves while the insert shows the 10% isoconcentration curve using the Fisher model and the one derived in this study. On the right are the 10% isoconcentration curves for a negative (left graph) and positive (right graph) dependence of D_{gb} on c_{gb} where $n = 2$, with the axes normalized to standard diffusion lengths. Reprinted from Short and Woll (2021) 55

3.4 Data showing the percent change in penetration depth along the grain boundary given a negative and positive concentration dependency. Subfigure a shows this deviation with respect to the diffusant concentration point where $n = 2$. Subfigure b shows the penetration depth's dependency on n where the diffusant concentration considered was 10%. Reprinted from Short and Woll (2021) 56

3.5 Data showing the result of applying equation 3.23 to our simulation results for a positive dependency using equation 3.16 as a boundary condition for the left side (a), and Fisher's model (b) with n ranging from 0 to 2. The simulation field was widened along the x-direction from $2\,\mathrm{nm}$ to $50\,\mathrm{nm}$ and shortened along the y-direction from $5\,\mathrm{\mu m}$ to $1\,\mathrm{\mu m}$. Linear trendlines were fitted to the data in the dilute region. Reprinted from Short and Woll (2021) 57

3.6 Results of applying Rabkin's solution shown in equation 3.30. Reprinted from Short and Woll (2021) 60

3.7 Data showing the % deviation from the Fisher model given various values of s for a positive (a) and negative (b) concentration dependency. Reprinted from Short and Woll (2021) 61

3.8 Figure showing the data from simulations using different values for s, layer averaged using equation 3.23. To account for the resulting different Harrison regimes, $s = 1$ is plotted over $y^{6/5}$ while $s = 5, 10$ are plotted over y^2. Reprinted from Short and Woll (2021) 61

3.9 Gold-Silver phase diagram showing a single phase at any mixing ratio. Reprinted with permission from H. Okamoto and T.B. Massalski, The Ag-Au (Silver-Gold) system, Bulletin of Alloy Phase Diagrams, 4, 30-38, 1983, Springer Nature. 63
3.10 HRTEM image of a site within the Ni/Al multilayer where Ni has diffused from the bottom of the image into the Al layer above, separated into two grains by the approximately vertical grain boundary just right of center. Diffusion was clearly promoted through the Al grain boundary forming a characteristic peak in the surrounding intermetallic phases. 64
4.1 An image showing the molecular makeup of DNA. Covalent bonds are indicated by solid lines while dotted lines indicate hydrogen bonds. Reprinted under fair use from Pray (2008). 68
4.2 An example of agarose gel electrophoresis showing the result of a PCR test for Groundnut bud necrosis virus in onions (*Allium Cepa*). Well 1 shows a negative result, while 2-4 are positive. Reprinted with permission from A. Sujitha et al, First report of Groundnut bud necrosis virus infecting onion (Allium cepa), Australasian Plant Disease Notes, 7, 183-187, 2012, Springer Nature 70
4.3 qPCR results on mouse DNA using primers targeting the hepcidin 1 gene with concentrations varying from 50-600 nM. Reprinted with permission from T. Nolan, R. E. Hands, and S. A. Bustin, Quantification of mRNA using real-time RT-PCR, Nature Protocols, 1, 1559-1582, 2006, Springer Nature. 71
4.4 A graphic depiction of the serpentine microfluidic device used by Kopp et al. (1998) to achieve a successful PCR amplification in 20 cycles within a minimum of 90 seconds. From Kopp, M. U., De Mello, A. J., & Manz, A. (1998). Chemical Amplification: Continuous-Flow PCR on a Chip. Science, 280(5366), 1046–1048. Reprinted with permission from AAAS. 73

4.5 A diagram showing a photonic PCR setup from the work of Son et al. (2015). Light, emitted by LEDs, thermally excited a gold layer in contact with the PCR mixture. This is then allowed to passively cool to cycle between denaturation, annealing and extension temperatures. Reprinted under the terms of the Creative Commons CC BY license. 74
4.6 An ultrafast PCR device proposed and tested by Zhang et al. (2022b) utilizing a glass chip micromachined using SLE using a femtosecond laser to create a chamber that was heated using a chip resistor. A blower fan provided an active cooling source and a thermistor was used to regulate monitor and regulate the temperature. Reprinted under the terms of the Creative Commons CC BY license. 75
4.7 A CAD drawing of the PCR chip that was redesigned from the heating spiral discussed in chapter 2. 77
4.8 CAD model of the thermoplastic caps applied to the heating coil shown in figure 4.7 78
4.9 On the left are data showing the desired temperature pulse and measured pulse over 6 cycles. To the right is an image of the underside of the heating coil with a teflon protective film after this cyclic pulsing was applied. 80
4.10 Agarose gel electrophoresis results of the solution thermocycled using the cycling pulse shown in figure 4.9 showing no PCR amplification. The wells on the left and right contained control solutions cycled using a C1000 Touch thermal cycler. 82

List of Tables

2.1 List of Ni/Al thin film samples indicating their varying Al film thicknesses. 18

3.1 Calculated and expected values of D_{gb} from applying equation 3.26 to the data shown in Figure 3.5. Expected D_{gb} is derived from Equation 3.27 at the dilute limit ($c_{gb} = 0$) with the given value of n. 58

List of Publications

Journal articles

M. Short and K. Woll. An expansion of the Fisher model for concentration dependent grain boundary diffusion. *Acta Materialia*, 217:117056, sep 2021. ISSN 1359-6454. doi: 10.1016/J.ACTAMAT.2021.117056.

M. Short, F. Bridges, T. Keiber, G. Rogl, and P. Rogl. A comparison of the local structure in ball-milled and hand ground skutterudite samples using EXAFS. *Intermetallics*, 63:80–85, aug 2015. ISSN 09669795. doi: 10.1016/j.intermet.2015.04.001.

M. Short, J. Müller, S. Lee, H. Fornasier, U. Köhler, V. Ott, M. Stüber, B. Gerdes, T. Rupp, C. Kirchlechner, and K. Woll. Heterogeneous microstructures tuned in a high throughput architecture. *Materials & Design*, 229:111834, may 2023. doi: 10.1016/J.MATDES.2023.111834.

Bibliography

A. Abdal-hay, F. A. Sheikh, N. Gómez-Cerezo, A. Alneairi, M. Luqman, H. R. Pant, and S. Ivanovski. A review of protein adsorption and bioactivity characteristics of poly ϵ-caprolactone scaffolds in regenerative medicine. *European Polymer Journal*, 162:110892, Jan 2022. ISSN 0014-3057. doi: 10.1016/J.EURPOLYMJ.2021.110892.

M. R. Achter, L. S. Birks, and E. J. Brooks. Grain-boundary diffusion of zinc in copper measured by the electron-probe microanalyzer. *Journal of Applied Physics*, 30(11):1825–1827, 1959. ISSN 00218979. doi: 10.1063/1.1735063.

G. V. Alexander, M. S. Indu, and R. Murugan. Review on the critical issues for the realization of all-solid-state lithium metal batteries with garnet electrolyte: interfacial chemistry, dendrite growth, and critical current densities. *Ionics 2021 27:10*, 27(10):4105–4126, Aug 2021. ISSN 1862-0760. doi: 10.1007/S11581-021-04190-Y.

L. H. Allen, G. Ramanath, S. L. Lai, Z. Ma, S. Lee, D. D. J. Allman, and K. P. Fuchs. 1 000 000 °C/s thin film electrical heater: In situ resistivity measurements of Al and Ti/Si thin films during ultra rapid thermal annealing. *Applied Physics Letters*, 64(4):417–419, Jan 1994. ISSN 0003-6951. doi: 10.1063/1.111116.

A. E. Austin and N. A. Richard. Grain-Boundary Diffusion. *Journal of Applied Physics*, 32(8):1462–1471, Nov 1961. ISSN 0021-8979. doi: 10.1063/1.1728380.

A. E. Austin and N. A. Richard. Grain-Boundary Diffusion of Gold in Copper. *Journal of Applied Physics*, 33(12):3569–3574, 1962. ISSN 0021-8979. doi: 10.1063/1.1702448.

P. Benoist and G. Martin. Atomic model for grain boundary and surface diffusion. *Thin Solid Films*, 25(1):181–197, Jan 1975. ISSN 00406090. doi: 10.1016/0040-6090(75)90255-2.

J. Bernardini, Ch. Girardeaux, A. Rolland, and D. L. Beke. Effect of grain boundary segregation and migration on diffusion profiles: Analysis and experiments. *Interface Science*, 11(1):33–40, 2003. ISSN 09277056. doi: 10.1023/A:1021574604642.

S. A. Bhakta, E. Evans, T. E. Benavidez, and C. D. Garcia. Protein adsorption onto nanomaterials for the development of biosensors and analytical devices: A review. *Analytica Chimica Acta*, 872:7–25, May 2015. ISSN 0003-2670. doi: 10.1016/J.ACA.2014.10.031.

G. Chen, M. S. Dresselhaus, G. Dresselhaus, J.-P. Fleurial, and T. Caillat. Recent developments in thermoelectric materials. *International Materials Reviews*, 48 (1):45–66, 2003. doi: 10.1179/095066003225010182.

Y. Chen, Y. Fan, S. Lee, G. Hackett, H. Abernathy, K. Gerdes, and X. Song. Interface and grain boundary degradation in LSM-YSZ composite Solid Oxide Fuel Cell cathodes operated in humidified air. *Journal of Power Sources*, 438:227043, Oct 2019. ISSN 0378-7753. doi: 10.1016/J.JPOWSOUR.2019.227043.

S. Divinski, J. Ribbe, G. Schmitz, and C. Herzig. Grain boundary diffusion and segregation of Ni in Cu. *Acta Materialia*, 55(10):3337–3346, 2007. ISSN 1359-6454. doi: https://doi.org/10.1016/j.actamat.2007.01.032.

S. V. Divinski, G. Reglitz, and G. Wilde. Grain boundary self-diffusion in polycrystalline nickel of different purity levels. *Acta Materialia*, 58(2):386–395, 2010. ISSN 13596454. doi: 10.1016/j.actamat.2009.09.015.

M. S. Dresselhaus, G. Chen, M. Y. Tang, R. Yang, H. Lee, D. Wang, Z. Ren, J.-P. Fleurial, and P. Gogna. New Directions for Low-Dimensional Thermoelectric Materials. *Advanced Materials*, 19(8):1043–1053, Apr 2007. ISSN 1521-4095. doi: 10.1002/ADMA.200600527.

Z. Erdélyi and D. L. Beke. Nanoscale volume diffusion: Diffusion in thin films, multilayers and nanoobjects (hollow nanoparticles). *Journal of Materials Science*, 46(20):6465–6483, 2011. ISSN 00222461. doi: 10.1007/s10853-011-5720-4.

Z. Erdelyi, D. Beke, P. Nemes, and G. Langer. On the range of validity of the continuum approach for nonlinear diffusional mixing of multilayers. *Philosophical Magazine A*, 79:1757–1768, Aug 1999. doi: 10.1080/01418619908210390.

J. C. Fisher. Calculation of Diffusion Penetration Curves for Surface and Grain Boundary Diffusion. *Journal of Applied Physics*, 22(1):74–77, 1951. doi: 10.1063/1.1699825.

P. Gas, D. L. Beke, and J. Bernardino. Grain-boundary diffusion: Analysis of the C kinetic regime. *Philosophical Magazine Letters*, 65(3):133–139, Mar 1992. ISSN 0950-0839. doi: 10.1080/09500839208207526.

G. B. Gibbs. Grain Boundary Impurity Diffusion. *physica status solidi (b)*, 16 (1):K27–K29, Jan 1966. ISSN 0370-1972. doi: 10.1002/pssb.19660160143.

M. Glienke, M. Vaidya, K. Gururaj, L. Daum, B. Tas, L. Rogal, K. G. Pradeep, S. V. Divinski, and G. Wilde. Grain boundary diffusion in CoCrFeMnNi high entropy alloy: Kinetic hints towards a phase decomposition. *Acta Materialia*, 195:304–316, 2020. ISSN 1359-6454. doi: https://doi.org/10.1016/j.actamat.2020.05.009.

M. D. Grapes, T. Lagrange, K. Woll, B. W. Reed, G. H. Campbell, D. A. Lavan, and T. P. Weihs. In situ transmission electron microscopy investigation of the interfacial reaction between Ni and Al during rapid heating in a nanocalorimeter. *APL Materials*, 2(11):116102, Nov 2014. ISSN 2166532X. doi: 10.1063/1.4900818.

J. E. Greene. Tracing the 5000-year recorded history of inorganic thin films from ∼3000 BC to the early 1900s AD. *Applied Physics Reviews*, 1(4):041302, 2014. doi: 10.1063/1.4902760.

S. M. Hahn and J. E. Shuren. Coronavirus (COVID-19) Update: FDA Authorizes First Antigen Test to Help in the Rapid Detection of the Virus that Causes COVID-19 in Patients | FDA, May 2020. URL `https://www.fda.gov/news-events/press-announcements/coronavirus-covid-19-update-fda-authorizes-first-antigen-test-help-rapid-detection-virus-causes`.

E. O. Hall. The Deformation and Ageing of Mild Steel: III Discussion of Results. *Proceedings of the Physical Society. Section B*, 64(9):747–753, 1951.

L. G. Harrison. Influence of dislocations on diffusion kinetics in solids with particular reference to the alkali halides. *Transactions of the Faraday Society*, 57(0):1191–1199, 1961. ISSN 0014-7672. doi: 10.1039/TF9615701191.

E. W. Hart. On the role of dislocations in bulk diffusion. *Acta Metallurgica*, 5 (10):597, 1957. ISSN 00016160. doi: 10.1016/0001-6160(57)90127-X.

R. Headrick. Fundamental Mechanisms of Roughening and Smoothing During Thin Film Deposition. Mar 2016. doi: 10.2172/1242492.

C. Herzig and S. V. Divinski. Grain Boundary Diffusion in Metals: Recent Developments. *Materials Transactions*, 44(1):14–27, 2003. doi: 10.2320/matertrans.44.14.

C. Herzig, M. Lohmann, and S. V. Divinski. Tracer Diffusion and Linear and Non-Linear Segregation in Cu Poly and Bicrystals. *Defect and Diffusion Forum*, 216-217:101–112, Jan 2003. doi: 10.4028/www.scientific.net/DDF.216-217.101.

C. Holzapfel, D. C. Rubie, S. Mackwell, and D. J. Frost. Effect of pressure on Fe-Mg interdiffusion in (FexMg1-x)O, ferropericlase. *Physics of the Earth and Planetary Interiors*, 139(1):21–34, 2003. ISSN 0031-9201. doi: https://doi.org/10.1016/S0031-9201(03)00142-0.

R. T. Howe. Polycrystalline Silicon Micromachining: A New Technology for Integrated Sensors. *Annals of Biomedical Engineering*, 14:187–197, 1986.

W. Huber, G. Borionetti, and C. Villani. The Behavior of Polysilicon Thin Film Stress and Structure Under Rapid Thermal Processing Conditions. *Materials Research Society*, 130(1):389–393, 1989. ISSN 0272-9172. doi: 10.1557/PROC-130-389/METRICS.

A. Jose, K. M. Ninave, S. Karnam, and V. V. K. Venuganti. Temperature-sensitive liposomes for co-delivery of tamoxifen and imatinib for synergistic breast cancer treatment. *Journal of liposome research*, 29(2):153–162, Apr 2019. ISSN 1532-2394. doi: 10.1080/08982104.2018.1502315.

B. H. Kang, Y. Lee, E. S. Yu, H. Na, M. Kang, H. J. Huh, and K. H. Jeong. Ultrafast and Real-Time Nanoplasmonic On-Chip Polymerase Chain Reaction for Rapid and Quantitative Molecular Diagnostics. *ACS Nano*, 15(6):10194–10202, Jun 2021. ISSN 1936086X. doi: 10.1021/ACSNANO.1C02154/ASSET/IMAGES/LARGE/NN1C02154_0005.JPEG.

M. J. Kim, H. I. Kim, J. H. Kim, S. M. Suh, and H. Y. Kim. Rapid on-site detection of shrimp allergen tropomyosin using a novel ultrafast PCR system. *Food Science and Biotechnology*, 28(2):591–597, Apr 2019. ISSN 12267708. doi: 10.1007/S10068-018-0479-X/TABLES/3. URL `https://link.springer.com/article/10.1007/s10068-018-0479-x`.

A. R. Kirmani, D. P. Ostrowski, K. T. VanSant, T. A. Byers, R. C. Bramante, K. N. Heinselman, J. Tong, B. Stevens, W. Nemeth, K. Zhu, I. R. Sellers, B. Rout, and J. M. Luther. Metal oxide barrier layers for terrestrial and space perovskite photovoltaics. *Nature Energy 2023 8:2*, 8(2):191–202, Jan 2023. ISSN 2058-7546. doi: 10.1038/s41560-022-01189-1. URL `https://www.nature.com/articles/s41560-022-01189-1`.

H. E Kissinger. Variation of peak temperature with heating rate in differential thermal analysis. *Journal of Research of the National Bureau of Standards*, 57(4):217, 1956. ISSN 0091-0635. doi: 10.6028/jres.057.026.

S. Kondavalasa, S. Sankaran, H. Kumar, H. Rösner, M. Peterlechner, V. Esin, S. V. Divinski, and G. Wilde. Grain boundary diffusion and grain boundary structures of a Ni-Cr-Fe- alloy: Evidences for grain boundary phase transitions. *Acta Materialia*, 195, Jun 2020. doi: 10.1016/j.actamat.2020.05.051.

M. U. Kopp, A. J. De Mello, and A. Manz. Chemical Amplification: Continuous-Flow PCR on a Chip. *Science*, 280(5366):1046–1048, May 1998. ISSN 00368075. doi: 10.1126/SCIENCE.280.5366.1046. URL `https://www.science.org/doi/10.1126/science.280.5366.1046`.

R. Kube, H. Bracht, J. L. Hansen, A. N. Larsen, E. E. Haller, S. Paul, and W. Lerch. Composition dependence of Si and Ge diffusion in relaxed Si1-xGex alloys. *Journal of Applied Physics*, 107(7):73520, Apr 2010. ISSN 0021-8979. doi: 10.1063/1.3380853.

A. Kumar, H. Barda, L. Klinger, M. W. Finnis, V. Lordi, E. Rabkin, and D. J. Srolovitz. Anomalous diffusion along metal/ceramic interfaces. *Nature Communications*, 9(1), 2018. ISSN 20411723. doi: 10.1038/s41467-018-07724-7.

S. L. Lai, G. Ramanath, L. H. Allen, P. Infante, and Z. Ma. High-speed (10^4°C/s) Scanning Microcalorimetry with Monolayer Sensitivity (J/m^2). *Applied Physics Letters*, 67:1229–1231, 1995. ISSN 00036951. doi: 10.1063/1.115016.

A. D. Le Claire. The analysis of grain boundary diffusion measurements. *British Journal of Applied Physics*, 14(6):351, Jun 1963. ISSN 0508-3443. doi: 10.1088/0508-3443/14/6/317.

H. S. Levine and C. J. MacCallum. Grain Boundary and Lattice Diffusion in Polycrystalline Bodies. *Journal of Applied Physics*, 31(3):595–599, Mar 1960. ISSN 0021-8979. doi: 10.1063/1.1735634.

C. Li, Z. Wang, Z. He, Y. Li, J. Mao, K. Dai, C. Yan, and J. Zheng. An advance review of solid-state battery: Challenges, progress and prospects. *Sustainable Materials and Technologies*, 29:e00297, Sep 2021. ISSN 2214-9937. doi: 10.1016/J.SUSMAT.2021.E00297.

A. C. Longden. Electrical Resistance of Thin Films Deposited by Kathode Discharge. *Physical Review (Series I)*, 11(2):84, Aug 1900. ISSN 0031899X. doi: 10.1103/PhysRevSeriesI.11.84.

T. Luka, S. Großer, C. Hagendorf, K. Ramspeck, and M. Turek. Intra-grain versus grain boundary degradation due to illumination and annealing behavior of multi-crystalline solar cells. *Solar Energy Materials and Solar Cells*, 158: 43–49, Dec 2016. ISSN 09270248. doi: 10.1016/J.SOLMAT.2016.05.061.

G. Maltezos, M. Johnston, K. Taganov, C. Srichantaratsamee, J. Gorman, D. Baltimore, W. Chantratita, and A. Scherer. Exploring the limits of ultrafast polymerase chain reaction using liquid for thermal heat exchange: A proof of principle. *Applied Physics Letters*, 97(26):264101, Dec 2010. ISSN 0003-6951. doi: 10.1063/1.3530452. URL `https://aip.scitation.org/doi/abs/10.1063/1.3530452`.

H. Mehrer. *Diffusion in solids: fundamentals, methods, materials, diffusion-controlled processes*. Springer, 2007.

P. Mehrotra. Biosensors and their applications – A review. *Journal of Oral Biology and Craniofacial Research*, 6(2):153–159, May 2016. ISSN 2212-4268. doi: 10.1016/J.JOBCR.2015.12.002.

Y. Mishin and I. M. Razumovskii. Analysis of an asymmetrical model for boundary diffusion. *Acta Metallurgica et Materialia*, 40(3):597–606, Mar 1992. ISSN 0956-7151. doi: 10.1016/0956-7151(92)90409-8.

Y. Mishin, C. Herzig, J. Bernardini, and W. Gust. Grain boundary diffusion: fundamentals to recent developments. *International Materials Reviews*, 42(4): 155–178, Jan 1997. ISSN 0950-6608. doi: 10.1179/imr.1997.42.4.155.

K. Mullis, F. Faloona, S. Scharf, R. Saiki, G. Horn, and H. Erlich. Specific enzymatic amplification of DNA in vitro: The polymerase chain reaction. *Cold Spring Harbor Symposia on Quantitative Biology*, 51(1):263–273, 1986. ISSN 00917451. doi: 10.1101/SQB.1986.051.01.032.

T. Neuhauser, G. Tinti, H. Leiste, N. Casati, M. Stüber, and K. Woll. Analysis of the reaction runaway in Al/Ni multilayers with combined nanocalorimetry and time-resolved X-ray diffraction. *Acta Materialia*, 195:579–587, 2020. ISSN 13596454. doi: 10.1016/j.actamat.2020.05.035.

T. Nolan, R. E. Hands, and S. A. Bustin. Quantification of mRNA using real-time RT-PCR. *Nature Protocols*, 1(3):1559–1582, Aug 2006. ISSN 17542189. doi: 10.1038/NPROT.2006.236.

Y. Pei, L. Zheng, W. Li, S. Lin, Z. Chen, Y. Wang, X. Xu, H. Yu, Y. Chen, and B. Ge. Interstitial Point Defect Scattering Contributing to High Thermoelectric Performance in SnTe. *Advanced Electronic Materials*, 2(6), 2016. ISSN 2199160X. doi: 10.1002/aelm.201600019.

L. Pray. Discovery of DNA Double Helix: Watson and Crick | Learn Science at Scitable, 2008. URL `https://www.nature.com/scitable/topicpage/discovery-of-dna-structure-and-function-watson-397/`.

M. W. Putty, S. C. Chang, R. T. Howe, A. L. Robinson, and K. D. Wise. Process Integration for active polysilicon resonant microstructures. *Sensors and Actuators*, 20(1-2):143–151, Nov 1989. ISSN 0250-6874. doi: 10.1016/0250-6874(89)87112-4.

L. Qiao, Y. He, H. Wang, Z. Shi, Z. Li, G. Xiao, and L. Yang. Effect of grain boundary deformation on the critical temperature degradation of superconducting Nb3Sn under hydrostatic pressure. *Journal of Alloys and Compounds*, 864:158116, May 2021. ISSN 0925-8388. doi: 10.1016/J.JALLCOM.2020.158116.

E. Rabkin. Grain boundary interdiffusion in the case of concentration-dependent grain boundary diffusion coefficient. *Interface Science*, 3(3):219–226, Nov 1996. doi: 10.1007/bf00191049.

Lj. Ristic, M. L. Kniffin, R. Gutteridge, and H. G. Hughes. Properties of polysilicon films annealed by a rapid thermal annealing process. *Thin Solid Films*, 220(1-2):106–110, Nov 1992. ISSN 0040-6090. doi: 10.1016/0040-6090(92)90556-Q.

Soroosh S.-A., V. Yurkiv, A. Gutierrez, M. Cheng, M. Balasubramanian, F. Mashayek, J. Croy, and R. Shahbazian-Yassar. Revealing Grain-Boundary-Induced Degradation Mechanisms in Li-Rich Cathode Materials. *Nano Letters*, 20(2):1208–1217, Feb 2020. ISSN 15306992. doi: 10.1021/ACS.NANOLETT.9B04620/ASSET/IMAGES/LARGE/NL9B04620_0006.JPEG. URL `https://pubs.acs.org/doi/full/10.1021/acs.nanolett.9b04620`.

M. Short and K. Woll. An expansion of the Fisher model for concentration dependent grain boundary diffusion. *Acta Materialia*, 217:117056, Sep 2021. ISSN 1359-6454. doi: 10.1016/J.ACTAMAT.2021.117056.

M. Short, F. Bridges, T. Keiber, G. Rogl, and P. Rogl. A comparison of the local structure in ball-milled and hand ground skutterudite samples using EXAFS. *Intermetallics*, 63:80–85, 2015. ISSN 09669795. doi: 10.1016/j.intermet.2015.04.001.

M. Short, J. Müller, S. Lee, H. Fornasier, U. Köhler, V. Ott, M. Stüber, B. Gerdes, T. Rupp, C. Kirchlechner, and K. Woll. Heterogeneous microstructures tuned in a high throughput architecture. *Materials and Design*, 229, May 2023. ISSN 18734197. doi: 10.1016/J.MATDES.2023.111834.

G. J. Snyder and E. S. Toberer. Complex thermoelectric materials. *Nature Materials 2008 7:2*, 7(2):105–114, Feb 2008. ISSN 1476-4660. doi: 10.1038/nmat2090.

J. Sommer and C. Herzig. Direct determination of grain-boundary and dislocation self-diffusion coefficients in silver from experiments in type-C kinetics. *Journal of Applied Physics*, 72(7):2758–2766, Oct 1992. ISSN 00218979. doi: 10.1063/1.352328.

J. H. Son, B. Cho, S. Hong, S. H. Lee, O. Hoxha, A. J. Haack, and L. P. Lee. Ultrafast photonic PCR. *Light: Science and Applications*, 4(7):e280, Jul 2015. ISSN 20477538. doi: 10.1038/lsa.2015.53.

J. C. Steinberg. Hall Effect and Specific Resistance of Evaporated Films of Silver, Copper and Iron. *Physical Review*, 21(1):22, Jan 1923. ISSN 0031899X. doi: 10.1103/PhysRev.21.22.

I. Stone. On the Electrical Resistance of Thin films. *The Physical Review*, 6(1): 1–16, Jan 1898.

J. Sung Yun, J. Kim, T. Young, R. J. Patterson, D. Kim, J. Seidel, S. Lim, M. A. Green, S. Huang, A. Ho-Baillie, J. S. Yun, J. Kim, T. Young, R. J. Patterson, M. A. Green, S. Huang, A. Ho-Baillie, D. Kim, J. Seidel, and S. Lim. Humidity-Induced Degradation via Grain Boundaries of $HC(NH_2)_2PbI_3$ Planar Perovskite Solar Cells. *Advanced Functional Materials*, 28:1705363, 2018. doi: 10.1002/adfm.201705363.

T. Surholt, Y. M. Mishin, and C. Herzig. Grain-boundary diffusion and segregation of gold in copper: Investigation in the type-B and type-C kinetic regimes. *Physical Review B*, 50(6):3577–3587, Aug 1994. doi: 10.1103/PhysRevB.50.3577.

T. Suzuoka. Lattice and Grain Boundary Diffusion in Polycrystals. *Transactions of the Japan Institute of Metals*, 2(1):25–32, 1961. doi: 10.2320/matertrans1960.2.25.

I. A. Szabó, D. L. Beke, and F. J. Kedves. On the transition between the C and B kinetic regimes for grain-boundary diffusion. *Philosophical Magazine A*, 62 (2):227–239, Aug 1990. ISSN 0141-8610. doi: 10.1080/01418619008243919.

J. Tang, X. He, Y. Lei, H. Shi, Q. Guo, J. Liu, D. He, L. Yan, and K. Wang. Temperature-responsive split aptamers coupled with polymerase chain reaction for label-free and sensitive detection of cancer cells. *Chemical communications (Cambridge, England)*, 53(87):11889–11892, 2017. ISSN 1364-548X. doi: 10.1039/C7CC06218D.

M. Vaidya, S. Trubel, B. S. Murty, G. Wilde, and S. V. Divinski. Ni tracer diffusion in CoCrFeNi and CoCrFeMnNi high entropy alloys. *Journal of Alloys and Compounds*, 688:994–1001, 2016. ISSN 0925-8388. doi: https://doi.org/10.1016/j.jallcom.2016.07.239.

M. Vaidya, K. G. Pradeep, B. S. Murty, G. Wilde, and S. V. Divinski. Bulk tracer diffusion in CoCrFeNi and CoCrFeMnNi high entropy alloys. *Acta Materialia*, 146:211–224, 2018. ISSN 1359-6454. doi: https://doi.org/10.1016/j.actamat.2017.12.052.

A. Vignes and C. E. Birchenall. Concentration dependence of the interdiffusion coefficient in binary metallic solid solution. *Acta Metallurgica*, 16(9):1117–1125, 1968. ISSN 0001-6160. doi: https://doi.org/10.1016/0001-6160(68)90047-3.

G. R. Wait. Hall Effect and Specific Resistance of Silver Films. *Physical Review*, 19(6):615, Jun 1922. ISSN 0031899X. doi: 10.1103/PhysRev.19.615.

Y. Wang and J. He. Fabrication of ultra-smooth hybrid thin coatings towards robust, highly transparent, liquid-repellent and antismudge coatings. *Journal of Colloid and Interface Science*, 594:781–790, Jul 2021. ISSN 0021-9797. doi: 10.1016/J.JCIS.2021.03.077.

P. Waters and A. A. Volinsky. Stress and moisture effects on thin film buckling delamination. *Experimental Mechanics*, 47(1):163–170, Feb 2007. ISSN 00144851. doi: 10.1007/S11340-006-9346-4.

R. T. P. Whipple. Concentration contours in grain boundary diffusion. *The London, Edinburgh, and Dublin Philosophical Magazine and Journal of Science*, 45(371):1225–1236, 1954. doi: 10.1080/14786441208561131. URL `https://doi.org/10.1080/14786441208561131`.

P. Wu, Y. Zeng, and H. M. Jin. *Interpretation and prediction of diffusion activation energy from thermodynamic model*. Springer Verlag, 2014. doi: 10.1007/978-981-287-128-2_9/FIGURES/5.

Y. Yamaguchi, D. A. Kiewit, and T. Aoki. Electrical Resistivity of NiAl, CoAl, NiGa, and CoGa. *Journal of Applied Physics*, 39:231–232, 1968. doi: 10.1063/1.1655738.

D. Yavas, P. Mishra, A. Alshehri, P. Shrotriya, K. R. Hebert, and A. F. Bastawros. Nanoindentation study of corrosion-induced grain boundary degradation in a pipeline steel. *Electrochemistry Communications*, 88:88–92, Mar 2018. ISSN 1388-2481. doi: 10.1016/J.ELECOM.2018.02.001.

D. Yavas, T. Phan, L. Xiong, K. R. Hebert, and A. F. Bastawros. Mechanical degradation due to vacancies produced by grain boundary corrosion of steel. *Acta Materialia*, 200:471–480, Nov 2020. ISSN 1359-6454. doi: 10.1016/J.ACTAMAT.2020.08.080.

F. Yi and D. A. Lavan. Nanocalorimetry: Exploring materials faster and smaller. *Applied Physics Reviews*, 6(3), Sep 2019. ISSN 19319401. doi: 10.1063/1.5098297.

F. Yi, J. B. Delisio, M. R. Zachariah, and D. A. Lavan. Nanocalorimetry-Coupled Time-of-Flight Mass Spectrometry: Identifying Evolved Species during High-Rate Thermal Measurements. *Analytical Chemistry*, 87:35, 2015. doi: 10.1021/acs.analchem.5b01872.

M. You, Z. Li, S. Feng, B. Gao, C. Yao, J. Hu, and F. Xu. Ultrafast Photonic PCR Based on Photothermal Nanomaterials. *Trends in Biotechnology*, 38(6): 637–649, Jun 2020. ISSN 0167-7799. doi: 10.1016/J.TIBTECH.2019.12.006.

M. Zambon, C. Drosten, M. Koopmans, D. Alland, Ka. Vandemaele, M. Samaan, C. Fuster, W. Zhang, C. Barnadas, L. Stevens, C. Oxenford, S. Cognat, K. Kojima, C. Dolea, M. Van Kerkhove, M. D. Perkins, and K. von Eije. Laboratory testing of human suspected cases of novel coronavirus (nCoV) infection. Technical report, World Health Organization, Jan 2020. URL `https://www.who.int/publications/i/item/10665-330374`.

H. Zhang, D. Lee, Y. Shen, Y. Miao, J. Bae, Y. Liu, J. Schroers, Y. Xiang, and J. J. Vlassak. Combinatorial temperature resistance sensors for the analysis of phase transformations demonstrated for metallic glasses. *Acta Materialia*, 156: 486–495, Sep 2018. ISSN 1359-6454.

R. Zhang, C. Wang, M. Ge, and H. L. Xin. Accelerated Degradation in a Quasi-Single-Crystalline Layered Oxide Cathode for Lithium-Ion Batteries Caused by Residual Grain Boundaries. *Nano Letters*, 2022a. ISSN 15306992. doi: 10.1021/ACS.NANOLETT.2C01103/ASSET/IMAGES/LARGE/NL2C01103_0004.JPEG.

W. Zhang, N. Sobahi, R. E. Fernandez, J. Dai, D. Yeom, J. Kim, S. Kim, S. Ahn, J. Choi, Y. Kim, and C. Koo. A Thermocycler Using a Chip Resistor Heater and a Glass Microchip for a Portable and Rapid Microchip-Based PCR Device. *Micromachines 2022, Vol. 13, Page 339*, 13(2):339, Feb 2022b. ISSN 2072-666X. doi: 10.3390/MI13020339. URL `https://www.mdpi.com/2072-666X/13/2/339/htmhttps://www.mdpi.com/2072-666X/13/2/339`.